TU

TECHNISCHE UNIVERSITÄT WIEN

DISSERTATION

Improved Ultrasonic Distance Measurement in Air

ausgeführt zum Zwecke der Erlangung des akademischen Grades eines Doktors
der technischen Wissenschaften unter der Leitung von

Prof. Dr. Herbert Schweinzer

Prof. Dr. Gottfried Magerl

Institut für elektrische Mess- und Schaltungstechnik E354

eingereicht an der Technischen Universität Wien

Fakultät für Elektrotechnik und Informationstechnik

von

DI Hannes Elmer

9525842

Propst Führerstrasse 32/4/1, 3100 St.Pölten

Wien, im September 2005

Danksagung

Ich möchte mich an dieser Stelle bei allen bedanken, die mich bei dieser Arbeit unterstützten.

In allererster Linie zählt dazu Prof. Dr. Herbert Schweinzer, der mich schon im Rahmen meiner Diplomarbeit in das Gebiet der Ultraschall-Entfernungsmessung einführte. Er stand mir unermüdlich mit Rat und Tat zur Seite und ich möchte ihm für seine wertvolle Zusammenarbeit nicht nur für diese Arbeit sondern auch für zahlreiche Konferenzbeiträge und die alltägliche Arbeit am Institut meinen herzlichen Dank aussprechen.

Im Weiteren danke ich Prof. Dr. Gottfried Magerl für seine Tür, die mir für Gespräche jeder Art immer offen stand, von denen ich viel profitieren konnte. Ganz besonders möchte ich ihm auch für die äußerst gründliche Durchsicht dieser Arbeit danken.

Vielen Dank möchte ich Prof. Dr. Georg Brasseur aussprechen, der trotz seines vollen Terminkalenders die Zeit für eine sehr ausführliche Zweitbegutachtung meiner Arbeit aufbrachte und mir die Möglichkeit bot, sie an seinem Institut an der TU Graz vorzustellen.

Bedanken möchte ich mich auch bei allen meinen Kollegen und Kolleginnen am Institut für elektrische Mess- und Schaltungstechnik mit denen ich im Laufe meiner Zeit als Universitätsassistent zusammenarbeiten durfte und die diese vier Jahre zu einem sehr interessanten und schönen Lebensabschnitt werden ließen.

Mein Dank gilt an dieser Stelle auch meinen Eltern, die mir die für diese Arbeit notwendige Ausbildung zukommen ließen und mir so eine unbeschwerte Studienzeit ermöglichten.

Vielen Dank sage ich auch meiner lieben Frau Barbara, die mir mit vielen Gesprächen und aufmunternden Worten durch die Entstehungsphasen dieser Arbeit half.

Ich möchte all diesen und auch allen Unerwähnten ein herzliches Dankeschön aussprechen, die mir auf die eine oder andere Weise halfen und so zum Gelingen der Arbeit beitrugen.

Kurzfassung

Das Verfahren der Ultraschall-Entfernungsmessung ist seit vielen Jahren bekannt. In den meisten Fällen wird das Laufzeitverfahren (Time of Flight – ToF) angewendet, welches die Zeit auswertet, die ein Ultraschallsignal für das Durchlaufen einer zu messenden Strecke benötigt.

In der Literatur finden sich verschiedene Topologien von Ultraschall-Entfernungsmesssystemen, die sich vor allem in Bezug auf die Positionen der Sender und Empfänger zueinander unterscheiden. In den meisten Fällen befinden sich Sender und Empfänger nahe beieinander oder sind sogar kombiniert (in sogenannten Tranceivern). Die Messung erfordert dann eine passive Reflexion an dem Objekt, zu dem die Entfernung gemessen werden soll. Eine andere Möglichkeit ist die Messung der Entfernung, die zwischen Sender und Empfänger liegt (A-B-Messung). Beide Methoden bieten interessante Eigenschaften, die sich im Verfahren der "Aktiven Reflexion" kombinieren lassen.

Eine genaue Erfassung der Laufzeit ist aufgrund der relativ geringen Schallgeschwindigkeit in Luft mit moderner Elektronik problemlos möglich. Im Fall von hochgenauer Entfernungsmessung spielt vielmehr die Schallgeschwindigkeit selbst die entscheidende Rolle, da sie von verschiedenen Parametern, wie der Temperatur, der relativen Luftfeuchtigkeit, der CO_2 – Konzentration und dem Luftdruck abhängt. Ebenso müssen Luftbewegungen, die die Relativgeschwindigkeiten der Schallsignale in Bezug zur Umgebung beeinflussen, berücksichtigt werden.

Im Fall von passiver Reflexion an Objekten hängen die erreichbaren Resultate stark von den Reflexionseigenschaften der Objekte ab. Den größten Einfluss spielt dabei die Form des Objektes, welche entweder zu spiegelnder Reflexion (liefert große Amplituden in eine bestimmte Richtung) oder zu diffuser Reflexion (kleine Amplitude in viele Richtungen) führt.

Konventionelle Ultraschallentfernungsmesssysteme verwenden meist monofrequente Burstsignale, die mit Hilfe piezoelektrischer Wandler erzeugt werden können. Die Signalerkennung erfolgt durch Amplitudendetektion, welche mit Hilfe von zeitgesteuerten Verstärkern beziehungsweise adaptiven Schwellwerten eine Kompensation der Luftdämpfung und Signalstreuung erlaubt. Trotz dieser Verbesserung ist dieses Verfahren auf genau definierte Objekte beschränkt, deren Positionen im Bereich der Sensorachse liegen müssen. Eine Unterscheidung zwischen schwach reflektierenden Objekten im Bereich der Sensorachse und gut reflektierenden weit außerhalb der Hauptkeule ist bei diesem Verfahren nicht möglich, wodurch es zu stark objektabhängigen Detektionsbereichen kommt.

Das wesentlich Neue der hier beschriebenen Methode ist der gut definierbare Detektionsbereich, der überdies noch unabhängig von den Reflexionseigenschaften der Objekte

ist. Es gibt mehrere Arbeiten die mit Hilfe der Trilateration (basiert auf Auswertung der Laufzeitunterschiede eines Signals von meist einem Sender zu mehreren Empfängern) den Winkel eines eintreffenden Signals bestimmen und so auf die Position des reflektierenden Objektes schließen. Besonders im Fall mehrerer reflektierender Objekte kommt es bei diesem Verfahren zu Mehrdeutigkeiten, die manchmal nur schwer beherrschbar sind. Das hier gezeigte Messverfahren schließt somit eine Lücke zwischen Systemen mit großteils undefiniertem Messbereich (insbesondere im Fall verschiedener Objekte) und aufwendigen Systemen die den genauen Winkel zu Objekten bestimmen können: mit nur einem Sender und Empfänger wird ein gut definierter und objektunabhängiger Detektionsbereich erreicht. Das Verfahren basiert auf der Auswertung der frequenzabhängigen Abstrahlcharakteristik des Ultraschallsenders, welcher, im Fall von breitbandigen Signalen, zu unterschiedlich - in Abhängigkeit der Abstrahlrichtung - kodierten Signalen führt. Die empfangenen Signale werden mit Hilfe des Ein-Bit-Korrelationsverfahrens analysiert, welches amplitudenunabhängige Ergebnisse liefert. Das Korrelationsverfahren liefert außerdem hochgenaue Signalerkennung, Störsicherheit und erlaubt Signalkodierung. Ein leicht modifiziertes Verfahren ermöglicht die Winkelbestimmung im Bereich der Detektionsgrenzen.

Dieses neue Messverfahren eignet sich für Anwendungen, die einen definierten Detektionsbereich - auch bei verschiedenen Objekten - verlangen. Dies sind, zum Beispiel Kollisionsvermeidungssysteme bei mobilen Robotersystemen oder Industrierobotern. Ebenso verlangen Überwachungsaufgaben einen genau definierten und objektunabhängigen Detektionsbereich. Im Fall von scannenden Verfahren, wie sie zum Beispiel für die Umgebungserkennung mobiler Roboter verwendet werden, ist die Winkelbestimmung am Rand des Detektionsbereiches von besonderer Bedeutung, da sie die Geschwindigkeit von hochauflösenden Scandurchläufen deutlich erhöht.

Abstract

Distance measurement by means of acoustic ultrasonic waves has been well known for many years. In most cases, ultrasonic distance measurement systems are based on the Time of Flight (ToF) principle, which evaluates the time while an ultrasonic signal needs to run through the distance to be measured.

There are several possible topologies found in literature, especially regarding the positions of transmitter and receiver: while in many cases they are located near together or are even combined (in a so called transceiver) and evaluate the signals occurring due to passive reflection at the object to which the distance is measured, others try to measure the distance between transmitter and receiver (A-B-measurement). Both methods provide different interesting aspects that can be combined in special cases (e.g. in "Active Reflection").

Due to the relatively low speed of sound in air, accurate ToF-measurement can be easily accomplished by means of state of the art electronics. However, in case of high accuracy distance measurements, the actual value of the speed of sound in air plays a critical role and must be taken into account: it depends on various parameters, especially on the temperature, the relative humidity, the CO_2-concentration and the ambient pressure. The air movement is of interest too, as it has a strong impact on the speed of sound relative to ground.

In cases where passive reflections on objects are necessary, the reflection properties significantly influence the achievable results. The main characteristic provides the shape of the object which defines whether specular reflection (high amplitudes but distinctive direction) or diffuse reflection (low amplitudes in many directions) takes place.

Conventional ultrasonic distance measurement systems mainly use monofrequent burst signals that can be easily generated by, for example, piezo-electric transmitters. Signal receiving is accomplished by amplitude detection. Although time varying amplification or threshold adaptation basically allows compensation of air damping and spreading effects, it only works well in case of previously defined objects that are located near the sensor axis. Basically, these systems cannot distinguish between objects providing low reflections located near the sensor axis and objects with strong reflections lying far outside the main lobe. Therefore, the range of detection strongly depends on the reflecting objects, too.

The particularly new of the ultrasonic distance measurement method presented in this thesis is the well definable range of detection that is, moreover, independent of the reflection properties of the objects. There are several works found doing trilateration using mostly one transmitter and several receivers, which evaluate the different ToFs occurring at each receiver. These systems can determine the receiving angle of ultrasonic waves and, therefore, give an estimation

of the object's position. However, especially in case of multiple reflecting objects, there often occur ambiguities that can be hardly solved in some cases. The presented measurement principle provides the missing link between systems with mostly undefined measurement range (in case of arbitrary objects) and rather complicated systems that deliver the angle towards an object: using only one transmitter and one receiver, it provides a well defined and object independent range of detection.

The main principle is the evaluation of the frequency dependent radiation pattern of ultrasonic transmitters which leads, in case of wide band signals, to differently coded signals depending on the angle of transmission. After receiving of a reflected signal, it is evaluated by means of the One Bit Correlation method that provides results that are independent of the signal amplitudes. This correlation based method provides high accuracy signal detection, robustness, and coding possibilities. An adaptation of the algorithm also allows determination of the angle towards the object within the range of the borders.

This new measurement method is well suited for applications that must deal with arbitrary objects, but require a well defined range of detection, too. This occurs, for example, in case of collision detection applications in connection with mobile or industrial roboters. Also many control applications require a well defined and object independent detection area. In case of scan based algorithms, e.g. for scene recognition, the angle determination in the range of the detection borders is of main interest, as it significantly improves the speed of high accuracy scanning tasks.

Table of contents

Index of Figures

Index of tables

List of abbreviations

CTFM	continuous transmission frequency modulation
DSO	digital sampling oszilloscope
FFT	fast Fourier transform
FPGA	field programmable gate array
LoS	line of sight
PoR	point of reflection
PVDF	Polyvinylideneflouride
RF	radio frequency
T/R	transmitter and receiver
ToF	time of flight
SNR	signal to noise ratio

1 Introduction

The use of ultrasonic signals in air is a well known principle for distance measurement, presence detection, and scene recognition which is popular due to its low costs and robustness. In contrast to optical sensors, requiring a rather clean and well defined illuminated environment, ultrasonic sensors are mainly insensitive to dust, atomized spray, and other contamination. The basic principle of the Time of Flight (ToF) evaluation of reflected bursts is used in most commercially available sensors and in the majority of cases only the distance towards the nearest object inside the range of detection is delivered. A lot of research has been done for many years up to now to get more information about the environment using more sophisticated sensor principles.

An advantage of ultrasonic sensors compared with optical solutions is the inherent reduction to only significant information. This information describes mainly the geometric shape of the environment – in agreement with the information necessary for mobile robots to navigate in unknown environments, to perform map building or to retrieve their own positions using previously recorded data. However, there are lots of problems ultrasonic sensors have to deal with, for example the limited echo separation capability that prevents discrimination of objects in similar distances or the echo-allocation in triangulation based systems.

The aim of this work is a concept of a new measurement system that provides well defined measurement conditions. The new concept is based on the evaluation of properties of ultrasonic waves in air and takes account of the transducer characteristics by using a special method of matched filtering. Finally, a prototype is designed to verify the expected results.

The work is organized in the following sections:

- At first basic measurement topologies usable in ultrasonic systems are compared according to their properties.

- Ultrasonic waves are bound to a transmission medium whose properties strongly influence the propagation characteristics. Therefore, in chapter 3 the influences of the properties of air to ultrasonic signals are discussed.

- For many years a lot of work has been done in the range of ultrasonic measurement. In chapter 4 a short overview over the state of the art is given and untreated problems are discussed.

- Based on the results of the previous chapters, in chapter 5 a concept of a new measurement system providing well defined measurement properties is developed.

- According to the new measurement concept, correlation based signal detection is used to detect ultrasonic signals. The basic correlation method is modified to the one bit correlation method that helps to overcome several problems.

- The conversion of electrical signals to ultrasonic waves and vice versa is accomplished by ultrasonic transducers. In chapter 7 the model of a piston membrane is evaluated that describes the majority of ultrasonic sensors.

- In chapter 8 the final measurement system is presented and its main feature, the well defined and adjustable detection area, is discussed.

- Finally, a prototype of the measurement system is introduced and its components are described. Furthermore, some measurement tasks are provided.

- At the end, a short summary and an outlook over future projects necessary to get a ready to use measurement system are given.

2 Basic Measurement topologies

Ultrasonic distance measurement systems are mainly based on the evaluation of the ToF of ultrasonic waves. Ultrasonic waves are generated by an ultrasonic transmitter and received by an ultrasonic receiver. While most transmitters can operate as receiver as well (so called transceivers), some topologies require separate devices for operation. In the following, some basic topologies of ultrasonic measurement systems are discussed which primarily differ in the position of the transmitter and receiver within the measuring assembly.

2.1 A-B-Measurement

The A-B-measurement topology uses one ultrasonic transmitter (T) and one receiver (R) which are placed on each side of the measurement distance (compare Figure 2.1). The distance is calculated by evaluating the time ToF of the ultrasonic signal running once through the measurement distance.

The main advantages of this topology are:

- Well defined detection range by position of transmitter and receiver

- Indifferent to obstacles in the measurement range as long as the line of sight stays free

- Non ambiguous measurement result – first received signal represents shortest way (line of sight)

- Not depending on reflection properties of objects

- Basic attenuation due to spreading of the ultrasonic lobe proportional to $1/d_{air}^2$ (with distance d_{air})
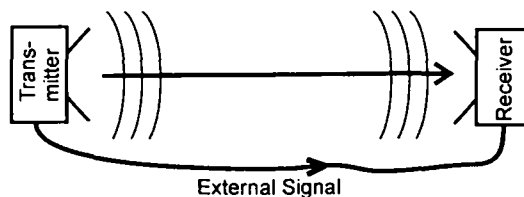
Figure 2.1: Possible configuration of an A-B-measurement system

However, there are also disadvantages to mention:

- A-B-measurement requires an external signal (e.g. electrical, optical, RF,...) to transmit the start- respectively the endpoint of the measurement cycle

- Sensitive to wind because ultrasonic signal runs only once through the measured distance (compare chapter 3.1.7)

- Measurement towards arbitrary objects is not possible (must be equipped with a transmitter and receiver, respectively)

2.2 Passive Reflection

Most ultrasonic distance measurement systems are based on passive reflection. In this topology the transmitter is located close to the receiver and in most cases a transceiver is used. The measurement cycle is initiated by emitting an ultrasonic signal and starting an electronic clock at the same time. The ultrasonic signal is reflected by each object inside the measurement range of the sensor. The arrival time of each can be recorded and allows calculation of the distance to each reflecting object.
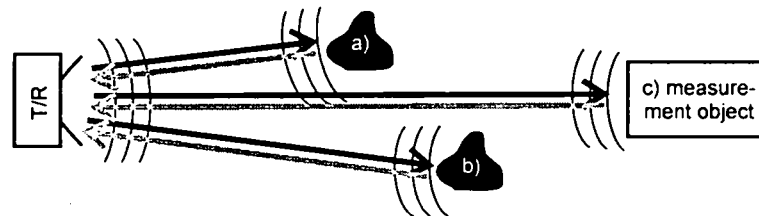
Figure 2.2: Principle of passive reflection with obstacles (*a* and *b*) inside the detection area

Passive reflection systems provide the following advantages:

- measurement towards arbitrary objects is possible

- insensitive to wind (compensation because signal runs once in each direction)

- easy implementation (only one device must be installed)

- no external signal necessary

The following disadvantages are observed:

- multiple results due to multiple objects – assignment of echoes to objects is critical

- good echo-separation capability necessary (if objects are only laterally shifted with regard to the measurement direction providing nearly the same measurement distance)

- dependent on reflection properties of objects

- basic attenuation due to spreading of the ultrasonic lobe and reflection process at least proportional to $1/d_{air}^{4}$

Most commercial ultrasonic distance measurement systems evaluate the first incoming signal only and, therefore, they can measure the distance to the nearest object (e.g. object *a* in Figure 2.2).

2.3 Active Reflection

The active reflection [Elm00] is a new method for ultrasonic distance measurement. It differs from the passive method by the presence of an additional ultrasonic device at the target (device *B* in Figure 2.3). Each device is equipped with a transmitter and receiver, a transceiver is possible, too.
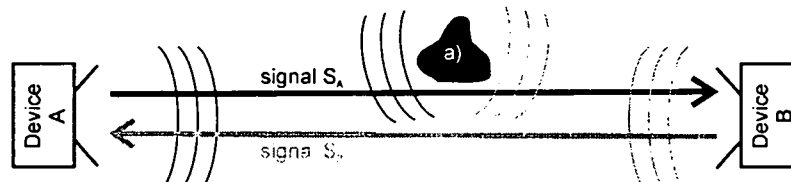
Figure 2.3: Principle of Active Reflection with coded signals S_A and S_B

Basically, active reflection combines two A-B-measurement systems which results in the advantages of methods using reflection without getting multiple results. It works as follows: Device A initiates a measurement cycle by starting an internal timer and transmitting signal S_A at the same time. When device B receives this signal the first time, it responds by transmitting a signal S_B after a well-defined delay time (necessary for switching from receiving to transmitting mode). Device A detects this signal and stops its timer, which now contains twice the propagation time plus an additional offset due to the length of the transmitted signals S_A and S_B and the well defined delay time of device B. While the reflection on obstacles will result in erroneous results in passive reflection, active reflection makes use of the possibility of coding signals. While device A generates signal S_A, its receiver is sensitive to signals S_B. Device B is configured vice versa. As a result, the receiver of device A only detects signal S_B, whereas echoes generated by obstacles are not detected (object *a* in Figure 2.3). As device B does not know at which time signal S_A arrives, it has to evaluate the incoming signal all over the time, which can be achieved only by using a real time evaluation method.

The active reflection combines the topology of the A-B-measurement with the advantages of passive reflection (indifference to wind, no external signal). Its main application is the measurement of far distances between two well defined points.

The advantages of active reflection are:

- well defined detection range by position of transmitter and receiver

- indifferent to obstacles in the measurement range as long as the line of sight is kept free

- non ambiguous measurement result – first received signal represents shortest way (line of sight)

- not dependent on reflection properties of objects

- basic attenuation due to spreading of the ultrasonic lobe proportional to $1/d_{air}^2$

- indifference to wind (compensation because signal runs once in each direction)

- no external signal necessary

The disadvantages are the following:

- measurement towards arbitrary objects is not possible (must be equipped with a transmitter and receiver, respectively)

- differently coded signals are necessary for device A and B

- real time evaluation of the received signals is necessary

2.4 Comparison of topologies

In Table 2.1 a short overview of the properties provided by different topologies is presented. While some properties (e.g. high resolution and noise immunity) concern all presented topologies, there are also significant differences found.

Aspect	A-B - Measurement	Active reflection	Passive reflection
high resolution	impulse compression		
noise immunity	correlation based receiver; increased by extending the correlation time		
good echo separation	n / a		impulse compression
distinguish signal S_B from echoes of S_A	n / a	different coding of signals S_A and S_B	n / a
multiple systems in parallel	different coding of signals		
high measurement rate	different coding of signals of following measurement cycles; pipelining possible with separate transmitter and receiver		
basic attenuation (signal spreading)	prop. $1/d_{air}^2$; due to the use of 2 transducers		prop. $1/d_{air}^4$; due to passive reflection
real time evaluation	optional for high measurement rate	necessary for system	optional for high measurement rate
obstacles in measurement area	one result		multiple results
wind sensitivity	sensitive	not sensitive	
external signal	necessary	ultrasonic signal only	

Table 2.1: Summary of properties of A-B-, Active- and Passive reflection systems

3 Influences to ultrasonic measurement systems

In the following a short summary of the main properties of ultrasonic distance measurement systems is given: at first the physical properties of air and their influence to the speed of sound and the basic reflection properties are discussed. Secondly, elementary measurement features of ultrasonic distance measurement systems are evaluated. Next the necessity of a well defined detection area that is independent of the objects reflecting properties is shown. At last some qualities of signal processing methods are addressed that are necessary in some applications.
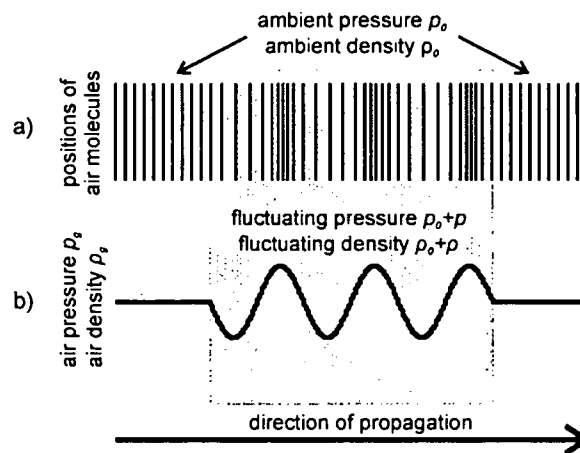
Figure 3.1: Schematic of longitudinal wave propagation in air
with a) position of air molecules and b) diagram of air pressure p_g and density ρ_g

3.1 Physical Properties of the air channel

3.1.1 Derivation of the speed of sound

Acoustic waves are always bound to a transmission medium which is the ambient air in our case. As shown in Figure 3.1 acoustic waves are fast fluctuations of the ambient pressure p_0 of the acoustic pressure p which leads to the total pressure p_g (Figure 3.1/b). Due to the compressibility of air, a changing pressure also causes a change of the density ρ. These fluctuations proceed in form of longitudinal waves consisting of compressions and expansions of the air (compare schematic in Figure 3.1/a which shows the positions of the air molecules). The speed of the molecules themselves is called the sound particle velocity $\bar{v}$ and the speed of

the whole propagating wave is the acoustic velocity c, responsible for transmitting ultrasonic signals.

In the following, a derivation of the speed of sound is given which is based on the thermodynamics of an ideal gas. Then the influences of air properties such as temperature, ambient pressure, relative humidity, and CO_2-content are discussed and an approximation of their influence is given. Afterwards, a nonlinear effect of the acoustic velocity is shown that occurs in case of very high amplitudes of transmitted signals.

3.1.1.1 Basic considerations

The following derivation of the speed of sound is mainly based on [Kut88]. As mentioned before, an acoustic wave is a propagating fluctuation of the sound field values pressure p_g and density ρ_g. These are linked together with a state equation, whose general form is given to

$$p_g = p_g(\rho_g, T) \xrightarrow[\text{change of state}]{\text{adiabatic / isentropic}} p_g = p_g(\rho_g).$$ (3.1)

Due to the high frequency of ultrasonic waves, the heat exchange between adjacent volume elements can be discarded (adiabatic / isentropic change of state), which allows omitting the temperature T in equation (3.1). The ambient air provides static parts of pressure p_0 and density ρ_0, while the longitudinal wave is a temporary deviation p respectively ρ of these static values according to

$$\begin{aligned} p &= p_g - p_0 \\ \rho &= \rho_g - \rho_0 \end{aligned}.$$ (3.2)

Using a Taylor series similar to equation (3.3), equation (3.1) can be expressed in the general form as shown equation (3.4).

$$f(x) \approx \sum_{k=0}^{n} \frac{f^{(k)}(a)}{k!}(x-a)^k$$ (3.3)

$$p_g(\rho_g) \approx \underbrace{p(\rho_0)}_{p_0} + \left(\frac{dp}{d\rho}\right)_{\rho_0} \underbrace{(\rho_g - \rho_0)}_{\rho} + \frac{1}{2}\left(\frac{d^2p}{d\rho^2}\right)_{\rho_0} \underbrace{(\rho_g - \rho_0)^2}_{\rho^2} + \dots$$ (3.4)

According to (3.2) the proceeding wave is based on the fluctuations p and ρ and, therefore, based on equation (3.4) a relation between the fluctuating parts p and ρ is found in (3.5).

$$\begin{aligned} p(\rho) = p_g - p_0 &\approx \underbrace{p(\rho_0)}_{p_0} + \left(\frac{dp}{d\rho}\right)_{\rho_0} \rho + \frac{1}{2}\left(\frac{d^2p}{d\rho^2}\right)_{\rho_0} \rho^2 + \dots - p_0 = \\ &= \left(\frac{dp}{d\rho}\right)_{\rho_0} \rho + \frac{1}{2}\left(\frac{d^2p}{d\rho^2}\right)_{\rho_0} \rho^2 + \dots \end{aligned}$$ (3.5)

In general the temporary changes p and ρ are small compared to the static values p_0 and ρ_0 and, therefore, high-order terms can be discarded to get the linear equation (3.6) between the pressure p and the density ρ.

$$p \approx \left(\frac{dp}{d\rho} \right)_{\rho_0} \rho = c^2 \rho \quad \text{with} \quad c^2 = \left(\frac{dp}{d\rho} \right)_{\rho_0} \tag{3.6}$$

Here the parameter c^2 is introduced as arbitrary factor firstly, but later on it is found to be the speed of sound (compare equation (3.10)).

The connection between the pressure p and the density ρ is given by the laws of conservation of mass and momentum:

$$\underbrace{- \operatorname{grad} p}_{\text{force}} = \underbrace{\rho_g}_{\text{mass}} \underbrace{\frac{d}{dt} \vec{v}}_{\text{acceleration}}$$

$$\underbrace{\operatorname{div} \left(\rho_g \vec{v} \right)}_{\substack{\text{escaping mass} \\ \text{from dV}}} = \underbrace{- \frac{\partial}{\partial t} \rho}_{\substack{\text{density change} \\ \text{in dV}}} \tag{3.7}$$

The vector $\vec{v}$ is the previously mentioned sound particle velocity and the acceleration term in (3.7) is the total acceleration of an air molecule. The connection between the local acceleration and the total acceleration is

$$\underbrace{\frac{d\vec{v}}{dt}}_{\substack{\text{total} \\ \text{acceleration}}} = \underbrace{\frac{\partial \vec{v}}{\partial t}}_{\substack{\text{local} \\ \text{acceleration}}} + \underbrace{\left(\vec{v} \cdot \operatorname{grad} \right) \vec{v}}_{\ll \frac{\partial \vec{v}}{\partial t}} \approx \frac{\partial \vec{v}}{\partial t} . \tag{3.8}$$

In case of sufficiently low sound particle velocities, which can be considered here, the latter term in (3.8) is sufficiently small to be discarded. Also the difference between the resulting pressure p_g and resulting density ρ_g from the static values p_0 respectively ρ_0 are negligible. These approximations together with the definition of c^2 allow deriving the sound field equations from (3.7) to

$$\operatorname{grad} p + \rho_0 \frac{\partial \vec{v}}{\partial t} = 0$$

$$\rho_0 c^2 \operatorname{div} \vec{v} + \frac{\partial p}{\partial t} = 0 \tag{3.9}$$

Elimination of the sound particle velocity $\vec{v}$ finally leads to the partial equation (3.10) which is the wave equation valid for all components of sound field values. It allows describing all acoustical events except losses occurring in reality. In this equation the parameter c^2 is found to be the speed of the propagating wave.

$$\Delta p = \operatorname{div} \operatorname{grad} p = \frac{1}{c^2} \frac{\partial^2 p}{\partial t^2} \tag{3.10}$$

3.1.1.2 Calculation of the speed of sound in an ideal gas

In the following the speed of sound valid for an ideal gas and its dependence on temperature and pressure is shown (based on [Sku54]). The adiabatic state equation (3.11) gives a relation

between the pressures p_x and the volumes V_x at a constant temperature T also using the specific heat ratio of the medium κ.

$$p_1 V_1^\kappa = p_2 V_2^\kappa \tag{3.11}$$

Introducing static values of pressure p_0 and volume V_0 and fluctuating values p and V, the fluctuating pressure p is calculated to

$$p = p_0 \frac{V_0^\kappa}{V^\kappa} = p_0 \left(\frac{\rho}{\rho_0} \right)^\kappa . \tag{3.12}$$

In the latter part the volume V_x is replaced using the equation for the mass $M_x = \rho_x \cdot V_x$ to get a function of p only depending on the density ρ and the static values p_0 and ρ_0. The previously defined speed of sound (3.6) is calculated to

$$c^2 = \left(\frac{dp}{d\rho} \right)_{\rho_0} = \kappa \frac{p_0}{\rho_0} \left(\frac{\rho}{\rho_0} \right)^{\kappa-1} \Bigg|_{\rho = \rho_0} = \kappa \frac{p_0}{\rho_0} . \tag{3.13}$$

Boyle's law defines a relation between the pressure p, the density ρ and the absolute temperature T also using the gas constant $R = 8.314472\ J\ (mol\ K)^{-1}$ and the molecular weight M of the gas:

$$\frac{pM}{\rho} = RT \tag{3.14}$$

With (3.14) equation (3.13) is evaluated to

$$c^2 = \frac{\kappa R}{M} T . \tag{3.15}$$

In Table 3.1 the molecular weights and the specific heat ratios are shown for several gases together with the resulting speed of sound at $T = 273\ K$.

Gas	Molecular weight M [kg/mol]	Specific heat ratio κ	Speed of sound c [m/s]
Oxygen O_2	$32 \cdot 10^{-3}$	1.4	315.0
Hydrogen H_2	$2.016 \cdot 10^{-3}$	2.02	1507.7
Nitrogen N_2	$28.02 \cdot 10^{-3}$	1.4	336.7
"Air"	$28.97 \cdot 10^{-3}$	1.4	331.1

Table 3.1: Molecular weight M, specific heat ratio κ and speed of sound c
for oxygen, hydrogen, nitrogen and air

As shown in equation (3.15) in case of ideal gases the speed of sound only depends on the temperature and on the properties of the (ideal) gas and not on the ambient pressure. In chapter 3.1.3 the impact of pressure on the velocity c in case of real gas is discussed.

A rough estimation of the speed of sound gives the derivation of equation (3.15)

$$\frac{dc}{dT} = \frac{1}{2}\sqrt{\frac{\kappa\,R}{M\,T}}\,,$$ (3.16)

that allows to calculate the relative change of the speed of sound depending on the temperature to

$$\frac{\frac{dc}{dT}}{c} = \frac{1}{2\,T} \approx 0.17\,\frac{\%}{K}.$$ (3.17)

3.1.1.3 Approximation of speed of sound c in air

In [Cra93] the dependencies of speed of sound c and the specific heat ratio κ on the properties of the ambient air are analyzed. These are the temperature T, the relative humidity RH, the static pressure p_0 and the mole fraction x_c of CO_2 in air. To simplify the calculation, instead of the relative humidity RH, the water vapor mole fraction x_W is introduced. In the following, an approximation of the speed of sound c and the specific heat ratio κ, valid in the parameter ranges shown in Table 3.2 to keep the overall uncertainty less than 320 ppm, is given.

Property	min	max
Temperature T	0 °C	30 °C
Ambient pressure p_0	75 kPa	102 kPa
Mole fraction H_2 x_w	0 %	6 %
Mole fraction CO_2 x_c	0 %	1 %

Table 3.2: Ranges for the approximation formula given in (3.18) for the speed of sound

The following approximation formula can be used to calculate both the specific heat ratio κ and the speed of sound c for any combination of environmental factors within the given range (T is the temperature in degrees centigrade, p_0 the ambient pressure, x_w the water vapor mole fraction, and x_c the CO_2 mole fraction):

$$f\left(T, p_0, x_w, x_c\right) = a_0 + a_1 T + a_2 T^2 + \left(a_3 + a_4 T + a_5 T^2\right)x_w +$$
$$+ \left(a_6 + a_7 T + a_8 T^2\right)p_0 + \left(a_9 + a_{10}T + a_{11}T^2\right)x_c +$$ (3.18)
$$+ a_{12}x_w^2 + a_{13}p_0^2 + a_{14}x_c^2 + a_{15}x_w p_0 x_c$$

The coefficients of equation (3.18) are given in Table 3.3.

The value x_w is obtained by using the method given in [Gia82] to calculate the fraction of water vapor in air on a real gas basis, where HW is the relative humidity expressed as a fraction, f_e the enhancement factor, p_{sv} the saturation vapor pressure of water vapor in air and p_0 the static pressure:

$$x_w = \frac{HW \, f_e \, p_{sv}}{p_0} \tag{3.19}$$

The enhancement factor f_e is evaluated to

$$f_e = 1.00062 + 3.14 \cdot 10^{-8} p_0 + 5.6 \cdot 10^{-7} T^2 \tag{3.20}$$

using the temperature T in [°C]. The saturation vapor pressure of water vapor p_{sv} is found to be

$$p_{sv} = e^{1.2811805 \cdot 10^{-5} T_{abs}^2 - 1.9509874 \cdot 10^{-2} T_{abs} + 34.04926034 - 6.3536311 \cdot 10^3 T_{abs}^{-1}} Pa \tag{3.21}$$

using the absolute temperature T_{abs}. Equations (3.19) to (3.21) are valid over the temperature range 0°C to 30°C (273.15 K to 303.15 K) and for the pressure range *60 kPa* to *110 kPa*.

Coefficients	Speed of sound c	Specific heat ratio κ
a_0	331.5024	1.400822
a_1	0.603055	$-1.75 \cdot 10^{-5}$
a_2	-0.000528	$-1.73 \cdot 10^{-7}$
a_3	51.471935	-0.0873629
a_4	0.1495894	-0.0001665
a_5	-0.000782	$-3.26 \cdot 10^{-6}$
a_6	$-1.82 \cdot 10^{-7}$	$2.047 \cdot 10^{-8}$
a_7	$3.73 \cdot 10^{-8}$	$-1.26 \cdot 10^{-10}$
a_8	$-2.93 \cdot 10^{-10}$	$5.939 \cdot 10^{-14}$
a_9	-85.20931	-0.1199717
a_{10}	-0.228525	-0.0008693
a_{11}	$5.91 \cdot 10^{-5}$	$1.979 \cdot 10^{-6}$
a_{12}	-2.835149	-0.01104
a_{13}	$-2.15 \cdot 10^{-13}$	$-3.478 \cdot 10^{-16}$
a_{14}	29.179762	0.0450616
a_{15}	0.000486	$1.82 \cdot 10^{-6}$

Table 3.3: Coefficients for calculating the speed of sound c and the specific heat ratio κ according to equation (3.18)

The overall uncertainty in the specific heat ratio is estimated to be less than 320 ppm and the uncertainty in the speed of sound is similarly estimated to be less than 300 ppm.

3.1.2 Temperature

The ambient temperature T provides the strongest impact on the speed of sound c and also strongly influences the impact of the other parameters. In Figure 3.2 the speed of sound c is plotted over the valid range of temperatures $0°C \leq T \leq 30°C$ for different values of relative humidity (*HW = 0 %, 30 %, 60 %* and *90 %*).

In Table 3.4 some results are shown for two different values of relative humidity (with ambient pressure $p_0 = 75\ kPa$ and CO_2-concentration $x_c = 0\ \%$): in case of $HW = 0\ \%$ the speed of sound varies from $c_{T=0°C, 0\%} = 331.49\ m/s$ to $c_{T=30°C, 0\%} = 349.17\ m/s$ which is a variation of about 5.33 %. With increasing relative humidity the influence increases to about 6.14 %. The relative changes shown in Table 3.4 relate to $c_{T=0°C, 0\%} = 331.49\ m/s$ (gray shaded).
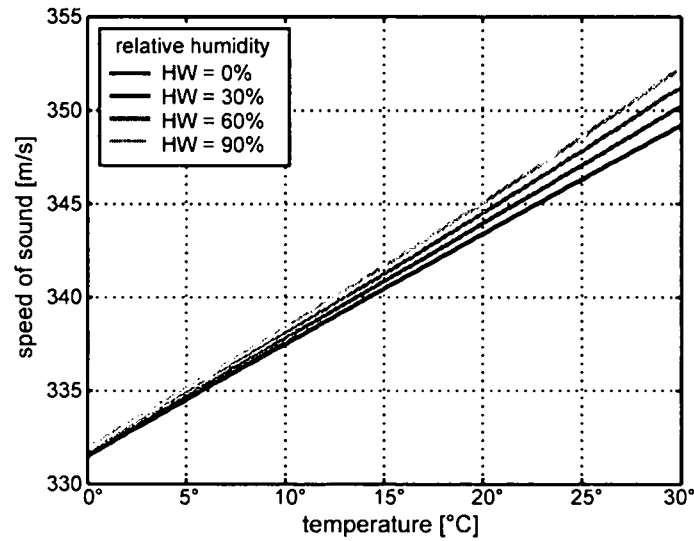
Figure 3.2: Dependence of speed of sound c on temperature and relative humidity HW

	relative humidity $HW = 0\ \%$		relative humidity $HW = 100\ \%$	
Temperature T	Speed of sound c [m/s]	Relative change	Speed of sound c [m/s]	Relative change
0 °C	331.49	0 %	331.90	0.13 %
10 °C	337.49	1.81 %	338.35	2.07 %
20 °C	343.38	3.59 %	345.06	4.09 %
30 °C	349.17	5.33 %	352.27	6.27 %

Table 3.4: Influences of temperature T on the speed of sound c
depending on relative humidity HW

Mean gradients are found to be about

$$\left.\frac{\partial c}{\partial T}\right|_{HW=0\%} = 0.59\,\frac{m/s}{K}, \text{ and } \left.\frac{\partial c}{\partial T}\right|_{HW=100\%} = 0.68\,\frac{m/s}{K}.$$

3.1.3 Pressure

In case of low relative humidity the pressure has a minor impact on the speed of sound. However, the influence strongly depends on the actual ambient temperature T: therefore, the relative change of the speed of sound for the valid pressure range $75\ kPa \le p_0 \le 102\ kPa$ with

respect to the speed of sound at $p_0 = 75\ kPa$ is plotted for several temperatures T. As shown in Figure 3.3 a relative change of several $10\ ppm$ is expected in case of $HW = 0\ \%$.
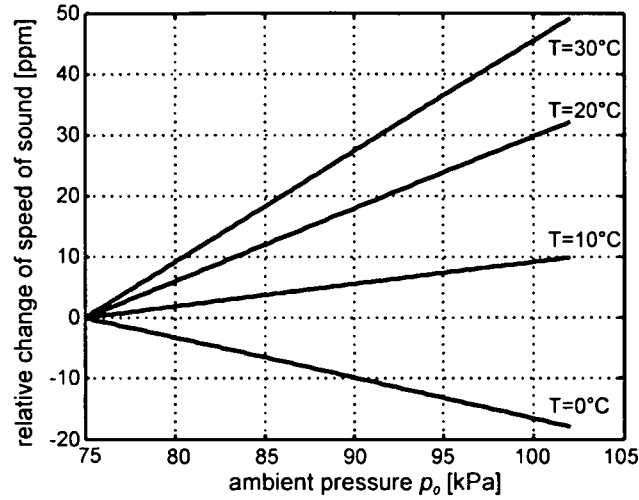
Figure 3.3: Influence of ambient pressure p_0 on the speed of sound c depending on the ambient temperature T at $HW = 0\ \%$

With increasing relative humidity the influence of the pressure increases rapidly: as shown in Figure 3.4, at $T = 30°C$ a full range change of more than $0.2\ \%$ is found.
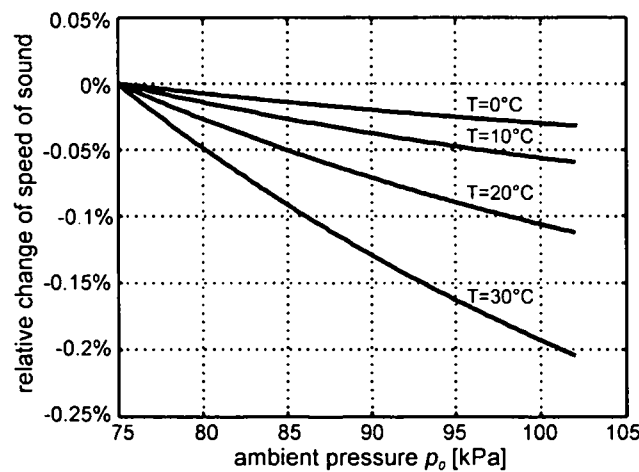
Figure 3.4: Influence of pressure p_0 at high relative humidity $HW = 90\ \%$

The gradient strongly depends on the ambient temperature T and the relative humidity HW. In Table 3.4 the mean gradients of the speed of sound $\partial c/\partial p_0$ depending on different values of temperature and relative humidity are shown.

Temperature T	relative humidity HW = 0 %		relative humidity HW = 90 %	
	Full range change [m/s]	Gradient [m/s/kPa]	Full range change [m/s]	Gradient [m/s/kPa]
0 °C	-0.0059	$-2.185 \cdot 10^{-4}$	-0.0169	$-6.271 \cdot 10^{-4}$
10 °C	0.0033	$1.222 \cdot 10^{-4}$	-0.2008	$-7.435 \cdot 10^{-3}$
20 °C	0.0110	$4.074 \cdot 10^{-4}$	-0.3868	$-1.433 \cdot 10^{-2}$
30 °C	0.0172	$6.370 \cdot 10^{-4}$	-0.7191	$-2.663 \cdot 10^{-2}$

Table 3.5: Influences of the ambient pressure p_0 on the speed of sound c depending on the ambient temperature T

3.1.4 Humidity

The temperature also strongly influences the impact of the relative humidity HW on the speed of sound c. In Figure 3.5 the relative change of the speed of sound depending on the relative humidity HW and on the temperature T is shown.

Temperature T	pressure $p_0 = 75kPa$		pressure $p_0 = 102kPa$	
	Full range change [m/s]	Gradient [m/s/%HW]	Full range change [m/s]	Gradient [m/s/%HW]
0 °C	0.416	$4.159 \cdot 10^{-3}$	0.303	$3.032 \cdot 10^{-3}$
10 °C	0.859	$8.591 \cdot 10^{-3}$	0.626	$6.263 \cdot 10^{-3}$
20 °C	1.675	$1.675 \cdot 10^{-2}$	1.222	$1.222 \cdot 10^{-2}$
30 °C	3.103	$3.102 \cdot 10^{-2}$	2.263	$2.263 \cdot 10^{-2}$

Table 3.6: Influences of the relative humidity HW on the speed of sound c depending on the ambient temperature T
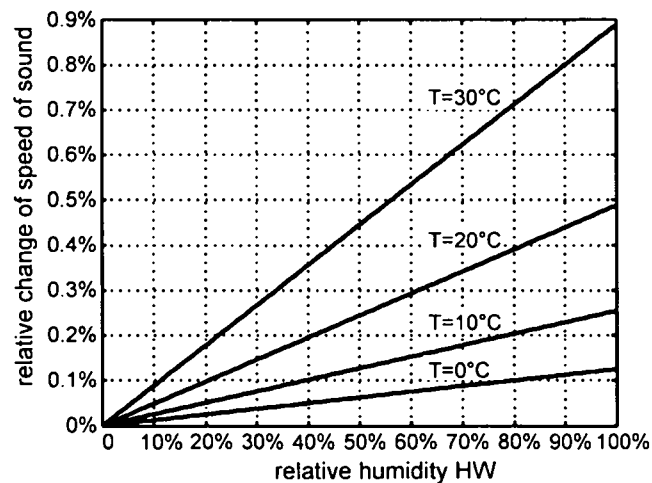
Figure 3.5: Influence of the relative humidity HW on the speed of sound c depending on the ambient temperature T at pressure $p_0 = 75\ kPa$

With increasing temperature the influence of the relative humidity rises. In Table 3.6 the full scale range of the speed of sound and the mean gradient at several ambient temperatures are shown.

The influence of the relative humidity HW on the speed of sound also depends on the ambient pressure p_0: with increasing pressure the influence decreases as shown in right part of Table 3.6.

3.1.5 CO$_2$ Concentration

The CO_2 concentration has a relatively strong impact on the speed of sound with a mean gradient of about $-0.9\ m/s/\%CO_2$. It is only slightly affected by ambient temperature and relative humidity. In Figure 3.6 the impact of the relative humidity HW at a temperature of $T = 30\ ^\circ C$ is shown.
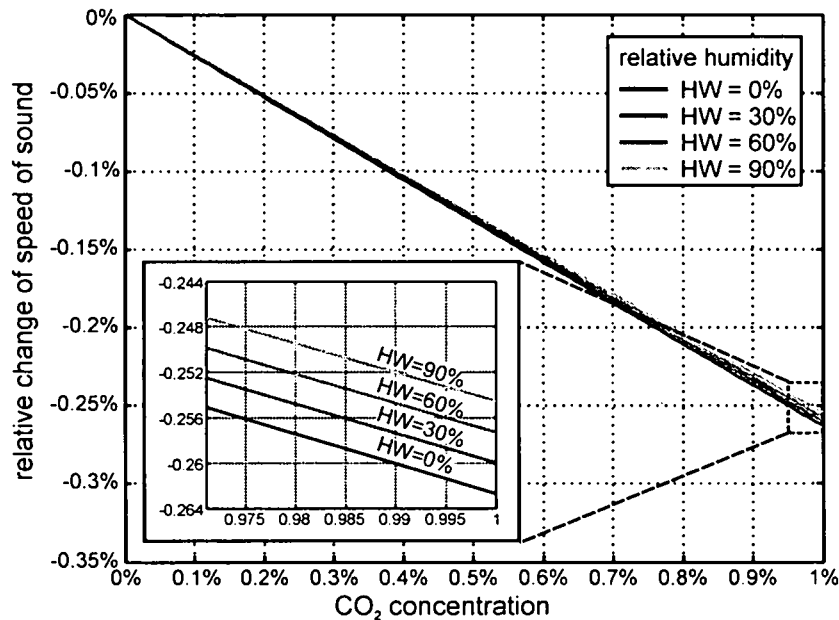
Figure 3.6: Influence of CO_2 concentration on speed of sound c
depending on relative humidity HW at temperature $T = 30^\circ C$ and pressure $p_0 = 75kPa$

The maximum deviation due to relative humidity is about $80\ ppm$ and the deviation due to temperature change is in a similar range of about $60\ ppm$.

3.1.6 Nonlinear effect of the speed of sound

In case of high acoustic amplitudes a nonlinear effect of the speed of sound is found (according to [Kut88]). Basically, the final speed of sound towards ground is the sum of the speed of sound in the medium c and the medium velocity towards ground. In case of longitudinal waves a movement of the medium is caused by the propagating wave itself. This movement is previously mentioned sound particle velocity v_x. Therefore, the final speed of sound c_{NL} is defined to

$$c_{NL} = c + v_x.\qquad(3.22)$$

The definition of the speed of sound in equation (3.6) is based on discarding high order components of equation (3.5). As mentioned there, this simplification is valid for low changes of the density ρ (relative to the static density ρ_0). In the following, the second order term is also evaluated to discuss the resulting nonlinearity in case of a plain acoustic wave.

Similar to equation (3.6) the speed of sound c_2 is defined as

$$c_2^2 = \left(\frac{dp}{d\rho}\right)_{\rho_0} + \left(\frac{d^2 p}{d\rho^2}\right)_{\rho_0} \rho = c^2 + \left(\frac{d^2 p}{d\rho^2}\right)_{\rho_0} \rho, \qquad (3.23)$$

which also takes the second order term into account. Using equation (3.12), the second order term is evaluated to

$$\left(\frac{d^2 p}{d\rho^2}\right)_{\rho_0} = \kappa(\kappa-1)\frac{p_0}{\rho_0^2}\left(\frac{\rho}{\rho_0}\right)^{\kappa-2}\Bigg|_{\rho=\rho_0} = \kappa(\kappa-1)\frac{p_0}{\rho_0^2} = c^2\frac{(\kappa-1)}{\rho_0}, \qquad (3.24)$$

and the speed of sound c_2 is calculated to

$$c_2^2 = c^2\left[1+(\kappa-1)\frac{\rho}{\rho_0}\right]. \qquad (3.25)$$

In case of a plane wave propagating in x-direction the density ρ is proportional to the acoustic particle velocity v_x [Zol98]

$$\rho = \frac{\rho_0}{c}v_x. \qquad (3.26)$$

The second order approximation of the speed of sound c_2 is shown in equation (3.27), where the speed of sound depends on the actual sound particle velocity v_x.

$$c_2(v_x) = c\sqrt{1+(\kappa-1)\frac{v_x}{c}} \approx c + \frac{\kappa-1}{2}v_x \qquad (3.27)$$

With equation (3.22), the final nonlinear speed of sound c_{NL} is found to

$$c_{NL} = c_2 + v_x = c + \frac{\kappa+1}{2}v_x \approx c + 1.2\,v_x. \qquad (3.28)$$

The specific heat ratio of air is about $\kappa = 1.4$ (compare Table 3.1) which allows the latter approximation in equation (3.27). Therefore, signal parts with higher sound particle velocities propagate faster than others with lower velocities. This leads to deformations of the transmitted acoustic signal as shown in the following: a primarily sinusoidal signal (see Figure 3.7/a) becomes increasingly steeper on its front because signal parts providing higher amplitudes are faster than others. When the wave front finally has a vertical tangent (compare Figure 3.7/b), a discontinuity is reached which is called pressure front. The distance x_{pf}, where the pressure front is found the first time, is calculated to

$$x_{pf} = \frac{c^2}{\hat{v}\, 2\pi\, f\left(\dfrac{k-1}{2}\right)} = \frac{c^2}{\hat{v}\,\pi\, f\left(k-1\right)}\,. \tag{3.29}$$

It depends on the peak value $\hat{v}$ of the sound particle velocity, the frequency f, the wave number k and the speed of sound c. As an acoustic wave cannot roll over, during further propagation the vertical part of the wave front increases until a triangle shaped signal form is reached (Figure 3.7/c). This case takes place when the maximum of the signal reaches the position of the pressure front and is expected at the distance $x_{triangle}$ calculated to

$$x_{triangle} = \frac{c^2}{\hat{v}\,4\, f\left(\dfrac{k-1}{2}\right)} = x_{pf}\cdot\frac{\pi}{2}\,. \tag{3.30}$$
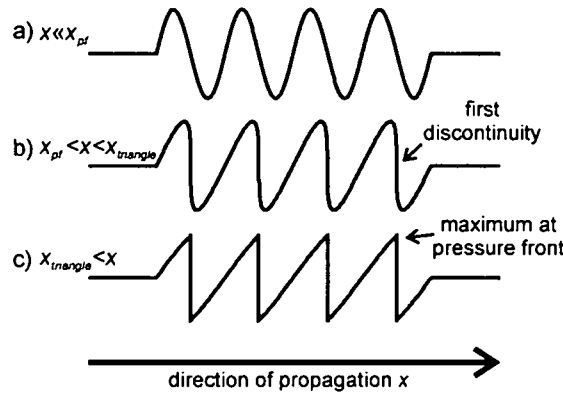
Figure 3.7: Schematic of the non linearity occurring during propagation:
a) undisturbed, b) first discontinuity and c) triangle shaped signal

In the following an example of this effect is shown and its practical influence is discussed: assuming a signal with a sound pressure level of $L = 120\,dB$, the acoustic pressure $\tilde{p}$ is calculated according

$$L = 20\,\lg\left(\frac{\tilde{p}}{p_{ref}}\right)dB \tag{3.31}$$

with a reference level of $p_{ref} = 20\,\mu Pa$ to $\tilde{p} = 20\,Pa$. In case of a plane wave the acoustic pressure p and the sound particle velocity v are connected by the characteristic wave impedance Z_0 according to

$$Z_0 = \frac{\tilde{p}(x,t)}{\tilde{v}_x(x,t)} = \rho\cdot c\,, \tag{3.32}$$

which is a real value of about $Z_0 = 414\,Ns\cdot m^{-3}$ in air. This allows calculating the peak value of the sound particle velocity v to

$$\hat{v} = \frac{\tilde{p}\sqrt{2}}{Z_0} = \frac{20\,\dfrac{N}{m^2}\,\sqrt{2}}{414\,\dfrac{Ns}{m^3}} \approx 0,07\,\frac{m}{s} \,.$$ (3.33)

Assuming a signal frequency of $f = 50\,kHz$, the distance, where the first discontinuity is expected, is derived to $x_{pf} = 26\,m$ and a triangle shaped signal form is reached at $x_{triangle} = 41\,m$. Ultrasonic distance measurement systems can be used to measure distances in this range and also the sound pressure level used in this example may be reached. However, also the following considerations must be regarded: the previously presented calculation assumes no transmission loss and, therefore, constant signal amplitude during the transmission path. However, this is not valid for ultrasonic signals which are strongly damped in air with the damping factor of about

$$D \approx 1.6 \cdot 10^{-10} f^2 \,\frac{dB}{m} \,.$$ (3.34)

The signal deformation leads to additional harmonic signal frequencies. According to equation (3.34) the damping factor is proportional to the square of the frequency and, therefore, harmonic frequencies of higher orders are damped even more, which means that damping results in a decrease of nonlinearity.

Due to these considerations the nonlinear effect can be mostly neglected in ultrasonic distance measurement applications with growing propagation distances.

3.1.7 Air movement (wind)

Although wind is not a physical property of air, it strongly influences the speed of ultrasonic signals in relation to fixed devices and objects. Due to the relative low speed of sound wind has a strong impact on the achievable results of ultrasonic distance measurement systems and is, therefore, discussed in this chapter. Details can be found in [Elm00], the essential results are shown in the following.
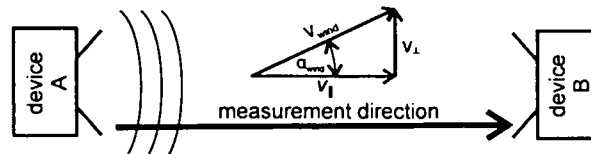
Figure 3.8: Wind velocity v_{wind} and its vectorial components $v_\parallel$ and $v_\perp$
in relation to the measurement direction in case of an A-B-measurement system

Generally the influence of wind depends on its direction in relation to the measurement direction. In this context the wind velocity v_{wind} is split into two components $v_\parallel$ and $v_\perp$ (compare Figure 3.8).

3.1.7.1 Wind parallel to the direction of measurement in one way measurement systems

In case of an A-B-measurement system (see chapter 2.1), where the ultrasonic signal runs only once through the measurement distance, the vectorial part $v_\parallel$ influences the speed of the signal v_{sig} with respect to the ground and the basic speed of sound c is changed to

$$v_{sig} = c + v_\parallel \tag{3.35}$$

This leads to a relative distance measurement error $e_{\parallel,1\text{-}way}$ of

$$e_{\parallel,1\text{-}way} = -\cfrac{1}{\cfrac{c}{v_\parallel} + 1} \tag{3.36}$$

A wind amount in measurement direction of $v_\parallel = 10\ m/s$, therefore, produces a relative measurement error of $e_{\parallel,1\text{-}way} = -2.9\ \%$.

3.1.7.2 Wind parallel to the direction of measurement in two way measurement systems

In passive and active reflection systems (chapter 2.2 and 2.3) the signal runs twice through the measurement direction, once in each direction. As a consequence the vectorial part of the wind along the measurement direction influences the speed of the signal twice, but with different sign:

$$\begin{aligned} v_{sig1} &= c + v_\parallel \\ v_{sig2} &= c - v_\parallel \end{aligned} \tag{3.37}$$

This leads to a strong compensation effect and to the relative measurement error

$$e_{\parallel,2\text{-}way} = \cfrac{1}{\cfrac{c^2}{v_\parallel^2} - 1} \approx \underbrace{\frac{v_\parallel^2}{c^2}}_{v_\parallel \ll c}. \tag{3.38}$$

The latter simplification is valid for low speed of wind $v_\parallel$ compared to the speed of sound c. A wind of $v_\parallel = 10\ m/s$ leads in this case to a relative error of only $e_{\parallel,2\text{-}way} = 0.092\ \%$, which moreover is independent of the direction of the wind.

3.1.7.3 Wind perpendicular to the direction of measurement

The vectorial part of the wind $v_\perp$ influences both topologies, 1-way and 2-way, identically: this part does not change the speed of the signal in relation to the surroundings, but shifts the ultrasonic signal normal to the measurement direction resulting in an elongation of the measured distance. This relative error $e_\perp$ resulting from this elongation is found to be

$$e_\perp = \frac{1}{\sqrt{1 - \frac{v_\perp^2}{c^2}}} - 1 \approx \underbrace{\frac{1}{2}\frac{v_\perp^2}{c^2}}_{v_\perp \ll c}. \tag{3.39}$$

A wind of $v_\perp = 10\,m/s$ across the measurement direction leads to a relative error of $e_\perp = 0.046\,\%$.

3.1.7.4 Summary

In Figure 3.9 the relative measurement errors are plotted versus the wind velocity for the previous mentioned cases: the dashed line shows the large error occurring at topologies using one way measurement with wind along the measurement direction $e_{\parallel, 1way}$. In this case the error is about the ratio between the velocities of sound c and wind $v_\parallel$. Due to the compensating effect of topologies providing two way measurements, the error stays much lower (black solid: $e_{\parallel, 2way}$). Moreover, it is independent of the direction of the wind (whether the velocity is positive or negative according to Figure 3.9). The lowest error is found due to wind across the measurement direction $v_\perp$ (solid gray). In this case it does not matter if there is a one or two way measurement system and it is only dependent of the absolute value of the wind velocity in measurement direction.
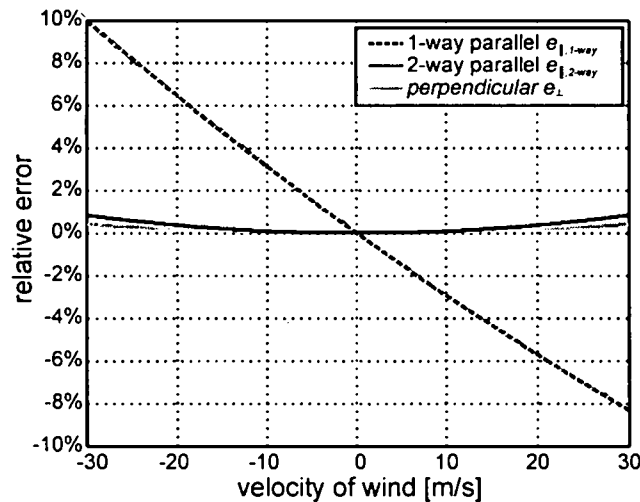
Figure 3.9: Relative error of distance measurement depending on wind velocity

Figure 3.9 shows the influences of the vectorial wind components $v_\parallel$ and $v_\perp$ separately. In the following the influence of arbitrary wind directions is analyzed. A wind velocity of $v_{wind} = 10\,m/s$ is assumed and according to the actual direction α_{wind} the two vectorial parts $v_\parallel$ and $v_\perp$ are calculated and their combined impact to the measurement result is evaluated.

In case of one way measurement the measurement error is dominated by the wind along the measurement direction $v_\parallel$. As shown in Figure 3.10 the measurement error e_{1-way} is in the range of about $\pm 3\,\%$ depending on the actual wind direction. To compensate this effect, both the wind velocity and the wind direction (relative to the measurement direction) must be known and considered.
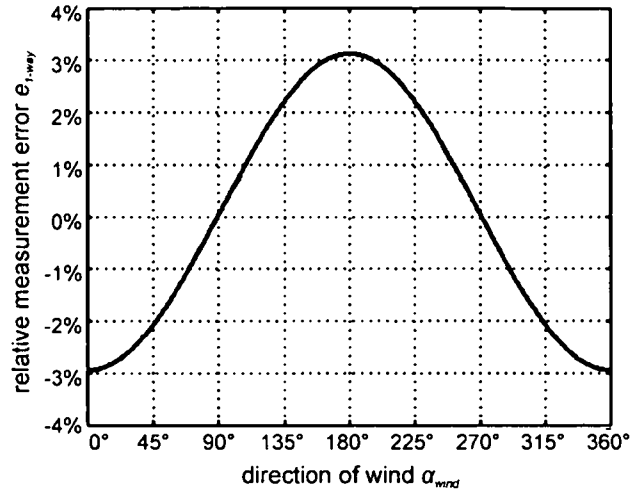
Figure 3.10: Relative error of distance measurement $e_{1\text{-}way}$ depending on wind direction α_{wind} in case of one way measurement at a wind velocity of *10 m/s*

In case of two way measurements the much smaller measurement error $e_{2\text{-}way}$ in the range $0.045\,\% < e_{2\text{-}way} < 0.095\,\%$ is found (see Figure 3.11). The limits of this range are the measurement errors obtained at the wind along the measurement direction $e_\parallel$ and the wind across $e_\perp$. As both errors are independent of the sign of the wind direction (always positive), the resulting error always has a positive sign, too.
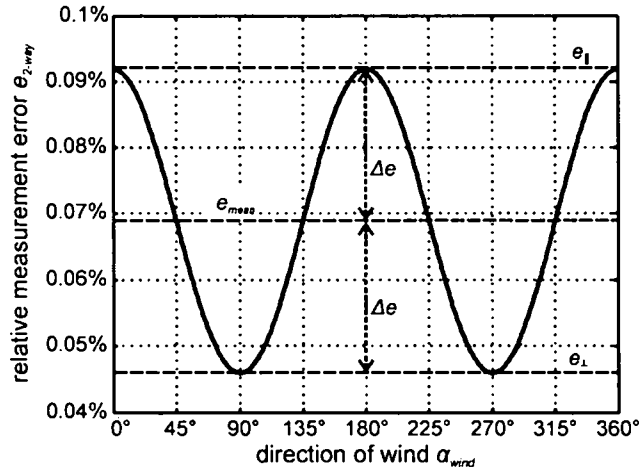
Figure 3.11: Relative error of distance measurement $e_{2\text{-}way}$ depending on wind direction α_{wind} in case of two way measurement at a wind velocity of *10 m/s*

A compensation of this effect is possible by measuring the speed of the wind v_{wind}. This allows calculating the minimal (wind perpendicular $e_\perp$) and the maximum (wind parallel $e_\parallel$) measurement error. Compensation of the mean error

$$e_{mean} = \frac{e_\parallel + e_\perp}{2} \approx \frac{3}{4} \frac{v_{wind}^2}{c^2} \tag{3.40}$$

leads to a residual measurement uncertainty $\pm\Delta e$ of

$$\Delta e = \frac{e_\parallel - e_\perp}{2} \approx \frac{1}{4} \frac{v_{wind}^2}{c^2}$$ (3.41)

In the previous shown example of $v_{wind} = 10$ m/s the mean error becomes $e_{mean} = 0.069$ %. After compensation of this mean error the residual measurement uncertainty is $\Delta e = 0.029$ % which is a good improvement compared to the uncompensated case where the maximum error is $e_\parallel = 0.092$ %.

3.2 Measurement properties

3.2.1 Resolution & Accuracy

The distance resolution of ToF based systems is given by the time resolution of the measurement of the point of time receiving the signal. Both, the resolution and the accuracy depend on the accuracy of the ToF measurement. However, the main influence to the accuracy is the accurate determination and the stability of the speed of sound c. In chapter 3.1 the physical parameters of the speed of sound are discussed. Inaccurate determination of the speed of sound leads to systematic measurement errors. Statistical errors are mainly based on local disturbances along the measurement distance. These occur due to turbulences by moving objects or persons or local temperature changes [Kle99]. Therefore, the achievable accuracy restricts the reasonable range of resolution.

3.2.2 Measurement rate

The measurement rate is mainly restricted by the relatively low speed of sound. Especially in cases where discrete measurement signals are used (burst method or most correlation based methods) a new measurement cycle must not start before the signals of previous measurement cycles are sufficiently damped to be not received any more. As shown in the following, the measurement rate strongly depends on the used signal processing method and also on the reflection properties of the measurement objects.

3.2.2.1 Well defined reflection properties, one signal type

Well defined reflection properties of the objects allow using receivers that are equipped with time dependent amplifiers to compensate the attenuation of the signal during its ToF. This is accomplished by either a time dependent amplifier that compensates the air attenuation or a time dependent threshold level taking into account the attenuation, which leads to a distance independent detection behavior of the receiver circuit. In Figure 3.12/a a measurement assembly is shown consisting of the measurement system and two objects at the distances d_1 and d_2. Object O_2 is located outside the maximum measurement range d_{max}.

In Figure 3.12/b a diagram of the measurement cycle is shown: the black line represents the signal amplitude that is at least necessary to trigger the receiver. Due to the time dependent amplifier this trigger level decreases during the ToF during the measurement cycle. Consider object O_1 at position d_1: it is located inside the measurement range d_{max} and its echo arrives at t_1. Its amplitude a_1 is above the actual trigger level and, therefore, object O_1 is detected by the receiver. In case of object O_2, arriving at t_2 at the receiver, the amplitude is much lower than the

trigger level because a new measurement cycle has already started and signals with higher amplitudes are expected. As a consequence the measuring rate is only restricted by the ToF to the farthest object.
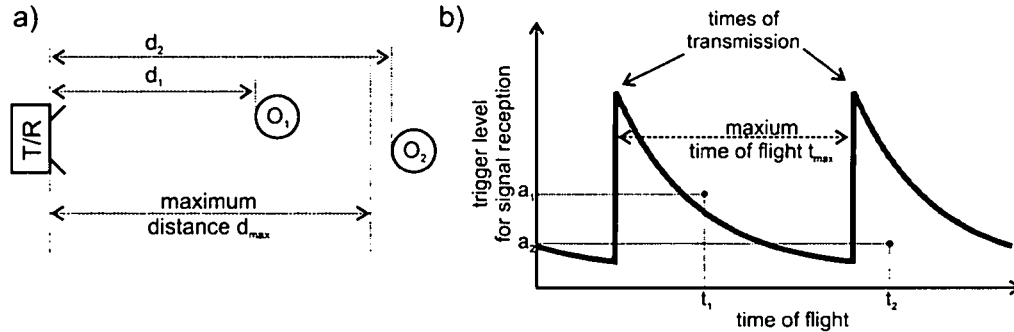
Figure 3.12: a) Measurement assembly consisting of measurement system and two objects, whereas object O_2 is located outside the measurement range
b) corresponding measurement diagram with resulting amplitude threshold
and reflections of both objects, whereas O_2 is not detected

3.2.2.2 Arbitrary reflection properties, one signal type

As shown in chapter 3.3.1 the reflection properties of objects can strongly differ especially due to different geometric shapes. Without a priori knowledge of the reflection properties of each object the echo amplitudes are unpredictable as shown in the following.
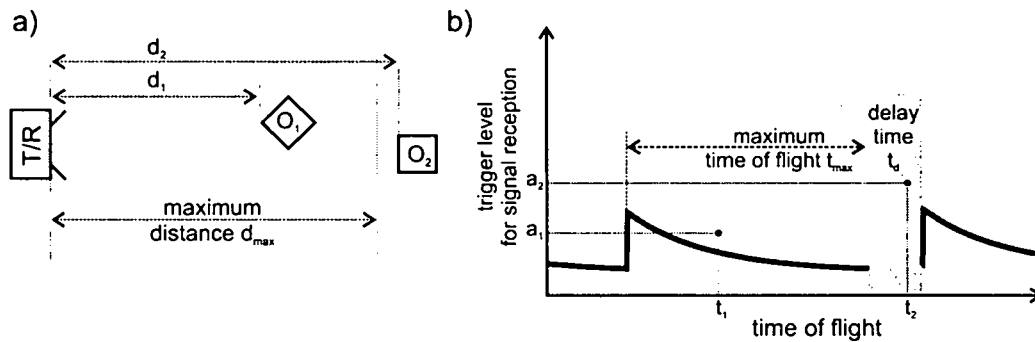
Figure 3.13: a) Measurement assembly with objects providing strongly different reflection properties, b) corresponding diagram of measurement cycle

In Figure 3.13/a a measurement assembly with two objects providing strongly different reflection properties and in Figure 3.13/b the diagram of a measurement cycle are shown. The assumption of weakly reflecting objects (as object O_1) requires high amplification of the incoming signal and a low detection threshold, respectively. Object O_1 is detected at t_1 according to its distance d_1. Although object O_2 is located farther away at d_2 outside the measurement range, its echo amplitude would be high enough to trigger the receiver. Therefore, a delay time is introduced that must be long enough to attenuate all signals below the detection threshold. The length of the delay time depends on the expected variations of the reflection factors of the objects. The larger the differences are, the longer is the required delay time. The

resulting measurement rate is, therefore, restricted by the sum of the maximum ToF t_{max} and the necessary delay time t_{delay}.

3.2.2.3 Use of coded signals

A solution that helps to overcome a limitation of the measurement rate by the ToF (to the farthest object) is the use of differently coded signals in adjacent measurement cycles. This, of course, is only possible in systems where coding of signals is supported (e.g. correlation based systems). The principle how the measurement rate is improved by coded signals is presented in chapter 3.4.1. However, increasing the measurement rate beyond one signal propagation time in the air channel requires the use of a different transmitter and receiver.

3.2.2.4 Use of continuous signals

Other measurement systems based on continuous waves do not define a measurement rate principally. Mostly the measurement rate occurs due to the block oriented signal processing algorithm (e.g. Fast Fourier Transform FFT). Assuming real time evaluation of the received signal without calculation delays, only the ToF causes a delay of the measurement result, but continuous measurements are possible. A system providing not yet continuous but a very high measurement rate based on this principle is found in [Tes89].

3.2.2.5 General considerations

Especially in case of closed loop systems that require measurement results at equidistant times, ultrasonic systems are not easy to implement: even in the case of high measurement rates as described before, the actual measurement results are always delayed according to the object distance, which inhibits equidistant measurement results. Therefore, closed loop systems, whose cycle times are in the range of the ToF, require sophisticated jitter compensation algorithms.

3.2.3 Multi path propagation

Ultrasonic distance measurement systems mostly intend to measure the direct distance (line of sight) to an object. However, due to the relative wide radiation pattern of transducers and the good reflection properties of most materials, in case of multiple objects multi path propagation is possible. Multi path propagation means that the ultrasonic signal is reflected at more than one object and, therefore, two or more points of reflection are found. In the following, reasons for multi path propagation are discussed and their effects to the measurement results are shown. The discussion is based on the principle of virtual sources (see chapter 3.3.2).

Assuming an environment containing n objects and allowing a total number of l reflections, the total number of reflection paths is limited to

$$p = K_i \, K_a \, n(n-1)^{l-1} , \qquad (3.42)$$

where K_i and K_a are pruning constants (according to [McK96]). Due to the transducer directivity not all objects are located inside the region of insonification and audition (compare Figure 3.19 on page 29): assuming i objects lying in the region of insonification and a objects in the region of audition, the pruning constants are defined to

$$K_l = \frac{i}{n} \text{ and } K_a = \frac{a}{n} + 1.$$

(3.43)

In case of two objects ($n = 2$) and one possible reflection ($l = 1$), the number of theoretically possible reflection paths is $p = 2$ (one line of sight measurement to each object).
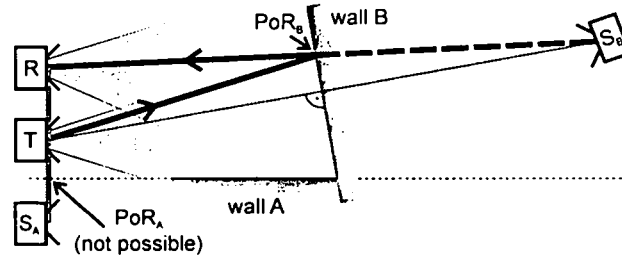
Figure 3.14: Arrangement of two walls and resulting reflection paths
in case of one possible reflection ($l = 1$)

As example, an arrangement of two walls is discussed in the following (Figure 3.14 and Figure 3.15): at first the reflection on wall B is considered: the method of virtual sources allows introducing the virtual source S_B as mirrored transmitter T (see Figure 3.14) to replace the reflection path with an A-B-measurement (virtual source S_B to receiver R). The intersection between this direct transmission path S_B - R with the surface of wall B leads to the PoR_B and the first reflection path T - PoR_B - R is found (solid black line in Figure 3.14). In the second case the virtual source S_A is introduced at the mirrored position of the transmitter T at wall A. The direct transmission path S_A - R does not lead to a valid PoR_A because firstly there is no intersection between the direct transmission path and the surface of wall A and secondly PoR_A would lay outside the ranges of insonification and audition of the transmitter T and receiver R (see chapter 3.3.2).
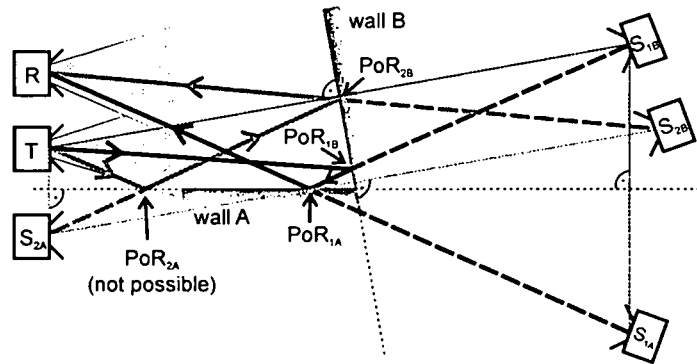
Figure 3.15: Arrangement of two walls and resulting reflection paths
in case of two possible reflections ($l = 2$)

In case of two possible reflections ($l = 2$) equation (3.42) delivers also 2 theoretically possible reflection paths. Let's consider the first case $T - wall\,B - wall\,A - R$: according to Figure 3.15 there are two virtual sources S_{1A} and S_{1B}, whereas S_{1B} is on the mirrored position of the initial source T at the wall B. The second virtual source S_{1A} (S_{1B} mirrored at wall A) simplifies the whole reflection path to a direct transmission S_{1A} - R. This finally leads to the reflection points

PoR_{1A} and PoR_{1B} that are both located on the object surfaces and are in the ranges of insonification and audition. The solid black line in Figure 3.15 shows the resulting transmission path.

The second theoretically possible transmission path with the first reflection on wall A and the second on wall B fails because the reflection point PoR_{2A} is not located on the object surface and, therefore, no valid second transmission path is obtained (compare solid gray line in Figure 3.15).

The main problems of multiple reflection paths are the following:

- If measurements are taken only from one position, it is not possible to distinguish between echoes occurring due to multiple reflecting objects or due to different reflection paths of echoes from one object. In some works multipath reflections are recognized by systematic measurements from several positions. In [Bor95] an error eliminating algorithm for crosstalk based on multipath propagation is shown.

- Multipath reflections are often the reason for very narrow spaced and even overlapping echoes. One example is long distance measurement in narrow rooms where the length of the line of sight differs only slightly from the length of multipath ways. Correct evaluation of the overlapping echoes requires very powerful echo separation capabilities in this case.

3.3 Object dependence of measurements

Ultrasonic distance measurements strongly depend on the properties of the reflecting objects. In the following, these aspects are discussed.

3.3.1 Reflection properties

In passive reflection topologies the reflection properties of the object are crucial to the achievable results obtained by the system. In the following different aspects of reflection properties, the material properties and the surface properties are discussed.

3.3.1.1 Material properties

In general, a reflection always takes place when the acoustic impedance $Z = \rho \cdot c$ of the medium, where ρ is the mass density and c the speed of sound, changes [Pap99]. As shown in Figure 3.16 an incoming signal with the pressure amplitude P_i arrives at a border where the acoustic impedance changes from Z_1 to Z_2. Part of the signal with amplitude $P_r = R_p \cdot P_i$ is reflected while another part of the signal $P_t = T_p \cdot P_i$ is transmitted through the border to the other medium.
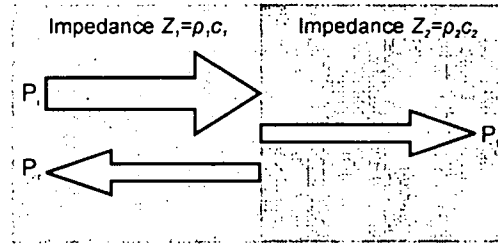
Figure 3.16: Schematic of impedance change from Z_1 to Z_2
with incoming signal amplitude P_i, reflected amplitude P_r and transmitted amplitude P_t

Knowing the impedances Z_x of both media, the pressure reflection coefficient R_p and the pressure transmission coefficient T_p are calculated to

$$R_p = \frac{Z_2 - Z_1}{Z_2 + Z_1}$$

$$T_p = \frac{2 Z_1}{Z_2 + Z_1}$$

(3.44)

In the following Table 3.7 the speed of sound and the acoustic impedances of several different materials are shown. Furthermore, the pressure reflection factor R_p is calculated which occurs at the border from air to the specific material.

It is obvious in Table 3.7 that most materials provide a reflection coefficient of $R_p \approx 1$ and are therefore called "acoustically hard" materials with nearly ideal reflection properties. As a consequence in most cases the reflection coefficient can be assumed to be $R_p = 1$.

Material	Speed of sound [m/s]	Acoustic impedance [MRayls]	R_p
Air	330	0.00004	0
Water	1480	0.148	0.999460
Concrete	3650	0.84	0.999905
Lead	2160	2.462	0.999968
Stainless Steel	5790	4.516	0.999982

Table 3.7: Properties of different materials as speed of sound c and acoustic impedance and the reflection factor R_p occurring at the boundary of air and several materials

3.3.1.2 Surface properties

The reflection properties of surfaces depend on the roughness of the surface compared with the wavelength of the ultrasonic signal. In literature surfaces are differentiated in smooth/rough surfaces [Kao00] or even smooth/moderate/rough surfaces [Boz92] [Pol99]. Decisive to the classification are the heights of the surface roughness. A surface is called smooth when the surface heights σ_s are much smaller than the wavelength λ of the incident signal: $\sigma_s << \lambda$. In this case only specular reflection (angle of incidence is equal to angle of reflection) takes place. In case of rough surfaces ($\sigma_s >> \lambda$) only diffuse reflections occur: an incoming signal is spread in each direction independent of the angle of incidence (compare Figure 3.17).

a) specular reflection
at smooth surface

b) diffuse reflection
at rough surface
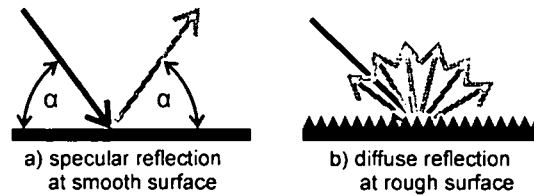
Figure 3.17: Reflections on a) smooth and b) rough surface

Moderate rough surfaces ($\sigma_s \approx \lambda$) provide both, specular and diffuse reflections. Smooth surfaces on the one hand reflect all signal energy in one specific direction and high signal amplitudes are expected, while in other directions nothing is emitted. On the other hand rough surfaces spread the incoming signal energy in every direction but with much lower amplitude.

A lot of work was done in empirically determining and modeling these effects to be able to implement this information to real measurement models [Kao00].

3.3.2 Object dependence

In the following discussion all surfaces are considered to be sufficiently smooth to provide only specular reflection. In literature three basic object types are proposed [Bar90] as shown in Figure 3.18. Similar to different surface properties some provide specular (plane and corner) and others diffuse reflection (edge).

a) plane   b) edge   c) corner
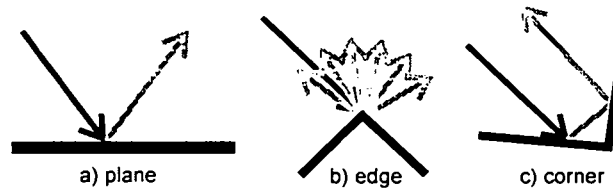
Figure 3.18: Basic object types: a) plane, b) edge and c) corner
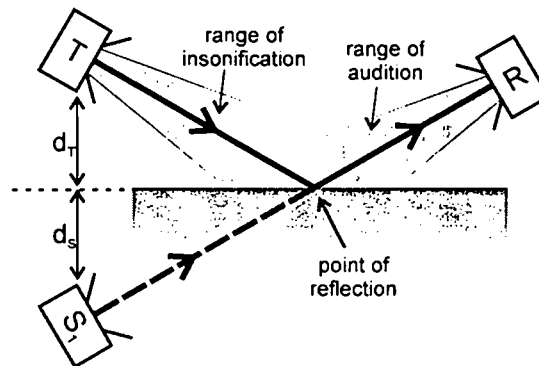
Figure 3.19: Principle of modeling specular reflections with the method of a virtual source

In case of smooth surfaces acting like a mirror to ultrasonic waves, reflections can be modeled using virtual sources which are located behind the reflecting object and which allow to treat reflections as direct transmissions. The position of the virtual source S_I is defined by the mirroring of the initial source T at the reflecting surface, which can be extended (compare dashed line in Figure 3.19). As shown there, the virtual source S_I is in the same distance behind

the reflector as the transmitter is in front ($d_T = d_S$) and a line from the transmitter to the virtual source is perpendicular to the reflecting surface.

The region of insonification is defined as the volume where the transmitter sound impinges on objects and the volume from which a receiver can detect echoes is called the field of audition. The intersection of the direct wave from S_i with the surface is called the Point of Reflection (PoR). To obtain a valid PoR, it must

- be located on the surface of the object,

- lie in the region of insonification of the transmitter and

- also in the range of audition of the receiver.

In case of smooth surfaces the PoR depends on both, the transmitters and the receiver's position.

In case of corners (Figure 3.18/b), where the radius of the edge is much smaller than the wavelength of the ultrasonic signal, diffuse reflections occur which spread the incoming signal in every direction. According to [Mor68] the ratio between the signal magnitudes of the reflections of plane s_{plane} and edge s_{edge} is given by

$$S_{plane} : S_{edge} = 1 : \frac{1}{2\pi\sqrt{\frac{d}{\lambda}}}.$$ (3.45)

It depends on the distance to the edge d and the wavelength of the ultrasonic signal λ.

3.3.3 Definition of detection area

In most works the detection range of ultrasonic distance measurement systems is modeled as cone shaped volume with defined opening angle. However, in case of amplitude detection systems, this assumption does not hold: due to the strongly object dependent amplitudes of echoes, the following deviations from the ideally cone shaped detection area are found:

- Object dependent reflection properties: objects providing a strong echo are detected in a larger area than others with weak reflection properties. This includes the distance of the object to the sensor as well as the angle from the sensor axis, inside which the object is located in front of the sensor.

  In Figure 3.20 the detection areas of an industrial ultrasonic distance sensor based on amplitude detection is shown (sensor type UB2000-30GM-H3-V1 from Pepperl&Fuchs [Pep04]): the datasheet provides two different detection areas for two well defined reflection objects. A rectangular plane of the size 100x100 mm^2 is detected in the area included by the solid line. The dashed line is valid for a round rod with a diameter of 25 mm. As mentioned before the round rod with weak reflection properties is detected in a much smaller area than the well reflecting plane.

- Object dependent signal attenuation: time dependent amplification allows compensation of the air damping, however, this is only valid for special object types. According to equation (3.45) the amplitude of a diffusely reflected signal is additionally weakened

with increasing distance in contrast to specular reflection. For full compensation of the distance dependent attenuation a priori knowledge of the object shape is necessary.

- Measurement errors at the borders of the detection area: towards the border of the detection range the signal amplitudes decrease which leads to systematic measurement errors (see chapter 4.2.1).
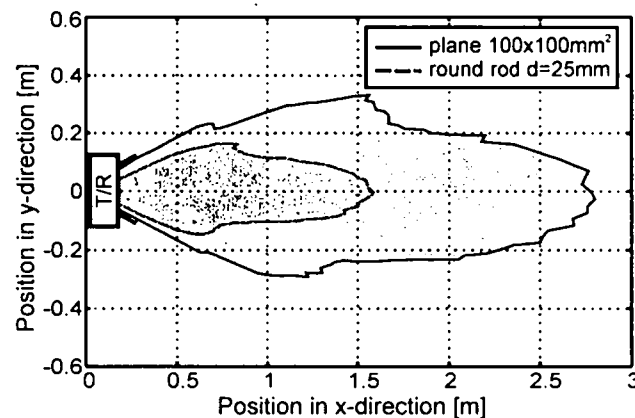
Figure 3.20: Detection areas of ultrasonic distance measurement sensor with amplitude detection for two different object types (*plane 100x100 mm²* and round rod with diameter of *25 mm*)

3.4 Advanced system properties

Advanced system properties are those exceeding the basic measurement requests but are necessary in special applications. The mentioned properties are the coding ability, the echo separation and the use of multi-receiver configurations.

3.4.1 Ability of Coding

Coding of signals means the generation of different signal types which are distinguished by the receiver. The needs for signal coding are discussed and afterwards some embodiments are described and discussed according to their advantages and disadvantages.

3.4.1.1 Need for signal coding

There are several reasons for the need of signal coding in ultrasonic distance measurement systems. In the following some examples are shown where signal coding leads to significant improvements:

a) Parallel systems: in contrast to optical systems that can use well focused signals (e.g. laser beams), ultrasonic systems provide a broad signal beams. Especially in cases where large distances are measured, one transmitter insonificates a rather big area. If there are several systems in the same operating range, they are very likely interfering with each other. Coding of the transmitted signals offers the possibility to use a unique signal for each system to prevent the problem of interference (see Figure 3.21/a).

b) Use of several transmitters: when a system includes several transmitters (e.g. position determination by trilateration in [Ran02]), it is necessary to distinguish which

transmitter is the source of a received signal. The use of differently coded signals for each transmitter allows this determination. Another example is the active reflection method as described in chapter 2.3.

c) Improvement of measurement rate: especially systems based on passive reflection suffer from a relatively low measurement rate due to the comparable low speed of sound in air. To prevent ambiguities of measurement results, a new measurement must not start before the signal of the previous measurement cycle is received or sufficiently damped. This is especially crucial in cases of scanning applications where a lot of measurements are carried out. The use of consecutively differently coded signals allows to start a new measurement cycle before the previous one is finished because the receiver can assign each received signal to the corresponding transmission time and avoid ambiguities in this way.
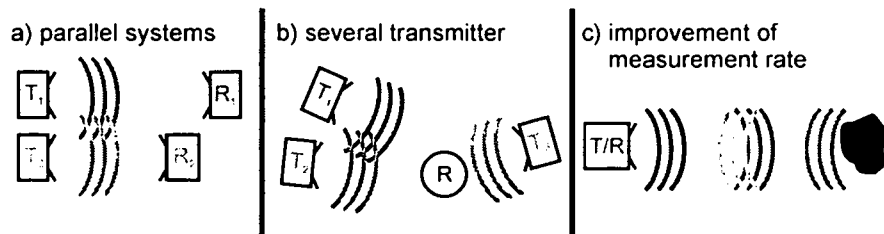
Figure 3.21: Different needs for coding of ultrasonic signals:
a) several systems in parallel, b) several transmitters and
c) improvement of measurement rate

3.4.1.2 Possibilities of signal coding

There are several possibilities to achieve coding of signals. While there are also systems based on A-B-measurement that provide coding with the external signal [War97], we are interested in "ultrasonic only" applications. In the following, three basic types of coding are shown and their properties are discussed.

a) Signal frequency: systems using small bandwidth signals (e.g. mono frequent bursts) can use different signal frequencies for coding purposes. In case of narrowband transducers (e.g. piezo-ceramic types) this is achieved by different distinctive resonance frequencies of different types. However, in this case the frequency cannot be changed without changing the transducer element. In case of wide bandwidth transducers (e.g. electrostatic type) several signal frequencies can be emitted and at the receiver a separate band pass filter is applied.

b) Time separation: another method that is more flexible uses groups of two or more narrowband signals whose time delay between each other contains the coding information. One example is found in [Kle99], who codes the transmitter identity using time separation of double pulses which allows two transmitters to operate simultaneously without spurious crosstalk readings.

c) Wide bandwidth signals: using wide bandwidth signals allows coding of the transmitted signal by applying different signal forms. In literature several attempts as Barker coded burst signals [Sta97], pseudo random noise [Jör97], Dirac like pulses [Kle99] or

frequency modulated bursts (so-called "chirps") [Gil99] [Zim92] are found. The receiver determines the code of the signal with correlation based methods. This method requires on the one hand most resources, but on the other hand it is most flexible, provides high resolution and also good echo-separation capabilities.

In Table 3.8 the presented signal coding methods are compared with regard to critical properties of ultrasonic systems as the complexity of implementation, the robustness to interferences, the echo separation capabilities and the flexibility of coding.

3.4.2 Echo separation

Echo separation describes the capability of ultrasonic systems to separate echoes of objects located at similar distances to the measurement system. It is specified by the minimum distance d_{sep} between two objects that is necessary to detect each object separately. In the following two types of signals processing algorithms are distinguished: at first systems that require separated signals at all and secondly systems that are able to distinguish overlapping signals.

	signal coding by		
	using different signal frequencies	applying different time separations	special wide band signals
complexity of Implementation	low	low	high
robustness to interference	good	bad	good
echo separation	bad	bad	good
flexibility of coding	bad / complex	good	good

Table 3.8: Comparison of different signal coding methods

3.4.2.1 Algorithms not allowing overlapping of signals

Most ultrasonic systems whose detection algorithms are based on evaluation of the signal amplitude (e.g. burst detection) are not able to separate overlapping signals reflected by different objects at nearly the same distance. Therefore, the echo separation capability is bound to the length of the transmitted signal T_{send}. Especially in case of narrowband transducers the effective time $T_{send,eff}$ can be much longer than the length of the electrical excitation of the transmitter. Therefore, $T_{send,eff}$ is the minimum necessary time between two signals that allows the receiver circuit to be able to differentiate the new signal. This leads to an echo separation capability d_{sep} of

$$d_{sep} \geq \frac{c\,T_{send,eff}}{2}. \tag{3.46}$$

3.4.2.2 Algorithms able to separate overlapping signals

Algorithms that are able to separate overlapping signals often evaluate the frequency (e.g. continuous wave methods [Pol98]) or the phase (e.g. correlation based methods [Zim92]) of the

signal. However, from radar engineering a theoretical bound for the range solution d_{sep} of reflection based systems is known [Meh99]:

$$d_{sep} > \frac{c}{2} \frac{\pi}{\omega_0} = \frac{c}{4 B_0} \tag{3.47}$$

In equation (3.47) $\pm B_0$ means the 3dB signal baseband bandwidth in Hertz.

3.4.3 Multi receiver configuration (trilateration)

There are lots of works found presenting ultrasonic distance measurement systems containing two or more receivers ([Bar90], [Kle95], and [Kle99]). These configurations are mainly used for trilateration purposes to determine the position of a reflecting object by evaluating the distances measured by each receiver. While on the one hand impressive results are found, there are also lots of problems these systems have to deal with as shown in the following:

- In case of multiple reflecting objects located in the area of detection, the resulting echoes of each receiver must be assigned correctly to each object, otherwise severe measurement errors may occur. One solution to this problem is to determine possible ambiguities [Kle95] and to ignore the corresponding values, which, however, leads to missing measurement results.

- The position of the PoR depends in most cases on both the transmitter and receiver position. The use of several receivers, therefore, leads to several (different) PoRs which may cause undefined results and measurement uncertainties. However, in [Bar90] this effect is also used to determine different object types.

- The problem of several different PoR increases with the distance between the receivers, but a greater distance enhances the angular resolution at the same time. Therefore, a compromise between the angular resolution and possible measurement uncertainties must be found.

4 State of the art

After the discussion of the basic properties in chapter 3, now the state of the art is presented. At first several transducer technologies are shown and afterwards some basic system concepts are presented.

4.1 Transducer technologies

A lot of research has been done in developing appropriate sensors for different tasks as distance measurement, measurement of chemical or physical variables [Mag94] or non destructive material testing [Sal03]. We concentrate on distance measurement in air and, therefore, on ultrasonic sensors that convert either electrical signals to longitudinal pressure waves running through air (transmitter) or incoming waves to electrical signals (receiver). A good overlook is given in [Man92]. Most ultrasonic transducers can work in both ways, as transmitter and as receiver. Using combined transducer a blind zone in the front of the transceiver must be taken into account because during transmission no receiving is possible and, moreover, it takes some time to switch from transmitting to receiving mode. The blind zone, therefore, depends on the length of the transmitted signal and in case of continuous waves (Continous Transmission Frequency Modulation - CTFM) the use of a transceiver is not possible and separate transmitters and receivers must be used.

In the following some of the basic methods for generating and receiving ultrasound in air are shown.

4.1.1 Piezo-ceramic

Most commercially available sensors, especially dedicated to industrial environments, are based on the piezo-effect occurring in piezo-active materials. This sensor type is characterized by a small form factor, high robustness and a very small usable frequency range due to its very distinctive resonance frequency. An example is shown in [Bab91], where a transducer is built of a piezo-ceramic disc. To use piezo-ceramic transducers in air, special matching layers between the piezo-ceramic element itself and the air are necessary because the acoustic impedance of the active element strongly differs from the acoustic impedance of air. Special matching layers provide an appropriate changeover from one to the other [Alv04]. These matching layers are responsible for the efficiency and sensitivity as shown in [Hal91] and [Khu88]. To simulate the resulting resonance frequencies of the whole transducers consisting of the piezo-ceramic elements, the housing, matching layers, and so on, finite element algorithms [Lan94] are used.

4.1.2 Composite transducers

Composite transducers are based on the combination of several piezo-ceramics with polymer layers between the active elements to get a more damped resonance frequency and, therefore, a wider usable bandwidth is provided which allows using them in pulse compression techniques [Rei98]. One example of a composite transducer implemented with thick film technology is given in [Cic97]. The sensitivity of piezo-composite transducers is examined in [Far97].

4.1.3 Ferroelectric Polymer Technology (PVDF)

A rather new method is the ferroelectric polymer technology that is based on the piezo-effect but provides much wider bandwidths. One form that is used in many works is the PVDF (Polyvinylideneflouride) foil that expands and contracts depending on the applied electric field. While the foil itself provides a very high bandwidth, the resulting resonance frequency depends on the final shape of the foil [Fio92]. This allows controlling the resonance frequency by mechanical foil deformation [Fio98] [Fio99]. Furthermore, works are reported where the foil is used to get a transducer array built of a set of small transducers [Cap97] [Cap94].

4.1.4 Electrostatic

Another main principle is the electrostatic method to generate and detect ultrasonic signals. The sensors mainly consist of a rough (mostly grooved) back plate covered by a thin metallized membrane. Several methods to model and characterize these sensors are found in literature [Ada94] [Ge99]. The most famous transducers used in mobile robotics are the electrostatic transducers from Polaroid (especially series 6000 and 7000 [www1]). Furthermore, there are also several attempts to build transducers with more uniform characteristics and better sensitivity by using e.g. silicon micro machined back plates [Sch92]. One major drawback of electrostatic devices, the necessary DC-bias voltage, is eliminated in [Hut95] by using a polarized metallized membrane. Electrostatic transducers are characterized by a wide usable bandwidth (providing bursts with fast rising amplitudes or other broadband signals) and a good match of the acoustic impedance.

4.1.5 Micromachined

An interesting method to build electrostatic transducers is given by the well known methods of chip design: the major enhancement comes with the well defined reduction of the space between the back plate and the membrane [Hal96]. While some reported works provide very high resonance frequencies of several MHz [Jin98] [Lad95], which is not useful for large distance measurement in air, there are also some transducers found that have resonance frequencies in the range of few hundred kHz [Har01]. Micromachined transducers are an interesting choice to get complex transducer arrays for beam forming due to their small size and the relatively low necessary operating voltages [Khu98] [Suz89].

4.2 Basic signal processing methods

4.2.1 Amplitude detection

The properties of ultrasonic sensors do not only depend on the used transducer type but also on the type of the transmitted signal and the implemented signal processing algorithm. The principle found in most industrial sensors and also in the often implemented ultrasonic ranging kit 650 from Polaroid [www1] is the ToF method using narrowband bursts. This method is characterized by an easily implementable transmitter circuit and a simple threshold detection receiver. A lot of work was done to get better results as implementing time dependent amplification to compensate signal attenuation or to detect further signal characteristics to get more accurate and reliable results [Kuc03] [Boz92]. One main problem is the limited echo-separation capability coming together with the impossibility of separating overlapping bursts occurring due to objects located at similar distances. This problem becomes even worse the longer the transmitted signal is (compare chapter 3.4.2). In [Ste04] a method is presented that minimizes the signal length by applying a control sequence to reduce unwanted signal ringing.

The simple principle of amplitude detection is not only restricted to burst signals, others try to make use of the high bandwidth provided by electrostatic transducers by transmitting wide bandwidth Dirac-like pulses [Yat99] [Kle02]. The advantage of these short pulses is the good echo separation capability. However, due to the limited energy they are suitable for short measurement ranges only.

4.2.2 Correlation based methods

The two main problems of the amplitude detection method, the inability to separate overlapping echoes and the noise sensitivity are mainly solved by correlation based methods. In general correlation methods (also called matched filter) require wideband transmit signals. The position of the signal is found inside the received signal by matching a previously stored reference signal [Kle95]. Even in case of overlapping of the transmitted signals they can mostly be separated [Jör98]. There are several possibilities for transmit signals found in literature: while some use wide-band Dirac like pulses [Kle99], others use frequency modulated bursts ("chirps") [Gil99] [Zim92], modulated digital Barker-Codes [Sta97] or pseudo random noise [Jör97]. While correlation based methods provide on the one hand very good results, on the other hand they require a lot of calculation effort compared to amplitude detection algorithms. There are some attempts found in literature to reduce this high effort: some combine correlation methods with the easy implementable amplitude detection to achieve better accuracy [Hea00], others reduce the sampled incoming signal to one bit and implement a one bit correlation that is well implementable in Field Programmable Gate Arrays (FPGA) [Zim92].

4.2.3 Continuous transmission frequency modulation (CTFM)

While all methods shown use more or less short signals, there are also some attempts to use continuous waves and to gather information out of the sum of the overlapping signals produced by several reflecting objects [Pol98]. The principle is the following: a long linearly frequency modulated signal, which is longer than the expected ToF to the farthest object, is transmitted.

The received signal, containing the sum of all occurring reflections on objects, is multiplied by the actual transmitted signal. After low pass filtering the resulting signal contains only frequencies proportional to the distance to each reflecting object which then can be found by evaluating the Fast Fourier Transform (FFT). While the frequency contains the distance information, the amplitude describes the strength of the echo which is used in some work for object characterization [Pol99].

4.3 Untreated problems of ultrasonic sensors

Although there is a lot of work done in the range of ultrasonic distance measurements, there are some topics that are not really addressed up to now. In the following these open points are summarized.

4.3.1 Well defined range

Most commercial ultrasonic sensors (which are mostly based on burst detection) deliver proper results only in case of well defined objects that are located near the sensor axis. Although the range of detection for different objects is given in datasheets (compare Figure 3.20), at the borders of this range fluctuating results are found which also produce systematic distance measurement errors (see chapter 9.3.1). This inhibits the use of these ultrasonic devices in sophisticated applications that require accurate information about the location of objects. In [Kra03] algorithms are presented that allow the calculation of 3D-orientations of edges out of the touching positions of the ultrasonic system (position of first and last detection of the edge during a scan). As conventional measurement systems provide errors especially in this range of the border, they are hardly to use in this application as a very large amount of measurements is necessary to deal with these fluctuating measurements by means of statistics.

4.3.2 Independence of reflecting properties

Due to the reflection properties of varying objects (especially due to their geometric shape), the detection range of amplitude detection based systems strongly depends on the type and orientation of the reflecting object. Therefore, without a priori knowledge about the object, an estimation of the angle between the sensor axis and the PoR at the object is hardly possible as it strongly depends on the object's reflection properties.

A distance measurement system with well defined measurement conditions provides the following qualities:

- Well defined range of detection (in distance range) independent of the reflecting object properties

- Detection area may not be exactly conically shaped but must provide at least a well defined shape

- The measurement accuracy must not decrease at the border of the detection range

5 Concept of a new measurement system with well defined properties

In the following the main properties of an advanced measurement system are discussed to get a concept of a new measurement system that provides well defined measurement characteristics and, therefore, is useful as general measurement tool in various sophisticated measurement tasks.

5.1 Main characteristics

The main characteristics of a distance measurement system like accuracy, resolution and measurement are discussed in the following.

5.1.1 Accuracy

The following influences to the measurement accuracy are found:

- Speed of sound in air: as ultrasonic distance measurement systems are mostly based on the ToF measurement, the speed of sound in air mainly influences the accuracy of the system. It depends on various physical parameters of the air channel as shown in chapter 3.1, that, especially in case of the temperature, may not be homogenous along the propagation path of the ultrasonic signal (e.g. due to hot objects).

- Moving air (wind): as ultrasonic signals are bound to the transmission medium air, air movement influences the speed over ground of ultrasonic signals. By choosing appropriate measurement topologies this effect can be minimized (see chapter 3.1.7).

- Signal detection: the method of the detection of a received signal also influences the accuracy. For example in simple amplitude detection systems the point of detection depends on the amplitude of the received signal (see chapter 9.3.1). The signal amplitude itself depends on various parameters as the shape of the object (provides specular or diffuse reflection), location of the object with respect to the measurement system and air damping (depends on physical properties). Therefore, an advanced measurement system should use a more robust signal detection method.

5.1.2 Resolution

The resolution mainly depends on the ability of determining the point of time when a signal is received. The resolution also limits the accuracy of the system and, therefore, it should be at

least a factor of ten better than the expected accuracy. Especially multi-receiver configurations make great use of high resolution as they measure the different ToFs to each receiver simultaneously. If the receivers are located near together, disturbances on the air channel are assumed to influence each measured ToF identically and, therefore, are canceled by the difference measurement which is used to calculate the angle of the incoming signal.

5.1.3 Robustness

Particularly in measurement systems for industrial applications robust signal processing methods must be implemented as noisy environments are found in many cases but regardless critical measurement tasks must provide reliable results.

5.1.4 Measurement rate

Especially in case of closed loop real time systems high measurement rates are required which is contradictory to the relatively low speed of sound in air. In most ultrasonic systems the measurement rate is restricted to at least the ToF to the farthest object. The use of differently coded signals in adjacent measurement cycles allows a kind of pipelining by starting a new measurement cycle before the previous one is finished. The signal code helps to avoid ambiguities during signal receiving as each received signal is related to its time of transmission to calculate the proper ToF. Therefore, the implementation of high measurement rates requires coding possibilities provided by the system.

5.1.5 Systems working in parallel

Another critical aspect of coding possibilities is the use of several systems in parallel that must not influence each other. Fields of applications where this is required are the use of several mobile robots working in the same area or industrial systems where multiple collision detection processes are running in parallel.

5.2 Properties of the detection area

Most ultrasonic measurement systems do not care about the detection area occurring due to different reflection properties of objects and require well defined properties for proper operation. However, this inhibits the use of them in sophisticated measurement tasks that are based on high accuracy scanning data. In case of threshold detection of burst signals the measurement accuracy depends on the amplitude of the received signal and the relatively slowly rising edge of the signal envelope leads to systematic measurement errors (compare chapter 9.3.1).

The new advanced measurement system must provide a well defined and object independent detection area that provides invariant accuracy inside the whole measurement range.

5.3 Angle detection

In scanning applications the quality of the achieved results mainly depends on the accuracy of the angles where objects are detected the first and last time (so called "touching positions").

High accuracy requires a well defined detection range of the measurement system and, in case of rotational scans, high angular resolution. If the incremental value $\Delta\Theta$ of the scan process is set to a sufficiently low value to get the required high angular resolution, often an intolerably long measurement time results. Consider the following example: a rotational scan is carried out by a mobile robot in the full range of $\Theta = 360°$. The required resolution of $\Delta\Theta = 0.1°$ and minimum measurement cycle time $T_{meas} = 30\ ms$ (measurement range of about $5\ m$) leads to a minimum scan time of

$$T_{scan,fine} = \frac{\Theta}{\Delta\Theta} \cdot T_{meas} = 108\ s,\qquad(5.1)$$

which is too long in most cases. A method that helps to reduce the scanning time is given by dynamical adaptation of the incremental value $\Delta\Theta$: basically a coarse increment of $\Delta\Theta_{coarse} = 2°$ is chosen but in case of a "touching position" where an object is firstly detected, the increment value is switched to $\Delta\Theta_{fine} = 0.1°$ and an area of $2\ \Delta\Theta_{coarse}$ is scanned again in this range to get a fine resolution of the area of interest. This leads to the following scan time

$$T_{scan,combined} = \left(\frac{\Theta}{\Delta\Theta_{coarse}} + N \cdot 2\frac{\Delta\Theta_{coarse}}{\Delta\Theta_{fine}} \right) \cdot T_{meas} = 5.4\ s + N \cdot 1.2\ s\qquad(5.2)$$

which depends on the number of detected objects N.

An advanced measurement system should be able to measure the angle towards an object at least in a small region near the border of its detection area by signal processing of the received signal. This allows a so called "soft scan" of the region of interest: a fine scan as presented before is not necessary anymore, because after finding the coarse position of the object, the high accuracy value is calculated from the previously sampled data. The scan time is, therefore, fixed to

$$T_{scan,advanced} = \frac{\Theta}{\Delta\Theta_{coarse}} \cdot T_{meas} = 5.4\ s\qquad(5.3)$$

because the fine measurement result is calculated without any additional measurements.

5.4 Multipath propagation

Multipath propagation is a problem that often occurs in case of multiple objects located inside the measurement area. While some regard results due to multipath propagation as errors (e.g. in [Leo92]), others try to get additional information out of it [McK96]. However, this requires very detailed information of the environment where the measurement system is working.

Mostly multipath propagation leads to several reflected signals that are located very near together or are even overlapping. Therefore, an evaluation requires a measurement system that is able to separate even overlapping signals well.

However, signal separation does not solve the main problem of multipath propagation, which is the determination if an echo is caused by direct Line-of-Sight (LoS) measurement or by multipath propagation caused by at least one additional object. A method that would help to

reduce this problem is the following: if it was possible to determine the angle of transmission Θ_{trans} and the receiving angle Θ_{rec} separately, multipath propagation could be recognized in most cases.
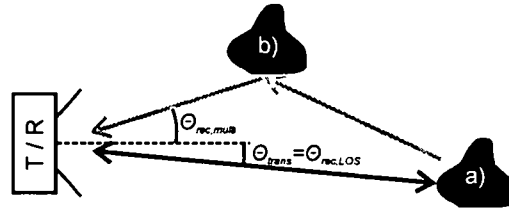
Figure 5.1: Multipath detection by evaluation
of transmit angle Θ_{trans} and receiving angle Θ_{recv}

Compare Figure 5.1: in case of direct line of sight measurement to object a), the angle of transmission is equal to the angle of receiving $\Theta_{trans} = \Theta_{rec,LOS}$. If, however, multipath propagation occurs due to object b), the angle of receiving $\Theta_{rec,multi}$ changes leading to a mismatch in most cases.

Multipath propagation is not in the scope of this work; therefore, it is not further evaluated. However, it provides the basis for this very interesting feature which can be evaluated in future work.

5.5 Summary

A signal processing technique that is able to fulfill the requests shown in the previous chapters is the pulse compression method. However, this method requires a wealth of resources especially in case of input signals with a large dynamic range as it is true for ultrasonic systems. Therefore, the one bit correlation method is introduced that shows similar results and provides several additional properties and is moreover much easier to implement especially in case of real time systems. Nevertheless, high bandwith signals are required which leads to strong demands on the used ultrasonic transducers. It provides the following properties:

- High resolution and accuracy: the pulse compression method delivers high resolution and accuracy independent of the amplitude of the incoming signal which is a major aspect especially in cases where strongly varying signal amplitudes (e.g. due to different object shapes) are expected (see chapter 6.3.1).

- Robustness: as pulse compression carries out a kind of energy compression of a relatively long signal to a very short range of time, it is very robust towards disturbances of the received signal (see chapter 6.3.3). While in case of amplitude detection methods it is more likely to get additional wrong measurement results (occur whenever disturbances exceed the threshold), in pulse compression systems wrong measurements are very rare. In case of strong disturbances signals only may be not detected at all instead of leading to wrong results.

- Signal coding: the use of different pairs of transmitter- and receiver filters (see chapter 6.3.4) allows advanced measurement tasks requiring coding as pipelining to get higher

measurement rates or using several systems in the same operating range in parallel without disturbing each other.

- Echo separation: the high echo separation capability that also allows separation of overlapping signals can be used to distinguish echoes from objects located near together or to evaluate multipath propagation effects.

- Well defined and adjustable detection area: the combination of transducers with different radiation patterns and a signal processing method based on the one bit correlation delivers a very well defined and both amplitude and object independent measurement range (see chapter 8.1). Further signal evaluation allows adjusting the detection area, which enables a kind of angle measurement in a range of several degrees at the border of the detection area (see chapter 7), which may significantly enhance scanning tasks.

- Multipath detection: in contrast to multi receiver applications that evaluate the receiving angle of an incoming ultrasonic wave, the presented method allows evaluation of the angle of transmission. A combination of these two methods may be used to detect multipath propagation.

In the following chapter the pulse compression method is presented and the one bit correlation method is introduced.

6 One bit correlation

The one bit correlation method is a promising approach to solve the open problems mentioned in the previous chapter. A detailed presentation of the method is found in [Zim92], where the 1-Bit-Correlation was firstly introduced to an ultrasonic system. In the following its principle and the achievable advantages are presented.

6.1 Principle of pulse compression by analog filtering

The main principle of pulse compression is the following: a short pulse, as necessary for high resolution and echo separation, runs through a filter whose impulse response $p(t)$ provides the signal to transmit (see Figure 6.1).
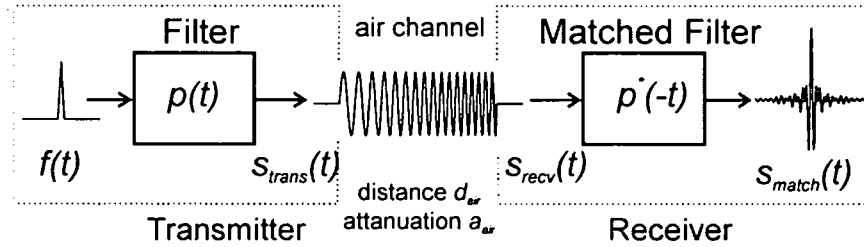
Figure 6.1: Principle of pulse compression

The generated signal $s_{trans}(t)$ is calculated to

$$s_{trans}(t) = f(t) * p(t) = \int f(\tau)\, p(t-\tau)d\tau = \mathcal{F}_{(\omega)}^{-1}\left[F(\omega)\, P(\omega)\right], \qquad (6.1)$$

where the latter part shows the frequency space containing the Fourier transforms of the initial pulse $F(\omega)$ and the impulse response $P(\omega)$. Assuming the initial impulse as Dirac impulse $f(t) = \delta(t)$, the transmitted signal $s_{trans}(t)$ is found to be identical to the impulse response of the filter:

$$s_{trans}(t) = \int \delta(t)\, p(t-\tau)d\tau = p(t) \qquad (6.2)$$

The signal $s_{trans}(t)$ is transmitted by the ultrasonic transmitter, runs through the air channel where it becomes attenuated by the factor a_{air} and delayed by the time $t_d = d_{air}/c$ according the distance d_{air} and the speed of sound c. The receiver, therefore, detects the signal $s_{recv}(t)$ which is

$$S_{recv}(t) = a_{air}\, S_{trans}\left(t - \frac{x_n}{c}\right) = \mathcal{F}_{(\omega)}^{-1}\left[a_{air}\, P(\omega)\, \underbrace{e^{-j\omega \frac{d_{air}}{c}}}_{\text{delay } d_{air}}\right]. \tag{6.3}$$

This received signal $S_{recv}(t)$ then runs through the matched filter $p^{*}(-t)$. The final result $S_{match}(t)$ is found to be

$$S_{match}(t) = \mathcal{F}_{(\omega)}^{-1}\left[S_{recv}(\omega)\, P^{*}(\omega)\right] =$$

$$= \mathcal{F}_{(\omega)}^{-1}\left[a_{air}\, \underbrace{P(\omega)\, P^{*}(\omega)}_{|P(\omega)|^2 = \mathcal{F}_{(\omega)}[psf_t(t)]}\, e^{-j\omega \frac{d_{air}}{c}}\right] = a_{air}\, psf_t\left(t - \frac{d_{air}}{c}\right). \tag{6.4}$$

The final result $S_{match}(t)$ depends on the point spread function $psf_t(t)$ which is, in case of a real valued signal $p(t)$ and only white Gaussian noise, the autocorrelation of the impulse response of the used filter. In case of colored noise, the power density spectrum of the noise must be taken into account. For good results the following requirements must be met by the envelope of the matched filter output $S_{match}(t)$:

- steep slopes for high resolution

- short pulse length for good echo separation capabilities

- well defined and clear pulse to avoid ambiguities

The impulse response $p(t)$ and the transmitted signal $s_{trans}(t)$ are chosen in order to fulfill the mentioned requests. While there are many possibilities of transmitted signals, in many cases frequency modulated chirps are used. In [Rei98] chirps with quadratic and cosine shaped frequency characteristics are examined. Due to their larger bandwidths good measurement results are reported. However, because to its simplicity in this work the impulse response $p(t)$ is chosen as linear chirp. This is mainly defined by its center frequency f_0 and the bandwidth B which leads to the begin- respectively end-frequency of

$$f_{begin/end} = f_0 \pm \frac{B}{2}. \tag{6.5}$$

The relative bandwidth B_{rel} is defined to

$$B_{rel} = \frac{B}{f_0}. \tag{6.6}$$

A linear chirp $f_{chirp}(t)$ is defined by equation (6.7). The function $rect(x)$ is defined to $rect(x) = 1$ in the range $-\frac{1}{2} < x < \frac{1}{2}$ and $rect(x) = 0$ anywhere else. The time T is the length of the chirp.

$$f_{chirp}(t) = rect\left(\frac{t}{T}\right)\cos\left[2\pi\, t\left(f_0 + \frac{B}{2}\frac{t}{T}\right)\right] = rect\left(\frac{t}{T}\right)\mathrm{Re}\left[e^{2\pi j\, t\left(f_0 + \frac{B}{2T}t\right)}\right] \tag{6.7}$$

In the following picture a chirp with the following parameters is plotted: chirp length $T = 300\ \mu s$, center frequency $f_0 = 55\ kHz$, bandwidth $B = 30\ kHz$. This leads to a relative bandwidth $B_{rel} = 55\ \%$ and the begin- and end frequency $f_{begin} = 40\ kHz$ and $f_{end} = 70\ kHz$.

According to [Sou99] the corresponding point spread function $psf_l(t)$ of a linear chirp defined by equation (6.7) is shown in equation (6.9). This equation is valid for long signals, where the bandwidth B is mainly defined by the begin and end frequency. However, in the interesting region around the correlation maximum, it provides a good approximation in case of short signals, too. The point spread function $psf_l(t)$ contains an oscillation with center frequency f_0 that is modulated by the $sinc(x)$ function according to

$$\mathrm{sinc}\left(x\right) = \frac{\sin\left(\pi\ x\right)}{\pi\ x} \tag{6.8}$$

that depends on the actual bandwidth B:

$$psf_l\left(t\right) = \underbrace{e^{2\pi j\ f_0\ t}}_{oscillation}\ \underbrace{\mathrm{sinc}\left(B\ t\right)}_{envelope} \tag{6.9}$$
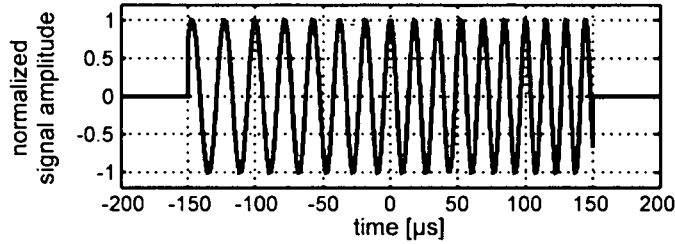
Figure 6.2: Linear Chirp with $L = 300\mu s$, $f_0 = 55kHz$ and $B = 30kHz$

In Figure 6.3 the point spread function $psf_l(t)$ of the linear chirp is plotted together with the envelope of the point spread function and a linear approximation that helps to qualify the point spread function only by knowing the relative bandwidth B_{rel}.

A linear approximation of the envelope (as defined by a direct connection from maximum $\kappa_{max} = 1$ to first zero of the envelope) $psf_{lin}(t)$ is given by

$$psf_{lin}\left(t\right) = \kappa_{max}\left(1 - B\ t\right). \tag{6.10}$$

Further calculation leads to an approximation of the amplitude of the highest maxima in vicinity $\kappa_{max,vicinity}$ (see Figure 6.3):

$$\kappa_{max,vicinity} \approx \kappa_{max}\left(1 - \frac{B}{f_0}\right) = 1 - B_{rel} \tag{6.11}$$

With increasing relative bandwidth B_{rel} the amplitudes of the maxima in vicinity $\kappa_{max,vicinity}$ decrease, which leads to better detectable correlation results.
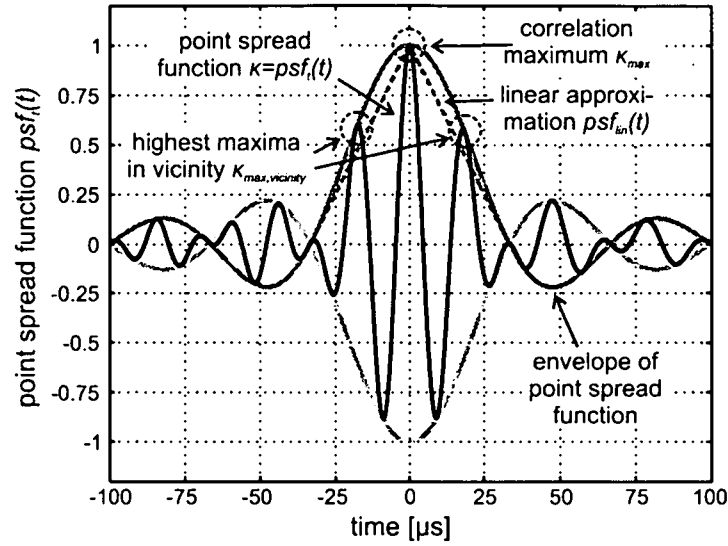
Figure 6.3: Correlation result of linear chirp shown in Figure 6.2
with envelope of point spread function and linear approximation

Pulse compression provides high resolution and good echo separation capabilities. However, as pulse compression is a linear method the signal amplitude, its results depend on the reflection properties of the objects. In Figure 6.4 the matched filter result $s_{match}(t)$ of a received signal $s_{recv}(t)$, consisting of two echoes with different amplitudes ($A_1 = 1$ and $A_2 = 0.5$) and a time delay of $t_{delay} = 400 \, \mu s$, is shown. Due to the wide possible amplitude range of ultrasonic signals (air attenuation, reflection properties) also the range of the matched filter results are strongly varying, which makes signal detection more difficult.
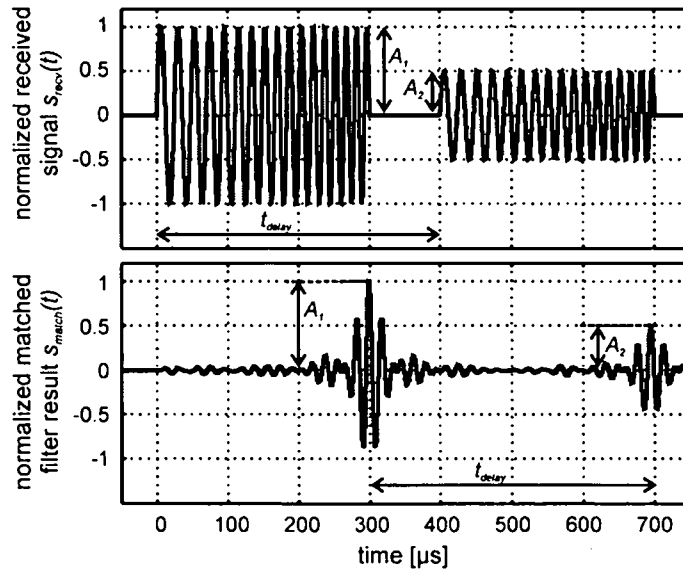
Figure 6.4: Combination of two differently attenuated signals ($A_1 = 1$ and $A_2 = 0.5$) and its influence on pulse compression

In the following a pulse compression method based on 1-Bit-correlation is presented which provides correlation results independent of the signal amplitude of the received signal.

6.2 Implementation of the One Bit Correlation

The One Bit Correlation method digitizes the incoming signal with one bit in resolution, therefore, only the sign of the signal, but not the amplitude is evaluated. One possible implementation suitable for FPGAs is shown in Figure 6.5: it consists of a shift register of the length N, which is defined by the sampling frequency f_{sample} and the length T of the impulse response of the filter $p(t)$ to $N = T f_{sample}$. The digitized received signal is applied to the shift register as bit stream which is shifted further at each point of sampling according to the sampling frequency f_{sample}. Further information about this work is found in [Elm00].
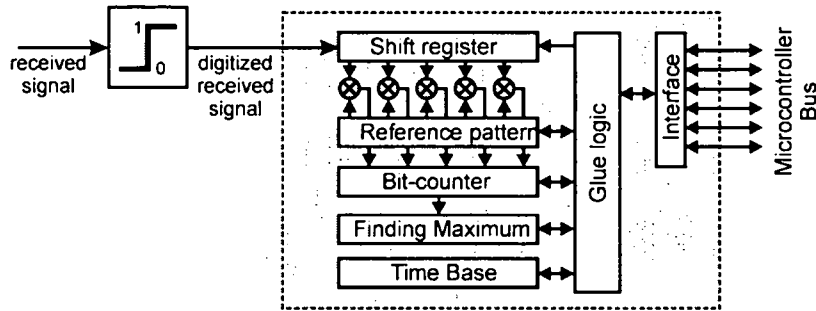
Figure 6.5: Implementation of 1-Bit-Correlation in
Field Programmable Gate Array (FPGA)

The content of the shift register is compared bitwise with a previously stored reference pattern, which corresponds to the impulse response of the matched filter $p^*(-t)$. The sum of all coincident bits is the correlation result $k(t_x)$ at this point of time t_x. In case of full coincidence the absolute correlation result k is equal to the number of bits N. A value that is independent of the actual length of the reference pattern is the relative correlation result κ, which is related to the maximum achievable result of $k_{max} = N$, and is defined by

$$\kappa = \frac{k - \dfrac{k_{max}}{2}}{\dfrac{k_{max}}{2}} = \frac{2\,k - k_{max}}{k_{max}} = \frac{2\,k - N}{N}.$$

(6.12)

Full coincidence, therefore, leads to $\kappa = 100\,\%$. Assuming an uncorrelated input signal a result around $k = N/2$ corresponding to $\kappa = 0\,\%$ is expected and in case of perfect matching but negative sign full anti correlation of $k=0$ and $\kappa = -100\,\%$ is found, respectively. As shown in [Zim92] the one bit correlation provides very similar results as the analog correlation method; a comparison of the results of the analog and of the 1-bit correlation is provided in Figure 6.6.

The 1-bit correlation provides the following advantages:

- independence of signal amplitudes
- real time evaluation possible due to
- good implementation in FPGAs
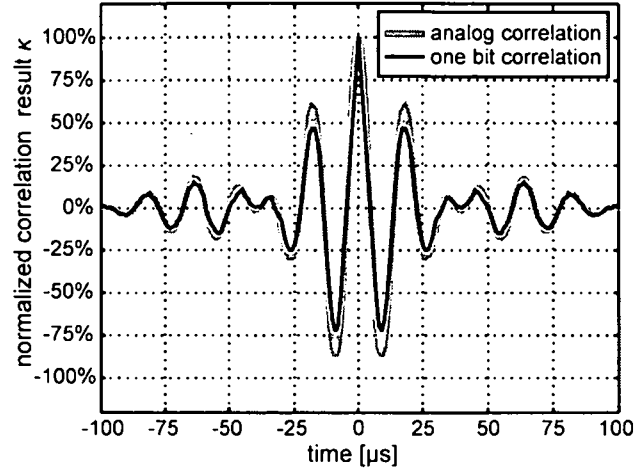
Figure 6.6: Comparison of the results of analog and 1-bit correlation

6.3 Advantages of the One Bit Correlation

In the following the advances of correlation based methods are discussed.

6.3.1 High resolution

Resolution depends on the detection of the transmitted signal $s_{trans}(t)$ in the received signal $s_{recv}(t)$ to determine the delay $t_{air} = d_{air}/c$. In case of pulse compression the position of the correlation maximum indicates the position of the transmitted signal. This allows to introduce a threshold κ_{thres} which examines the matched filter output $s_{match}(t)$ (see Figure 6.7). After exceeding of the threshold κ_{thres} the relative maximum $\kappa_{max,1}$ is looked for and a seek timer $t_{seek,1}$ is started. The length of the seek time t_{seek} depends on the center frequency of the used chirp f_0 and is set to

$$t_{seek} \approx 1.5 \frac{1}{f_0}. \tag{6.13}$$

If a further sampling point $\kappa_{max,n+1}$ exceeds the previous one $\kappa_{max,n}$ during the seek time $t_{seek,n}$, the new reference value becomes $\kappa_{max,n+1}$ and a new seeking process starts. When the timer $t_{seek,m}$ expires, the corresponding maximum $\kappa_{max,m}$ is set to be the maximum found.

In the example shown in Figure 6.7 the detection threshold is exceeded the first time at $t = -19\ \mu s$. After finding the first maximum $\kappa_{max,1}$ the seek time $t_{seek,1}$ is started. At $t = -2\ \mu s$ the previous maximum is exceeded and the following maximum $\kappa_{max,2}$ is obtained. This value remains the maximum during the seek time t_2 and is, therefore, regarded as main maximum. The resolution is defined by the sampling rate: in case of $f_{sample} = 1\ MHz$ a distance resolution of $d_{res} = 0.17\ mm$ (in case of reflection based systems) is obtained. To achieve higher resolution the following steps are possible:

- Increasing of sampling rate f_{sample} (also increases calculation effort)

- Partial increasing of sampling rate (finding of range where maximum is located with low sampling rate $f_{sample,low}$, afterwards accurate location determination with high

sampling rate $f_{sample,high}$ – similar calculation effort during seeking, only higher effort during accurate localization)

- Implementation of curve fitting algorithms to the correlation results (similar calculation effort during seeking, only higher effort during accurate localization)
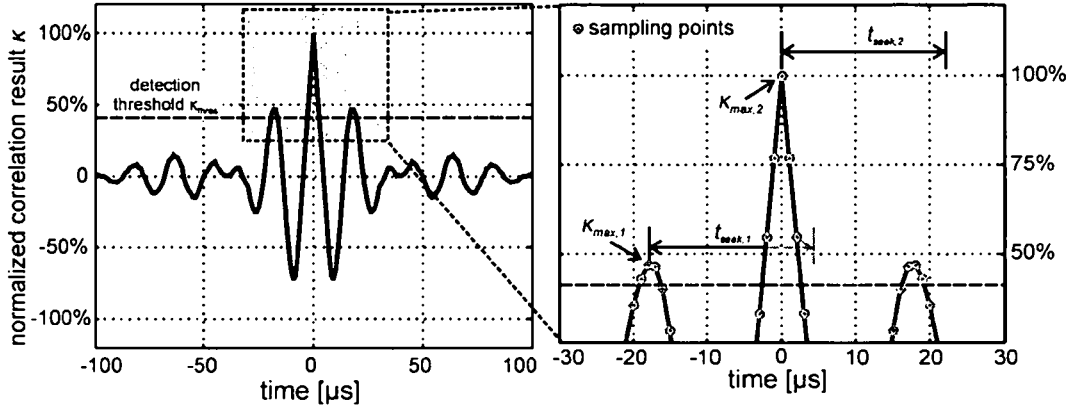
Figure 6.7: Correlation result with sampling points and maximum finding algorithm

6.3.1.1 Estimation of lower bound of sampling frequency

In the following a lower bound of the required sampling frequency, necessary for the 1-bit correlation method, is estimated. It is based on the linear approximation of the envelope of the correlation results $psf_{lin}(t)$ shown in Figure 6.3. The main request to the sampling frequency is the ability to find the absolute correlation result κ_{max}. This can be achieved only when at least two sampling points are located inside the range, where the correlation result around the absolute maximum exceeds the amplitudes of the maxima in vicinity $\kappa_{max,vicinity}$. This range from $-t_{vicinity} < t < t_{vicinity}$ is marked grey in Figure 6.8. Therefore, the minimum sampling frequency $f_{sample,min}$ is defined to

$$f_{sample,\min} = \frac{1}{\Delta t_{\max}} = \frac{1}{2\,t_{vicinity}}\,. \tag{6.14}$$

The slope on each side of the correlation result is linearly approximated by

$$\kappa_{lin}(t) = 1 - \frac{t}{t_0} = 1 - \overbrace{4\,f_0}^{\frac{1}{t_0}}\,t\,. \tag{6.15}$$

According to equation (6.11) the relative amplitude $\kappa_{max,vicinity}$ of maximum in vicinity is approximated to

$$\kappa_{\max,vicinity} \approx 1 - B_{rel}\,. \tag{6.16}$$

The border of the range $\pm t_{vicinity}$ inside which at least two sampling points must be located is calculated by the equations (6.15) and (6.16) to

$$t_{vicinity} = \frac{B_{rel}}{4 f_0} .$$ (6.17)

Therefore, the width of the range Δt_{max} and hence the minimum sampling frequency $f_{sample,min}$ becomes

$$f_{sample,min} = \frac{1}{\Delta t_{max}} = \frac{1}{2 t_{vicinity}} = 2\frac{f_0}{B_{rel}} .$$ (6.18)
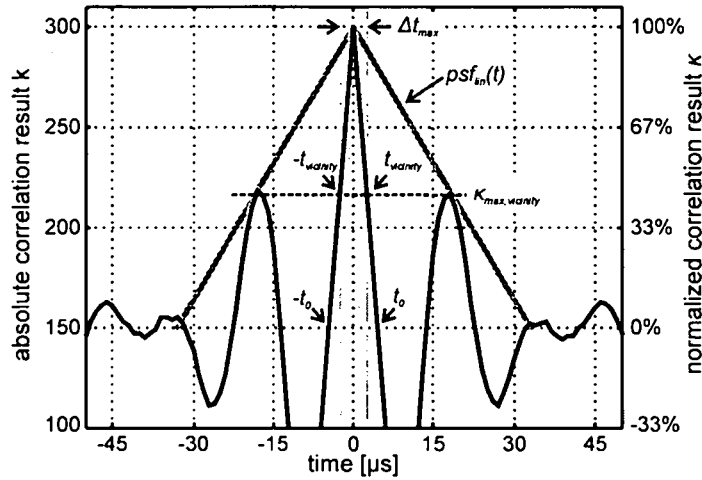
Figure 6.8: Correlation result with parameters
to obtain the minimum sampling frequency $f_{sample,min}$

According to the Nyquist theorem the sampling frequency $f_{nyquist}$ must not be lower than the double of the highest frequency f_{max} of the sampled signal:

$$f_{nyquist} > 2 f_{max}$$ (6.19)

In case of a linear chirp with increasing frequency the end frequency f_{end} can be considered as lower bound of the maximum signal frequency f_{max}. According to equation (6.5) this bound is calculated to

$$f_{nyquist} > 2 f_{max} > 2 f_{end} = 2\left(f_0 + \frac{B}{2} \right) = 2 f_0 \left(1 + \frac{B_{rel}}{2} \right) .$$ (6.20)

While the Nyquist frequency $f_{nyquist}$ increases with relative bandwidth B_{rel}, the calculated minimum sampling frequency $f_{sample,min}$ decreases. This allows calculating a critical relative bandwidth $B_{rel,critical}$ at which the minimum sampling frequency $f_{sample,min}$ is not valid any more as it violates the Nyquist theorem. This critical bandwidth is found in case of equality of the Nyquist frequency $f_{nyquist}$ and the minimum sampling frequency $f_{sample,min}$ and can be calculated to

$$B_{rel,critical} = -1 + \sqrt{3} \approx 73\% .$$ (6.21)

In Figure 6.9 the minimum necessary sampling frequencies for two center frequencies $f_0 = 50\ kHz$ and $f_0 = 80\ kHz$ are plotted together with their corresponding sampling frequencies $f_{sample,min}$ and $f_{nyquist}$. As shown in equation (6.21) these two are intersecting at a relative

bandwidth of $B_{rel} = 73\ \%$. Below this value the sampling frequency must be higher than the minimal sampling frequency derived in equation (6.18), therefore, $f_{sample} > f_{sample,min}$. Above this border the Nyquist frequency $f_{nyquist}$ is the crucial border and in this case $f_{sample} > f_{nyquist}$ must be achieved.
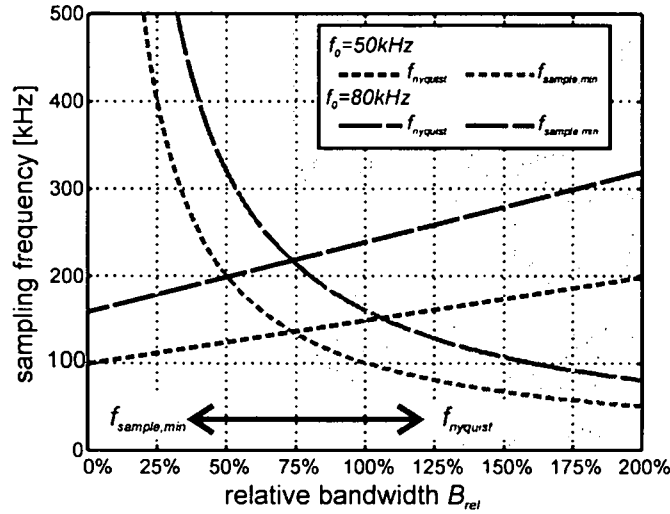
Figure 6.9: Minimum sampling frequency depending on relative bandwidth

6.3.2 Echo separation

Echo separation is the ability to detach echoes with low separation distance or also overlapping ones. In Figure 6.10 an example of two overlapping chirps that are separated by using the one bit correlation method is found.
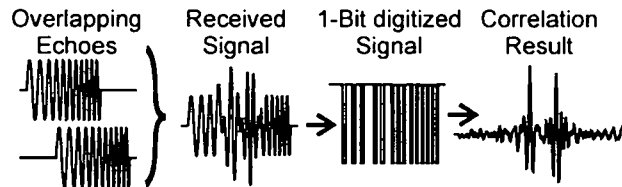
Figure 6.10: Echo separation capability of 1-Bit-Correlation

6.3.2.1 Theoretical evaluation

The echo separation capability mainly depends on the envelope of the correlation result. According to chapter 6.1 the envelope is defined by the point spread function $psf_l(t)$. In case of a linear chirp it is defined by equation (6.9) and the envelope is given by

$$S_{envelope}\left(t\right) = \mathrm{sinc}\left(B\,t\right) \tag{6.22}$$

In Figure 6.11 an evaluation of the equation (6.22) is shown.

Signal separation requires two maxima with a well detectable reduction of the signal envelope in between. In case of two signals with equal amplitudes a reduction of the resulting envelope of about -3 dB is sufficient. This demand requires an attenuation of about -9 dB for each signal, which leads to

$$-9dB \triangleq \frac{1}{2\sqrt{2}} = \text{sinc}\left(B \, \Delta t_{min}\right).$$

(6.23)

Solving equation (6.23) leads to the following approximation

$$\Delta t_{min} \approx \frac{\sqrt{2}}{B},$$

(6.24)

which is the minimum possible time lag between two consecutive signals. In case of a passive reflection system the minimum distance is found to be

$$\Delta x_{min} = \frac{\Delta t \, c}{2} = \frac{c}{\sqrt{2} \, B}.$$

(6.25)
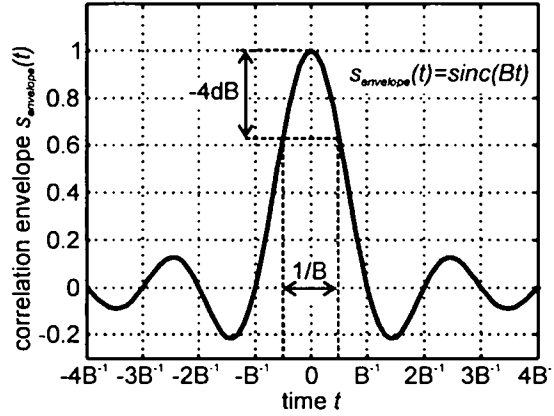
Figure 6.11: Envelope of correlation result
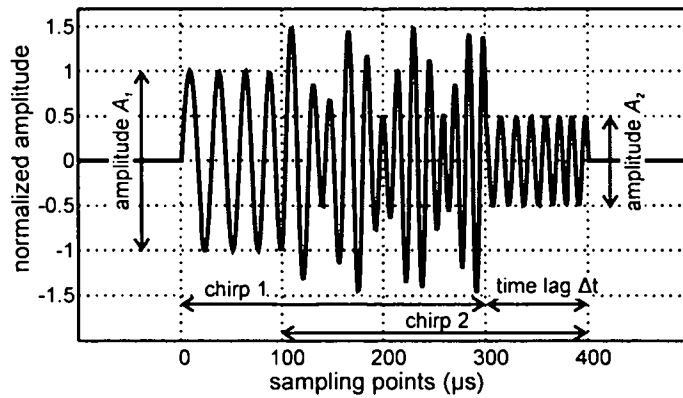
Figure 6.12: Overlapping of two linear chirps ($L = 300 \, \mu s$, $f_0 = 55 \, kHz$, $B = 50 \, kHz$) with relative amplitude $A_{rel} = 2$ and time lag $\Delta t = 100 \, \mu s$

6.3.2.2 Simulation overlapping in case of One Bit Correlation

In the following chirps with a length of $L = 300 \, \mu s$, a center frequency of $f_0 = 55 \, kHz$ and a bandwidth of $B = 50 \, kHz$ are examined. In the example shown in Figure 6.12 the received signal $s_{recv}(t)$ consists of two overlapping chirps. In the following, overlapping chirps are defined by their time lag Δt and their relative amplitude $A_{rel} = A_1/A_2$.

The output of the matched filter $p^*(-t)$ is plotted in Figure 6.13: although the received signals are mainly overlapping, the correlation result provides clear peaks at the positions of the end of each chirp (κ_{max1} at $t_1 = 300\ \mu s$ and κ_{max2} at $t_2 = 400\ \mu s$ – see zoomed area in Figure 6.13). The possibility of signal detection depends on the amplitudes of the maxima as well as on the biggest maximum in vicinity $\kappa_{vicinity}$. The smaller $\kappa_{vicinity}$ is in contrast to the main maxima, the better the detection algorithm works.
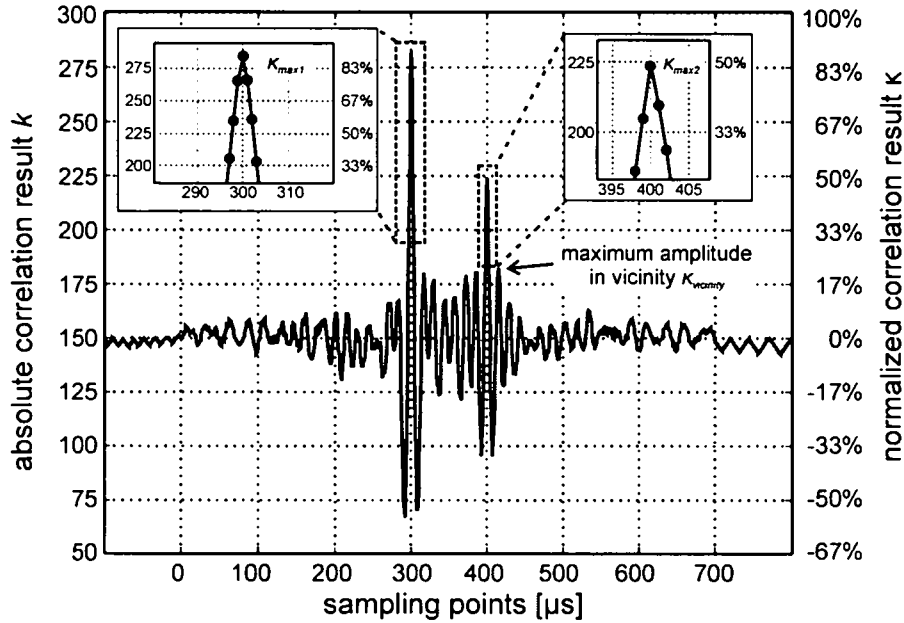
Figure 6.13: Correlation result of overlapping signals shown in Figure 7.1

In the following, overlapping signals are discussed with respect to the points below:

- Ratio between the main maxima (κ_{max1} and κ_{max2}) and the biggest amplitude in vicinity $\kappa_{vicinity}$

- Dependency of the main maxima on the amplitudes of the chirps A_1 and A_2

- Agreement of the positions of the two main maxima with the positions of the overlapping signals

The example provided in Figure 6.12 and Figure 6.13, respectively, leads to the following results: the two main maxima κ_{max1} and κ_{max2} are located exactly at each chirp's end position. At $t_1 = 300\ \mu s$ a correlation maximum of $\kappa_{max1} = 88\ \%$ and at $t_2 = 400\ \mu s$ one of $\kappa_{max2} = 49\ \%$ are found. The biggest maximum in vicinity is located at $t_{vicinity} = 418\ \mu s$ with an amplitude of $\kappa_{vicinity} = 21\ \%$ which is about the half of κ_{max2}. In this case the overlapping signals are well separable.

In the following pictures, a systematic evaluation of overlapping chirps is given. Therefore, the amplitudes of the three greatest relative maxima of the correlation results are plotted over the time lag Δt between the two signals, which allows to qualify the expected results.

At first two signals with a center frequency $f_0 = 55\ kHz$ and a bandwidth of $B = 50\ kHz$ and equal amplitudes $A_{rel} = 1$ are evaluated: outside the range of overlapping ($\Delta t > 300\ \mu s$) an undisturbed correlation result of $\kappa = 100\ \%$ is expected. With decreasing time lag Δt overlapping starts resulting in decreasing correlation results.

Figure 6.14: Maxima of correlation results depending on the time lag Δt
between two overlapping signals

Good separation is possible until about $\Delta t > 20\ \mu s$ while at lower time lags the two main correlation maxima start decreasing and the maximum in vicinity $\kappa_{vicinity}$ increases. In Figure 6.15 the correlation results occurring at a time lag of $\Delta t = 10\ \mu s$ are shown. Here the three main maxima are of about the same amplitude which inhibits a proper allocation to the received signals.
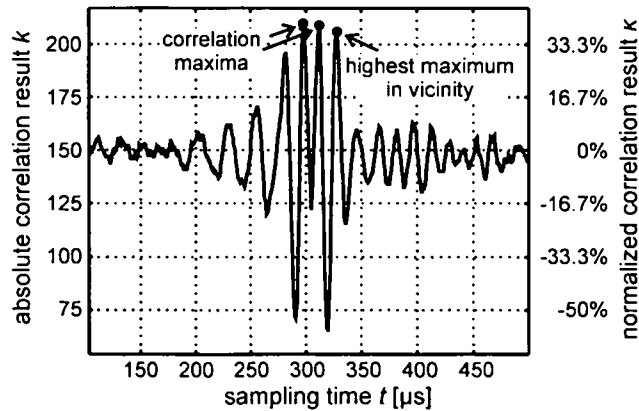
Figure 6.15: Correlation result at time lag of $\Delta t = 10\ \mu s$

To verify the signal separation capability in the described way, the distance errors which occur in case of evaluation of the correlation results are plotted in Figure 6.16: although the signals are overlapping, the correlation maxima κ_{max1} and κ_{max2} are mainly located at the correct position (which means at the end of the overlapping bursts). Strong deviations are found in the range below $\Delta t < 12\ \mu s$, however, in this case the two main amplitudes also strongly decrease

(compare Figure 6.14). At very low time lags $\Delta t < 5 \mu s$ the two signals are melting, in this it is reasonable to refer to the three maxima as one main maximum κ_{max} and two maxima in vicinity $\kappa_{vicinity\ 1/2}$. This condition is visible as well in Figure 6.14 as in Figure 6.16: the resulting maximum κ_{max} provides a very good correlation result of $\kappa_{max} \approx 100\%$ together with low position errors in case of the first correlation maximum, while the other is displaced by about $1/f_0 \approx 18 \mu s$ (distance to next maximum in vicinity).
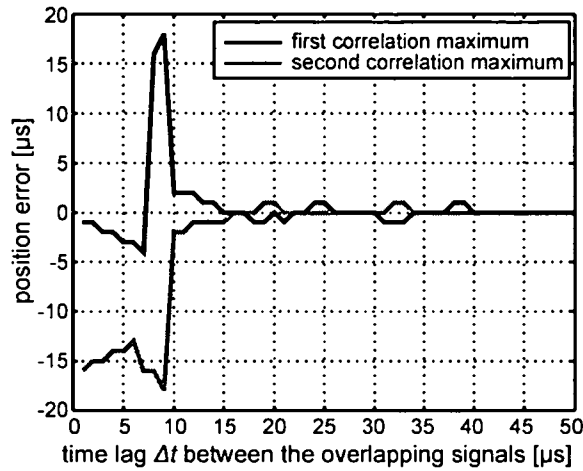
Figure 6.16: Position errors occurring due to overlapping depending on the time lag Δt

A comparison with the theoretically derived value from equation (6.24) of

$$\Delta t_{min} = \frac{\sqrt{2}}{B} = \frac{\sqrt{2}}{50kHz} = 28.3\ \mu s \qquad (6.26)$$

leads to similar results.

6.3.2.3 Comparison between analog and one bit correlation

Based on the simulation shown in the previous chapter, one bit correlation is compared with analog correlation. Therefore, two signals with the same relative bandwidth B and center frequency f_0 but strongly different signal amplitudes ($A_{rel} = 10$) are examined.

In Figure 6.17 the correlation results obtained by analog correlation are shown: as correlation is a linear process, the signal amplitude is also reflected in the correlation results. Although the signals are not overlapping in the example shown, strongly varying correlation results are obtained which inhibits introducing a threshold to evaluate the received signals: the maxima in the vicinity of the first (bigger) signal are already higher than the maximum of the second one. Therefore, an evaluation as shown in Figure 6.14 does not make sense, because the second and third maxima are both maxima in the vicinity of the main maximum and never represent the position of the second signal.

In contrast to the analog correlation, the one bit correlation does not evaluate the amplitude. Therefore, the small second signal is evaluated as well as the big first signal as long as the noise is low. In Figure 6.18 the same incoming signal is evaluated using the 1-bit correlation method. As shown there, both signals are detected in the same way.
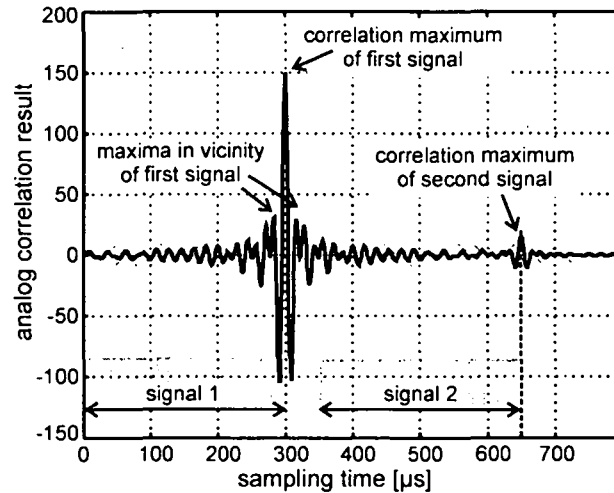
Figure 6.17: Analog correlation result of two signals
with different amplitudes (A_{rel} = 10)

Of course in case of overlapping the bigger signal dominates the correlation results. In Figure 6.19 the correlation maxima are plotted over the time lag between the two signals. As mentioned before, a perfect correlation result is expected in case of no overlapping. Then the correlation result of the smaller signal starts decreasing, however, it is well separable until a time lag of about $\Delta t > 150 \mu s$, where a normalized correlation result of $\kappa \approx 50\%$ is found.
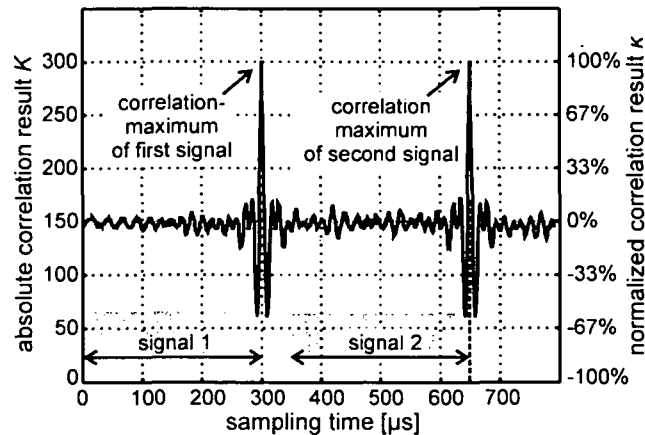
Figure 6.18: 1-bit correlation result of two signals
with different amplitudes (A_{rel} = 10)

The reason is the following: although the bigger signal cancels the overlapping part of the small signal (in case of $\Delta t = 150 \mu s$ that's 50 % of the whole signal), the other half provides a good correlation result, which leads to a normalized correlation result of $\kappa \approx 50\%$ in this case.

6.3.3 Robustness

Robustness means the ability to suppress uncorrelated interfering signals. In the following, short disturbances ($T_{disturbance} < T_{signal}$) and continuous disturbances that are modeled as white Gaussian noise are distinguished.

6.3.3.1 Statistical evaluation of the one bit correlation

Assuming only white Gaussian noise as received signal (see Figure 6.5), the probability p of each bit of the digitized received signal to match respectively to mismatch (q) with the corresponding bit of the reference pattern is
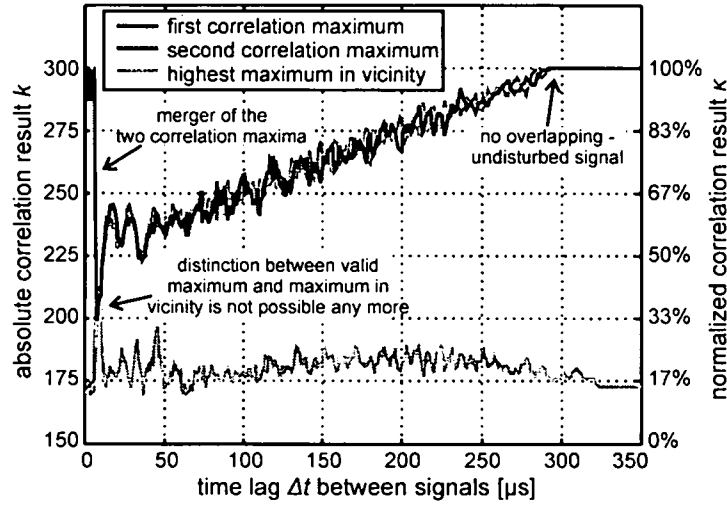
$$p = 1 - q = \frac{1}{2}.$$

(6.27)
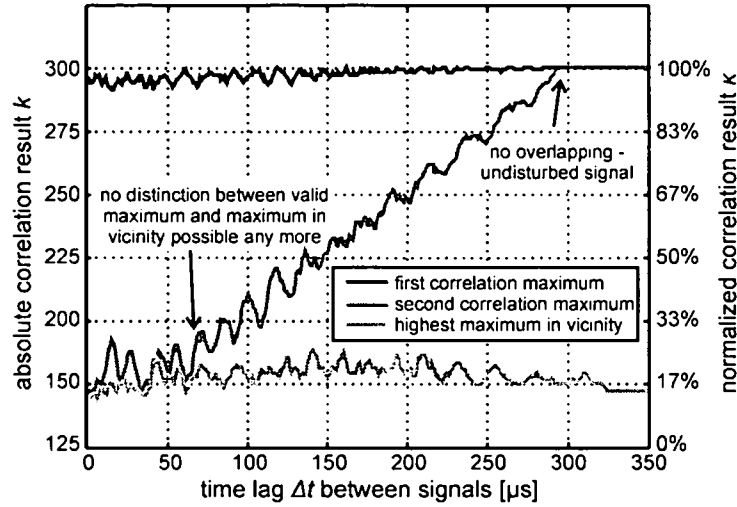
Figure 6.19: Maxima of correlation results depending on the time lag Δt
between two overlapping signals with strongly different amplitudes ($A_{rel} = 10$)

The number of matching bits k represents the absolute correlation result used in this work. In case of a correlation length of N the probability to achieve a full match of $k = N$ respectively $\kappa = 100\,\%$ is equal to

$$p_{100\%} = p^N = \left(\frac{1}{2}\right)^N.$$

(6.28)

The count c_k of possible combinations that reach an arbitrary amount of matching bits k is calculated by the binominal coefficient

$$c_k = \binom{N}{k} = \frac{N!}{k!(N-k)!}.$$

(6.29)

The probability p_k to reach a specific c_k amount of matching bits is given by

$$p_k = c_k\, p^k\, q^{N-k} = \underbrace{\frac{N!}{k!(N-k)!}\, p^k\, q^{N-k}}_{\text{general binomial probability function}} = \frac{N!}{k!(N-k)!}\left(\frac{1}{2}\right)^N.$$

(6.30)

In Figure 6.20 an example of a binomial distribution is plotted in case of a correlation length of $N = 10$. In case a) the count of possibilities c_k is plotted over the number of matching bits k. It is obvious that a symmetric distribution is found: therefore, a full match of $k = 10$ is reached as

often as a full mismatch $k = 0$ in $c_0 = c_{10} = 1$ times. One matching bit $k = 1$ or one mismatching one $k = 9$ is, therefore, possible in $c_1 = c_9 = 10$ different cases. The occurrence probability for each number of bits p_k is derived by scaling the diagram (see right scale of Figure 6.20/a) according to equation (6.30).
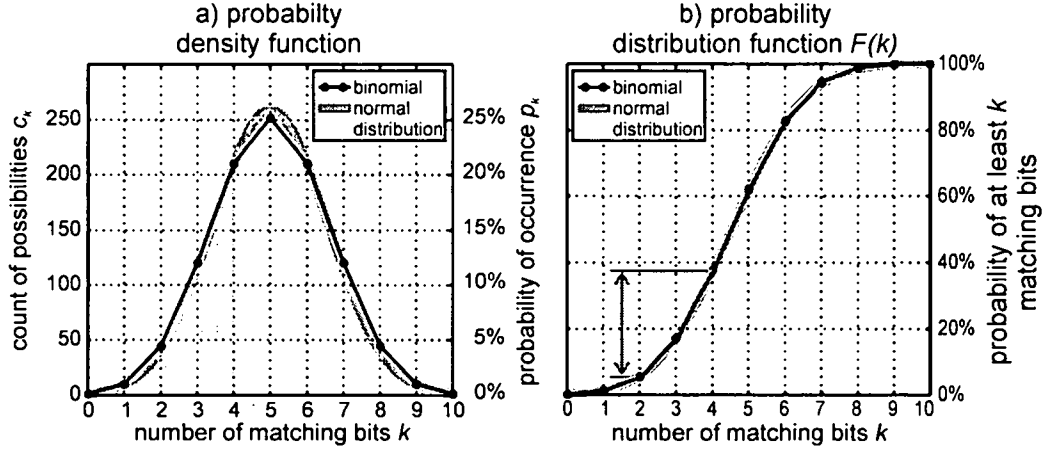
Figure 6.20: Example of binomial distribution with length $N = 10$ providing
a) the probability density function and b) the probability distribution function
in comparison with normal distribution

In Figure 6.20/b the distribution function of the given example is plotted. It provides the probability if a number of matching bits k or below is reached. For example, a maximum number of matching bits $k = 3$ is reached in about $F(3) = 17\%$ of all possible cases. The distribution function $F(k)$ further allows calculating the probability that a given range of matching bits is reached. For example the probability that a sample contains matching bits in the range of $2 \le k \le 4$ (gray shaded area in Figure 6.20/a) is calculated using the distribution function $F(k)$: $F(4) - F(2) = 32.23\%$ (see marked vertical distance in Figure 6.20/b).

According to [Kre99] for large numbers of N the binomial distribution can be approximated by the normal distribution whose general form is given in the following. The distribution density $f_{norm}(x)$ is defined by

$$f_{norm}\left(x\right) = \frac{1}{\sigma\sqrt{2\pi}} e^{-\frac{1}{2}\left(\frac{x-\mu}{\sigma}\right)^2}$$

(6.31)

containing the mean value μ and the standard deviation σ. The related distribution function $F_{norm}(x)$ is given by

$$F_{norm}\left(x\right) = \frac{1}{\sigma\sqrt{2\pi}} \int_{-\infty}^{x} e^{-\frac{1}{2}\left(\frac{\upsilon-\mu}{\sigma}\right)^2} d\upsilon .$$

(6.32)

As equation (6.32) cannot be integrated by one of the methods of calculus, a standardized normal distribution with mean $\mu = 0$ and standard deviation $\sigma = 1$ is provided with $\Phi(x)$ in equation (6.33).

$$\Phi(x) = \frac{1}{\sqrt{2\pi}} \int_{-\infty}^{x} e^{-\frac{u^2}{2}} du \qquad (6.33)$$

The solution of this equation is provided in tables or approximations and the solution of the general form in equation (6.32) is found using the following substitution:

$$F_{norm}(x) = \Phi\left(\frac{x-\mu}{\sigma}\right) \qquad (6.34)$$

Another important definition is the Gaussian error integral $Q(x)$ defined as following:

$$Q(x) = 1 - \Phi(x) = \frac{1}{\sqrt{2\pi}} \int_{x}^{\infty} e^{-\frac{u^2}{2}} du \qquad (6.35)$$

The general binomial distribution density from equation (6.30) is approximated by the normal distribution of equation (6.31) using the following substitutions for the mean value μ and the standard deviation σ:

$$\mu = N\,p$$
$$\sigma = \sqrt{N\,p\,q} \qquad (6.36)$$

An estimation of the binomial distribution function to calculate the probability P that a number of x bits in the range of $a \le x \le b$ is matching is given by the following equation

$$P(a \le X \le b) = \sum_{x=a}^{b} \binom{N}{x} p^x q^{N-x} \approx \Phi(\beta) - \Phi(\alpha) \qquad (6.37)$$

using the standardized normal distribution $\Phi(x)$ and the substitutions α and β:

$$\alpha(a) = \frac{a - N\,p - 0.5}{\sqrt{N\,p\,q}} \xrightarrow{p=q=\frac{1}{2}} \frac{2a - N - 1}{\sqrt{N}}$$

$$\beta(b) = \frac{b - N\,p + 0.5}{\sqrt{N\,p\,q}} \xrightarrow{p=q=\frac{1}{2}} \frac{2b - N + 1}{\sqrt{N}} \qquad (6.38)$$

According to [Cra46] the term 0.5 in α and β is a correction caused by the change from a discrete to a continuous distribution. In Figure 6.20/b the results of equation (6.37) are plotted together with the binomial distribution function (with $a = 0$ and $b = k$).

6.3.3.2 Evaluation of correlation results occurring due to white Gaussian noise

In this work a signal is expected to be received whenever a minimum correlation result κ_{min} is exceeded. The presented statistical equations allow an evaluation of a relation between the minimum correlation results κ_{min} and the probability $P_{\kappa,min}$ to exceed at least this value in case of only white Gaussian noise at the input and the length of the correlator N. In the following, the correlation result κ_{min} which is expected to be exceeded with a probability of e.g. $P_{\kappa,min} = 1\,ppm$ (only one measurement of 10^6 delivers a correlation result above the given value κ_{min}) is derived: assuming a sufficiently large correlator length N (which is surely given in case of a

required probability of $P_{\kappa,min} = 1\ ppm$), the binomial distribution is approximated by the normal distribution. As the normal distribution function cannot be solved, the standardized distribution function $\Phi(x)$ is used instead (equation (6.37) with $a = k$ and $b = N$) whose solutions are found in tables (e.g. in [Kre99]). Next, the inverse standardized distribution function

$$\alpha_{\kappa,min} = \Phi^{-1}\left(\underbrace{\Phi(\beta(N))}_{\approx 1\ \text{for large N}} - P_{\kappa,min}\right) \approx \Phi^{-1}\left(1 - P_{\kappa,min}\right) = Q^{-1}\left(P_{\kappa,min}\right) \qquad (6.39)$$

provides a value of $\alpha_{\kappa,min} = 4.753$ in case of $P_{\kappa,min} = 1\ ppm$. According to equation (6.38) the minimum number of matching bits $a_{\kappa,min}$ is evaluated by

$$a_{\kappa,min} = \alpha_{\kappa,min}\sqrt{N\ p\ q} + 0.5 + N\ p \xrightarrow{p=q=\frac{1}{2}} \frac{1}{2}\left(\alpha_{\kappa,min}\sqrt{N} + 1 + N\right), \qquad (6.40)$$

and the minimum reached normalized correlation result κ_{min} is found to be

$$\kappa_{min} = \frac{a_{\kappa,min} - \dfrac{N}{2}}{\dfrac{N}{2}} = \frac{2\,a_{\kappa,min} - N}{N} = \frac{\alpha_{\kappa,min}}{\sqrt{N}} + \frac{1}{N}. \qquad (6.41)$$

In Table 6.1 and Figure 6.21 the results obtained by equation (6.41) are shown: the minimum expected relative correlation result κ_{min} which is exceeded with a probability of $P_{\kappa,min}$ is plotted over the correlation length N. As expected, with increasing correlation length noise suppression increases leading to lower correlation maxima occurring with the same probability.

$P_{\kappa,min}$	$\alpha_{\kappa,min}$	probability to exceed the minimum correlation result κ_{min} in case of a correlator length N of		
		$N = 100$	$N = 1000$	$N = 10000$
1 ppm	4.753	47 %	15 %	5 %
100 ppm	3.719	36 %	12 %	4 %
1 %	2.326	22 %	7 %	2 %

Table 6.1: Expected minimum normalized correlation results κ_{min} depending on probability of occurrence $P_{\kappa,min}$ and correlation length N

Figure 6.21 further allows an estimation of the probability of wrong measurements (erroneous signal detection) depending on the correlation length N. Assuming a signal to be received when e.g. a threshold of $\kappa_{thres} = 50\ \%$ is exceeded: one out of 100 correlations exceeds the threshold in case of a correlation length of about 20 bits (light gray line representing $P_{\kappa,min} = 1\ \%$), while in case of 80 bits it is only one out of 1000000 correlations (black line). This sounds rather high, however, it must be taken into account that a correlation result is evaluated at each sampling time: assuming a sampling rate of $f_{sample} = 1\ MHz$, the black line in Figure 6.21 depicts the border of the correlation result κ_{min} which is exceeded once every second.
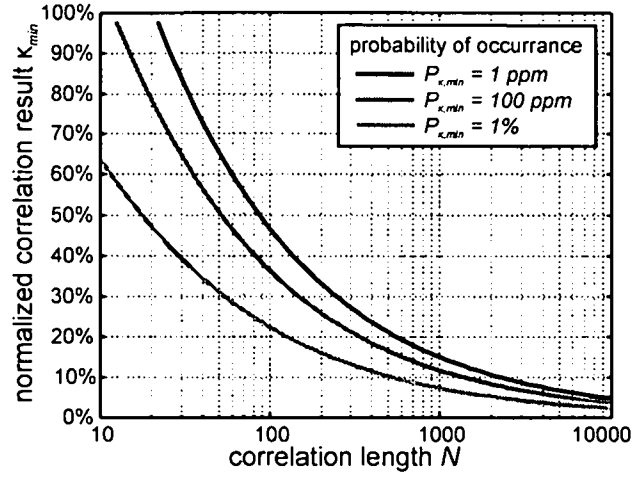
Figure 6.21: Expected minimum normalized correlation results κ_{min}
depending on probability of occurrence $P_{\kappa,min}$ over the correlation length N

To evaluate the distribution of the minimum border of the correlation result κ_{min} depending on the length of the correlator N, the minimum reached value κ_{min} is assumed to be given, and, using equation (6.41), the argument $\alpha_{\kappa,min}$ is evaluated by

$$\alpha_{\kappa,min} = \sqrt{N}\left(\kappa_{min} - \frac{1}{N}\right) = \frac{\overbrace{\kappa_{min}}^{x} - \overbrace{\frac{1}{N}}^{\mu}}{\underbrace{\frac{1}{\sqrt{N}}}_{\sigma}}. \tag{6.42}$$
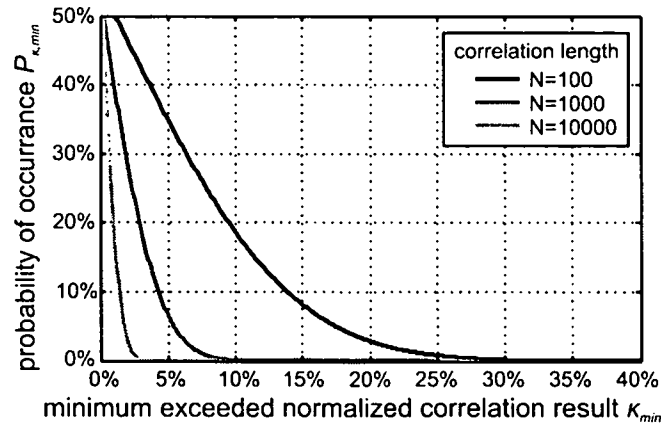
Figure 6.22: Probability of occurrence $P_{\kappa,min}$
over minimal exceeded correlation result κ_{min}
for different correlation lengths N

A comparison with the general form of the distribution function in equation (6.34) leads to the parameters μ and σ:

$$\mu = \frac{1}{N} \quad \text{and} \quad \sigma = \frac{1}{\sqrt{N}} \tag{6.43}$$

With equation (6.39) the probability of occurrence $P_{\kappa,min}$ for each value of κ_{min} is derived by

$$P_{\kappa,min} \approx Q(\alpha_{\kappa,min}) = Q\left[\sqrt{N}\left(\kappa_{min} - \frac{1}{N}\right)\right] \tag{6.44}$$

In Figure 6.22 some results obtained by equation (6.44) are plotted. While this figure shows the influence of different correlation lengths very well, due to its large scale it is not suitable for further analyses, because in most cases the interesting regions are located in the range of $P_{\kappa,min}$ of several *ppm* (compare Figure 6.21).

6.3.3.3 Influences of white Gaussian noise on the correlation results

In the following the influence of white Gaussian noise added to a received signal, as shown in Figure 6.23 (*SNR = 0 dB*), is evaluated. In case of one bit correlation it is obvious that disturbances only influence the correlation result when they are strong enough to change the value of at least one bit in the digitized signal.
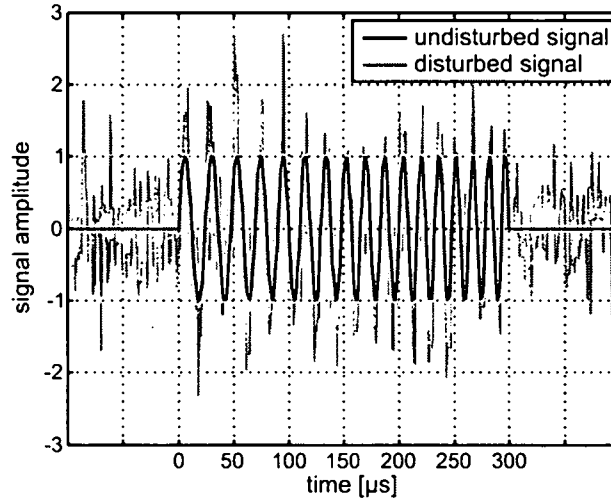
Figure 6.23: Undisturbed signal (black)
and disturbed signal with SNR of 0dB (light gray)

This is accomplished whenever the added noise causes a change of the signal sign (assuming a threshold-amplitude $A_{thres} = 0$ of the discriminator). According to [Kro96] the probability P_{error} that white Gaussian noise with an effective value of A_{noise} exceeds a defined amplitude range $A_{defined}$ can be calculated using the error integral $Q(x)$ from equation (6.35) to

$$P_{error} = Q(x) = \frac{1}{\sqrt{2\pi}} \int\limits_{x}^{\infty} e^{-\frac{u^2}{2}} du \quad \text{with} \quad x = \frac{A_{defined}}{A_{noise}}. \tag{6.45}$$

As the actual signal amplitude $A(t)$ changes during time, also the error probability varies and, therefore, the final result depends on the amplitude distribution of the used signal. In case of a chirp as used in this work, the amplitude distribution equals the distribution obtained by a

normalized sinusoidal signal $A(x) = sin(x)$ multiplied by the maximum signal amplitude A_{max}. In the range of $-\pi/2 \leq x \leq \pi/2$ all possible values in the amplitude range of $-1 \leq A \leq 1$ are reached. The first derivative of the inverse function with an additional scaling factor

$$D_{sign}(A) = \frac{d}{dA} \frac{\arcsin(A)}{\pi} = \frac{1}{\pi\sqrt{1-A^2}}$$ (6.46)

leads to the amplitude distribution as shown in Figure 6.24/a.
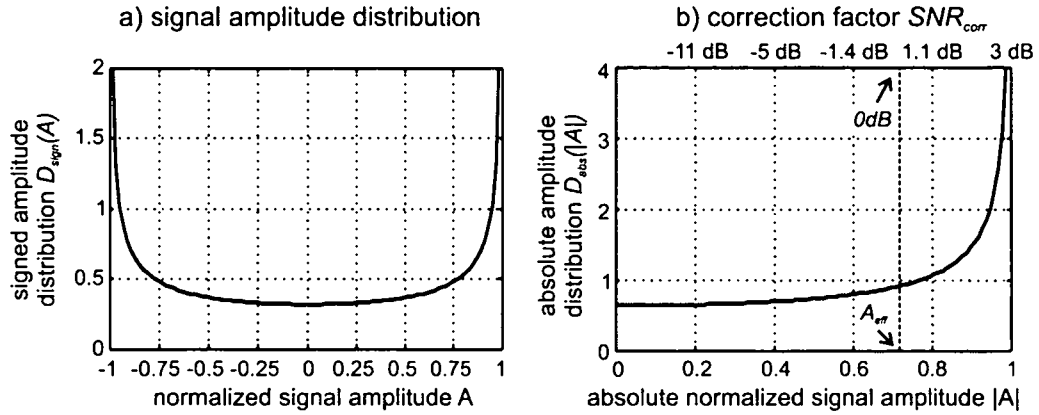
Figure 6.24: Amplitude distribution of sinusoidal signal:
a) signed amplitude distribution $D_{sign}(A)$ and
b) absolute amplitude distribution $D_{abs}(A)$ also scaled with correction factor SNR_{corr}

However, in case of Gaussian noise the sign of the amplitude A does not matter and, therefore, only the absolute value $|A|$ is of interest. Due to the symmetry of D_{sign}, the distribution of the absolute value D_{abs} shows twice the height of D_{sign} and is defined in the range $0 \leq |A| \leq 1$ (see Figure 6.24/b).

In most cases the strength of the noise is defined by the signal to noise ratio

$$SNR_{sig} = 20\log_{10}\left(\frac{A_{sig,eff}}{A_{noise}}\right) = 20\log_{10}\left(\sqrt{\frac{E_{sig}}{E_{noise}}}\right) = 10\log_{10}\left(\frac{E_{sig}}{E_{noise}}\right)$$ (6.47)

based on the signal and noise amplitudes $A_{sig,eff}$ and A_{noise} respectively on their energies E_{sig} and E_{noise}. While the effective value $A_{sig,eff}$ of the whole sinusoidal signal is defined by

$$A_{eff} = \frac{1}{\sqrt{2}} A_{max},$$ (6.48)

the Gaussian noise affects each sampled value A_{sample} separately, leading to a signal to noise ratio depending on the amplitude A_{sample} of each sample:

$$SNR_{sample}\left(A_{sample}\right) = 20 \log_{10}\left(\frac{A_{sample}}{A_{noise}}\right) =$$

$$= 20 \log_{10}\left(\frac{A_{sig,eff}}{A_{noise}}\right) + SNR_{corr}\left(A_{sample}\right) \quad (6.49)$$

$$\underbrace{\qquad\qquad\qquad}_{SNR_{sig}}$$

The correction value $SNR_{corr}(A_{sample})$ is calculated to

$$SNR_{corr}\left(A_{sample}\right) = 20 \log_{10}\left(\frac{\overbrace{A \cdot A_{max}}^{A_{sample}}}{\underbrace{A_{eff}}_{\frac{A_{max}}{\sqrt{2}}}}\right) = 20 \log_{10}\left(\sqrt{2}\, A\right) \quad (6.50)$$

and depends only on the normalized signal amplitude A. This allows scaling of the x-axis of the amplitude distribution to the actual correction factor (see top scale in Figure 6.24/b): as expected, the correction term SNR_{corr} causes a strong decrease of the effective signal to noise ratio with decreasing signal amplitude.

According to equation (6.45) the probability to achieve a wrong bit depends on the value of the actual signal to noise ratio

$$x_{SNR}\left(SNR_{sig}, A\right) = 10^{\frac{SNR_{sample}}{20}} = 10^{\frac{SNR_{sig} + SNR_{corr}(A)}{20}} = 10^{\frac{SNR_{sig}}{20}}\sqrt{2}\, A . \quad (6.51)$$

In case of the one bit correlation process the mean probability $P_{error,mean}$ of a bit error is of interest as it allows evaluating the mean number of disturbed bits $k_{disturb} = N\, P_{error,mean}$ and of the expected correlation result

$$k = N - k_{disturb} = N\left(1 - P_{error,mean}\right) \quad (6.52)$$

The normalized correlation result κ is further calculated to

$$\kappa = \frac{k - \frac{N}{2}}{\frac{N}{2}} = \frac{2\,N\left(1 - P_{error,mean}\right) - N}{N} = 1 - 2\,P_{error,mean} . \quad (6.53)$$

The mean error probability $P_{error,mean}$ is the sum of weighted error probabilities P_{error} of each bit using the amplitude distribution function of equation (6.46) and the error probability depending on the actual signal to noise ratio (6.51). This leads to the following equation:

$$P_{error,mean}\left(SNR_{sig}\right) = \int_0^1 \underbrace{D_{abs}\left(A\right)}_{\text{amplitude distribution}} \underbrace{Q\left[x_{SNR}\left(SNR_{sig}, A\right)\right]}_{\text{error probability}} dA =$$

$$= \int_0^1 \underbrace{\frac{2}{\pi\sqrt{1-A^2}}}_{\text{amplitude distribution}} \underbrace{Q\left(10^{\frac{SNR_{sig}}{20}}\sqrt{2}\,A\right)}_{\text{error probability}} dA \qquad (6.54)$$

To verify the results obtained by equations (6.53) and (6.54) some simulations are carried out and compared with the calculation: in Figure 6.23 the undisturbed linear chirp from Figure 6.2 is shown with added white Gaussian noise, resulting in a signal to noise ratio of $SNR = 0\ dB$ (original undisturbed signal is plotted light gray). The corresponding correlation result is shown in Figure 6.25 and its correlation maximum providing a value of about $\kappa = 63\ \%$ is well detectable.
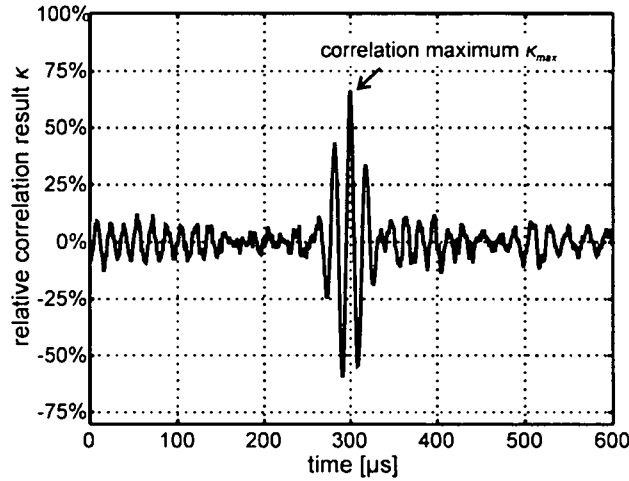
Figure 6.25: Correlation result of disturbed signal from Figure 6.23

As random results occur due to the added white noise, 50 measurements are taken at each signal to noise ratio SNR in the range of $-10\ dB \leq SNR \leq 30\ dB$ and the evaluated minimum and maximum values are evaluated and contribute the limits of this measurement. In Figure 6.26 these simuation results (light gray area) are compared with the calculation results (black line) obtained by equation (6.53) and good agreements are obtained.

6.3.3.4 Influence of SNR to recognizability of signals

In the previous chapters the two main effects affecting the recognizability of signals are described:

- In chapter 6.3.3.2 a border of the maximum correlation result κ_{min} obtained in case of uncorrelated input signals is evaluated. This border depends on the length of the reference pattern N of the one bit correlation method and decreases with increasing N (see equation (6.41) and dashed lines in Figure 6.27). As in this case no input signal except noise is provided and the one bit correlation only evaluates the sign but not the amplitude of the signal, this border is independent of the amplitude of the noise.

- In chapter 6.3.3.3 the influence of the noise to the maximum correlation result is discussed. As shown in equation (6.54) it depends only on the signal to noise ratio *SNR* and not on the length of the reference pattern (see solid line in Figure 6.27).
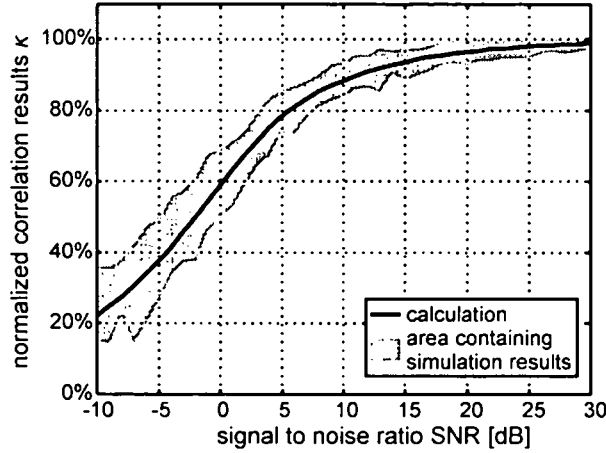
Figure 6.26: Comparison of relative correlation maxima at different SNRs:
results obtained by calculation (black solid) and
area of obtained simulation results (gray area)

Valid signal detection is possible only when the correlation maximum in case of signal detection is significantly greater than the correlation peaks obtained without input signal. The dashed lines in Figure 6.27 show borders that are exceeded by correlation results with a probability of $P_{\kappa,min} = 10^{-9}$ (in case of $f_{sample} = 1$ *MHz* one correlation exceeds this border every quarter of an hour) in case of white noise as input.
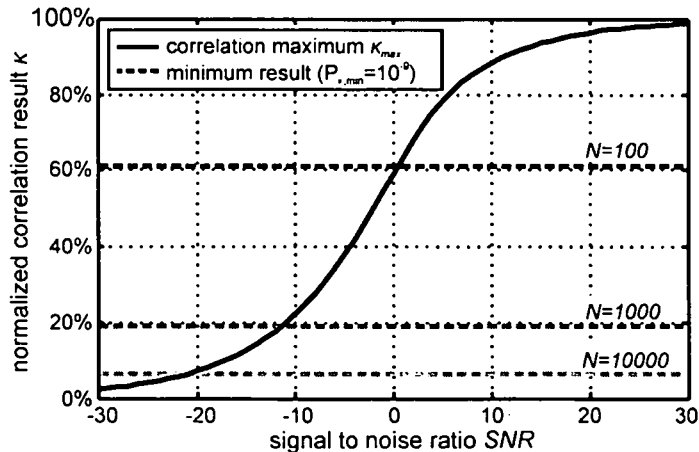
Figure 6.27: Maximum correlation result depending on signal to noise ratio (solid line)
and minimum border of correlation peaks (with probability $P_{\kappa,min} = 10^{-9}$)
at different correlation pattern lengths ($N = 100, 1000$ and 10000)

In the following example the minimum necessary correlation length N_{min} is calculated that is necessary in case of a signal to noise ratio of $SNR = 0$ *dB* to achieve good correlation results

which mean that evaluated correlation maximum κ_{max} is at least $6\,dB$ higher than correlation peaks κ_{min}. The probability of wrong signal detection should be less than $P_{\kappa,min} = 10^{-9}$.

At first the expected amplitude of the correlation result κ_{max} which is affected by the signal to noise ratio SNR is calculated using equation (6.53) and equation (6.54) which must be solved numerically:

$$\kappa_{max} = 1 - 2 \underbrace{P_{error,mean}(SNR)}_{SNR=0 \;\to\; P_{error,mean}=0.2048} = 59\,\% . \tag{6.55}$$

The requested safety margin of $6\,dB$ leads to a border of the correlation peaks occurring only due to white noise at the input of

$$\kappa_{min} = \frac{\kappa_{max}}{\underbrace{2}_{-6\,dB}} = 29.5\,\% . \tag{6.56}$$

With equation (6.39) a value for $\alpha_{\kappa,min} = 6$ is found according to the requirement of exceeding the border of κ_{min} with a probability of $P_{\kappa,min} = 10^{-9}$. Solving equation (6.41) finally leads to the minimum length N_{min} of the reference pattern

$$N_{min} \geq \left(\frac{\alpha_{\kappa,min} + \sqrt{\alpha_{\kappa,min}^2 + 4\,\kappa_{min}}}{2\,\kappa_{min}} \right)^2 = 421 . \tag{6.57}$$

6.3.3.5 Short noise bursts

As shown in chapter 6.2 the result of the one bit correlation is the sum of coincident bits of the received bit stream with the reference pattern. Therefore, a short disturbance leads to a degradation of the full correlation result proportional to the length of the disturbance:

$$\kappa_{max,dist} = 1 - \eta \underbrace{\frac{T_{disturbed}}{T_{signal}}}_{T_{dist,rel}} \tag{6.58}$$

The disturbance coefficient η depends on the strength of the disturbance: in case of high amplitudes leading to total disturbance of the original signal, which causes a correlation result of zero during the disturbed part, the disturbance coefficient is $\eta = 1$. This leads to a degradation of the correlation result equal to the relative length of the disturbance $T_{dist,rel}$. In case of disturbances with lower amplitudes, the affected correlation part is not fully erased, leading to a lower disturbance coefficient η which depends on the signal to noise ratio of the received signal. Assuming a relative correlation maximum of $\kappa_{disturbance}$ due to a given SNR, the disturbance coefficient is given by

$$\eta = 1 - \kappa_{disturbance} . \tag{6.59}$$

The dependency of the correlation maximum on the signal to noise ratio (SNR) was described in chapter 6.3.3.3.

6.3.4 Coding possibilities

According to the evaluation shown in chapter 6.1 the transmitted signal of a pulse compression system depends on the impulse response of the filter $p(t)$ and the receiver requires a corresponding matched filter $p^{*}(-t)$. This offers the possibility of using different pairs of filters $p_x(t)$ and $p_x^{*}(-t)$ whose cross correlations

$$p_i(t) * p_{j \neq i}^{*}(-t) \tag{6.60}$$

do not provide explicit peaks. In the following example the impulse responses $p_x(t)$ are linear chirps with the same center frequency $f_0 = 55\ kHz$ and bandwidth $B = 30\ kHz$, the first chirp shows an increasing and the second a decreasing frequency characteristic. In Figure 6.28 a signal containing the two signals s_1 and s_2 generated by the filters p_1 and p_2 is plotted.
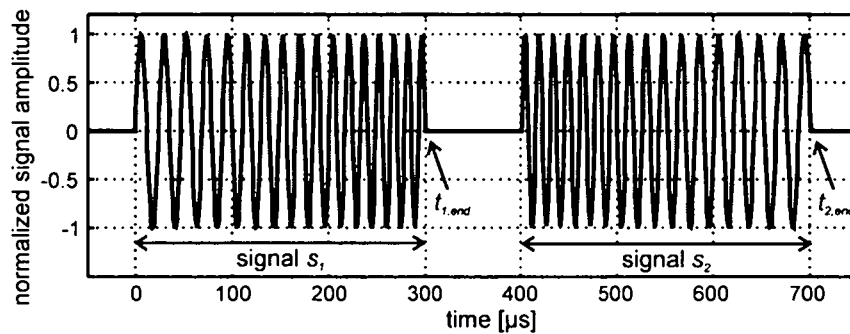
Figure 6.28: Example of two different signals s_1 and s_2

After receiving, this combined signal is evaluated separately by the two matched filters $p_{1/2}^{*}(-t)$. The calculated correlation results are shown in Figure 6.29.
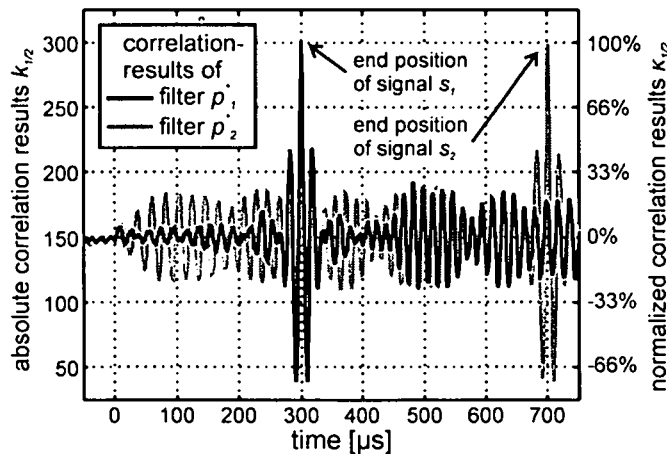
Figure 6.29: Correlation results of different receivers

Each filter detects its "own" signal only whereas the other is suppressed: therefore, filter $p_1^{*}(-t)$ produces its maximum κ_{max} at the end of the signal s_1 ($t_{1,end} = 300\ \mu s$) and filter $p_2^{*}(-t)$ at $t_{2,end} = 700\ \mu s$, respectively.

This coding ability allows implementation of advanced features as presented in chapter 3.4.1.

7 Transducer Model

Most ultrasonic transducers can be described by the model of a piston membrane. This model is extensively evaluated in [Zol98]. In the following, only a short evaluation is presented, containing the crucial points for this work.

In Figure 7.1, a schematic of a piston membrane is shown. For the calculation it is considered to be an in-phase vibrating plane that is mounted in a rigid wall with infinite dimensions. The rotational symmetry (z-axis) of the assembly allows defining the measuring point $P_M(r, \Theta)$ by just two variables. Only the far sound field of the assembly is evaluated. Therefore, the acoustic pressure at the measuring point P_M is assumed to be the sum of the partial acoustic pressures generated by infinitely small areas dS of the piston surface which are defined by the distance ε from the center and by the angle σ (compare Figure 7.1).
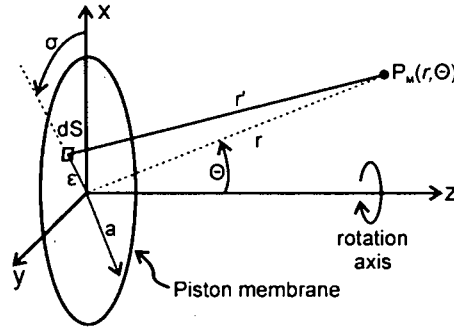
Figure 7.1: Schematic of piston membrane

According to the Huygens principle each infinitely small area dS defined by

$$dS = \varepsilon \, d\varepsilon \, d\sigma \qquad (7.1)$$

emits a hemispherical wave providing a partial acoustic pressure dp at the measuring point P_M of

$$\underline{dp} = j \frac{Z_0 \, k}{2\pi \, r'} \hat{v} \, dS \, e^{j(\omega t - kr')} = j \frac{Z_0 \, k}{2\pi \, r'} \hat{v} \, \varepsilon \, d\varepsilon \, d\sigma \, e^{j(\omega t - kr')}, \qquad (7.2)$$

where Z_0 is the characteristic wave impedance, $\hat{v}$ the peak sound particle velocity, t the time, k the wave number and r' the distance from the infinite small area dS to the measuring point P_M. For each dS of the piston membrane the distance r' is calculated to

$$r' = \sqrt{r^2 + \varepsilon^2 - 2 \, r \, \varepsilon \, \sin(\Theta) \cos(\sigma)} \approx r - \varepsilon \sin(\Theta) \cos(\sigma), \qquad (7.3)$$

where the latter simplification requires far field considerations ($r \gg \varepsilon$, $r \gg \dfrac{\varepsilon^2}{\lambda}$). Substitution of equation (7.3) in (7.2) leads to

$$
\begin{aligned}
d\underline{p} &\approx j\frac{Z_0\, k\, \hat{v}}{2\pi\, r}\, e^{j[\omega t - k\, r + k\,\varepsilon\,\sin(\Theta)\cos(\sigma)]} = \\
&= j\frac{Z_0\, k\, \hat{v}}{2\pi\, r}\, e^{j(\omega t - k\, r)}\, \underbrace{e^{j[k\,\varepsilon\,\sin(\Theta)\cos(\sigma)]}d\sigma\,\varepsilon\,d\varepsilon}_{\text{piston membrane effect}}
\end{aligned}
\tag{7.4}
$$

$$\underbrace{\qquad\qquad}_{\text{spreading wave } \underline{P}}$$

While the first part $\underline{P}$ of equation (7.4) represents a basic spreading wave, the second part presents the effect of the piston membrane. The resulting pressure $\underline{p}(r,\Theta)$ on the measuring point P_M is the sum of all waves generated by each infinitely small area dS of the piston. Therefore, the integral

$$
\underline{p}(r,\Theta) = \int_S d\underline{p} = \underline{P}\int_{\varepsilon=0}^{a}\varepsilon\underbrace{\int_{\sigma=0}^{2\pi} e^{j\,k\,\varepsilon\,\sin(\Theta)\cos(\sigma)}d\sigma}_{\underline{C}}\,d\varepsilon
\tag{7.5}
$$

must be evaluated over the whole piston area. The zero order Bessel function J_0, defined by

$$
J_0(x) = \frac{1}{2\pi}\int_0^{2\pi} e^{j\,x\cos(\varphi)}d\varphi,
\tag{7.6}
$$

is used to simplify equation (7.5) according to

$$
\underline{C} = \int_{\sigma=0}^{2\pi} e^{j\,k\,\varepsilon\,\sin(\Theta)\cos(\sigma)}d\sigma = 2\pi\, J_0\big[k\,\varepsilon\,\sin(\Theta)\big],
\tag{7.7}
$$

which leads to

$$
\underline{p}(r,\Theta) = 2\pi\,\underline{P}\int_{\varepsilon=0}^{a}\varepsilon\, J_0\big[k\,\varepsilon\,\sin(\Theta)\big]d\varepsilon.
\tag{7.8}
$$

To solve the last remaining integral, the first order Bessel function $J_1(x)$ is introduced as follows

$$
x\, J_1(x) + C_1 = \int x\, J_0(x)\,dx.
\tag{7.9}
$$

This equation is implemented by expanding (7.8) with $k\,\varepsilon\,sin(\Theta)$ and by substituting ε with $k\,\varepsilon\,sin(\Theta)$ to get

$$\underline{p}(r,\Theta) = 2\pi \, \underline{P} \, \int_{k\varepsilon\sin(\Theta)=0}^{ka\sin(\Theta)} \frac{1}{\left[k\sin(\Theta)\right]^2} k \, \varepsilon \, \sin(\Theta) \, J_0\left[k \, \varepsilon \, \sin(\Theta)\right] d\left[k \, \varepsilon \, \sin(\Theta)\right] =$$

$$= \frac{2\pi \, \underline{P}}{\left[k\sin(\Theta)\right]^2} \left\{k \, \varepsilon \, \sin(\Theta) \, J_1\left[k \, \varepsilon \, \sin(\Theta)\right]\right\}_0^{k\,a\,\sin(\Theta)} = \tag{7.10}$$

$$= \frac{2\pi \, \underline{P}}{\left[k\sin(\Theta)\right]^2} k \, a \, \sin(\Theta) \, J_1\left[ka\sin(\Theta)\right]$$
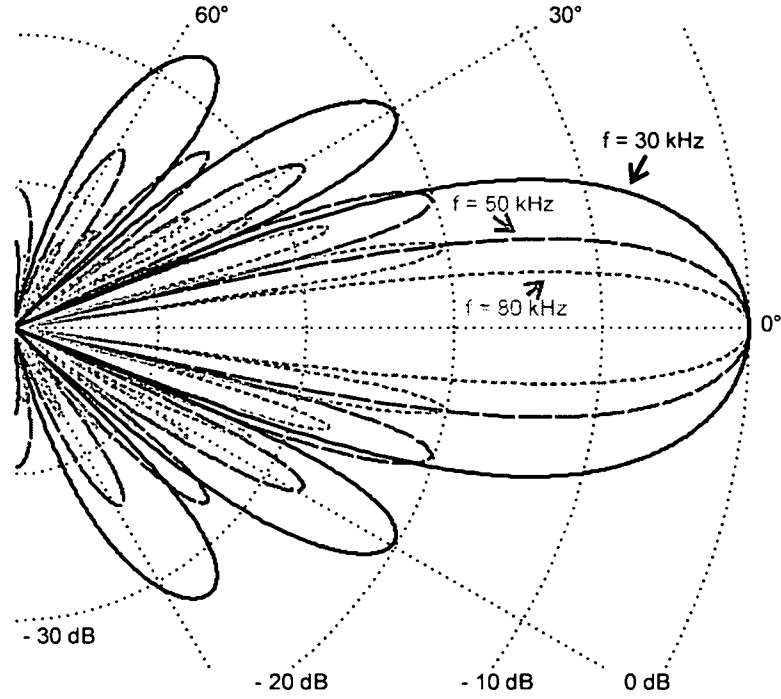
Figure 7.2: Evaluation of antenna pattern Γ_{piston} for a transducer diameter of $2a = 35$ mm at three different signal frequencies f (30 kHz, 50 kHz and 80 kHz)

A final simplification of equation (7.10) leads to

$$\underline{p}(r,\Theta) = \pi \, a^2 \underline{P} \underbrace{\frac{2 \, J_1\left[k \, a \, \sin(\Theta)\right]}{k \, a \, \sin(\Theta)}}_{\Gamma_{piston}}, \tag{7.11}$$

where the latter part is the antenna pattern Γ_{piston} of the piston membrane which only depends on the direction Θ, the radius of the piston membrane a and the wave number k. The wave number k directly connects the signal frequency f, the speed of sound c and the wavelength λ as shown in equation (7.12):

$$k = \frac{\omega}{c} = \frac{2\pi \, f}{c} = \frac{2\pi}{\lambda} \tag{7.12}$$

As mentioned before, the antenna pattern Γ_{piston} depends on the signal frequency f and on the transducer diameter $2a$. In Figure 7.2, a polar diagram of the antenna patterns Γ_{piston} for a

transducer with a diameter of $2a = 35$ mm at three different signal frequencies (30 kHz, 50 kHz and 80 kHz) are shown. The main differences are found in the widths of the main and side lobes: with increasing frequency the lobes become smaller.

In Figure 7.3, the antenna pattern

$$\Gamma_{piston}\left[ka\sin(\Theta)\right] = \frac{2\,J_1\left[ka\sin(\Theta)\right]}{ka\sin(\Theta)} \tag{7.13}$$

is plotted over its argument $k\,a\,sin(\Theta)$. It allows evaluation of its properties independent of the actual signal frequency. Figure 7.3 is plotted linearly scaled to be able to examine the sign of the result of equation (7.13).
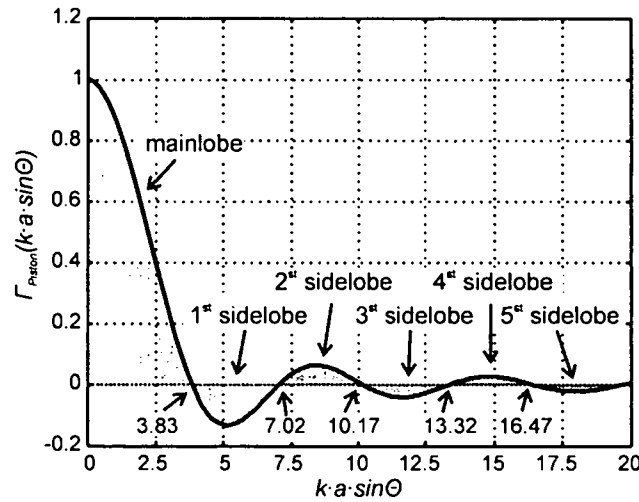
Figure 7.3: Antenna pattern Γ_{piston} of a piston membrane

Generally the radiation pattern consists of a main lobe and several side lobes providing increasing attenuation. At the center of the main lobe ($\Theta = 0°$) the direction factor Γ_{piston} is equal to one and, therefore, a signal is transmitted with full amplitude. With increasing angle Θ the interference effects increase until the argument of the direction factor reaches a value of about $k\,a\,sin\Theta = 3.83$ (compare Figure 7.3 and Table 7.1), where the first null is found due to the occurring destructive interference. The corresponding angle Θ depends on the transducer diameter $2a$ and the actual signal frequency. In Table 7.1, a transducer diameter of $2a = 35$ mm is assumed and some basic parameters (angle, where side lobe starts and angular position of the maximum) for three different signal frequencies are calculated (30 kHz, 50 kHz and 80 kHz – corresponding to Figure 7.2). As shown there, the crossover from the main lobe to the first side lobe occurs, depending on the actual signal frequency, at $22.53°$ (30 kHz), $13.29°$ (50 kHz) respectively $8.26°$ (80 kHz). Further increasing of Θ leads to signal transmission through the first side lobe. According to Figure 7.3 the direction factor Γ_{piston} is negative in this and each second following side lobe (with odd numbers) and, therefore, a phase shift of 180° is provided to the transmitted signal. In Figure 7.2 this effect is not visible because a logarithmic presentation of the absolute value is shown there.

The presented measurement system discards the amplitude information and evaluates the phases of the signal only. In case of an ideal piston membrane the phase only takes a value of 0° (main lobe and even numbered side lobes) and 180° (odd numbered side lobes).

Side-lobe	begin at $[k \cdot a \cdot \sin d\Theta]$	maximum at $[k \cdot a \cdot \sin\Theta]$	maximal attenuation	$f = 30\ kHz$		$f = 50\ kHz$		$f = 80\ kHz$	
				begin	max.	begin	max.	begin	max.
1	3.8317	5.13	17.57dB	22.53°	30.88°	13.29°	17.93°	8.26°	11.10°
2	7.0156	8.41	23.81dB	44.61°	57.28°	24.92°	30.32°	15.27°	18.39°
3	10.1735	11.61	27.98dB			37.63°	44.56°	22.44°	26.01°
4	13.3237	14.79	31.08dB			53.08°	62.59°	29.98°	33.70°
5	16.4706	17.95	33.59dB			81.34°		38.16°	42.33°

Table 7.1: Evaluation of the side lobes of the direction coefficient Γ_{piston}
at different frequencies f

In chapter 9.3.2 the transducer used in the prototype is evaluated according to its amplitude and phase behavior. The measured results are compared with the expected theoretical results and the effects to the measurement method are discussed.

8 Final measurement system

The final measurement system is based on the one bit correlation that allows achieving the requirements discussed in chapter 5. The main feature of the new measurement system is the well defined detection area that is moreover independent of the reflection properties of the object. Moreover, the detection area can be adjusted which allows on the one hand a compensation of the temperature effect to the angle of detection and on the other hand it can be used to perform a so called "soft scan" to enhance the speed of scan based systems.

8.1 Well defined detection area

As shown in the following, a well defined detection area is achieved by evaluation of the radiation pattern of the ultrasonic transmitter.

8.1.1 Theoretical evaluation

In chapter 7 the radiation pattern of a piston type transmitter is shown, which mainly depends on the actual signal frequency f. In equation (7.13) the radiation pattern Γ_{piston} valid for a given transducer with radius a and a signal with wave number k is shown. The new measurement method analyzes the crossover from the main lobe to the first side lobe. An evaluation of the radiation pattern Γ_{piston}, also shown in Figure 7.3, leads to

$$3.83 = k\, a \sin\left(\Theta_z\right) = \frac{2\pi f}{c} a \sin\left(\Theta_z\right).$$ (8.1)

Equation (8.1) shows the relation between the angular position Θ_z of the zero between main and side lobe and the wave number k and the actual frequency f of the transmitted signal. The use of wide bandwidth chirp signals generates a variety of different transmission patterns. As the one bit correlation (see chapter 6.2) evaluates only the sign but not the amplitude of the signal, only the signal phase is considered in the following. While no phase shifts occur in the directions near the sensor axis (all signal parts are transmitted through their main lobes – see Figure 8.1), at higher transmission angles signal parts with higher frequencies are transmitted through the first or even higher side lobes.

In case of a linear chirp with center frequency f_0, bandwidth B (relative bandwidth $B_{rel} = B / f_0$) and total length T, at $t = 0\,s$ the start frequency $f_{start} = f_0 - B/2$ and at the end $t = T$ the end-frequency $f_{end} = f_0 + B/2$ (assuming a linear chirp with increasing frequency) are found. The actual frequency $f(t)$ in the range $0 \leq t \leq T$ is calculated to

$$f(t) = f_{start} + t \frac{f_{end} - f_{start}}{T} = f_0 \left[1 + B_{rel} \left(\frac{t}{T} - \frac{1}{2} \right) \right]. \qquad (8.2)$$

Considering an angle of transmission Θ which denotes the angle of the zero point between the main and first side lobe at a specific frequency f_z of the chirp signal, one can derive the time t_z when the zero occurs from equations (8.1) and (8.2) to

$$t_z = \frac{T}{B} \left(\frac{3.83\, c}{2\pi\, a\, \sin(\Theta)} + \frac{B - 2 f_0}{2} \right). \qquad (8.3)$$
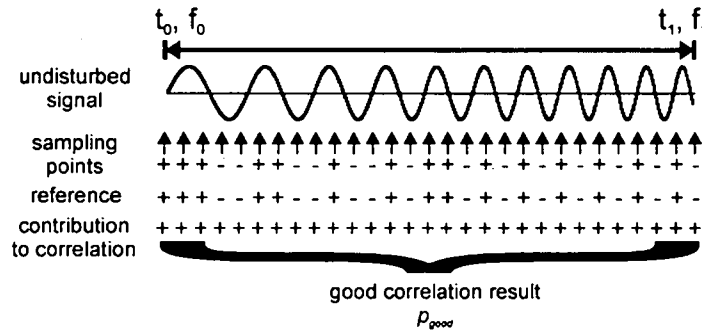
Figure 8.1: One bit correlation in case of a signal transmitted completely through main lobe leading to good correlation of whole signal
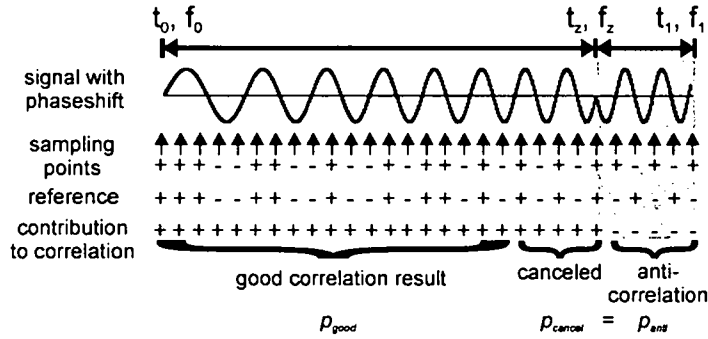
Figure 8.2: One bit correlation in case of a signal with partly transmission through the side lobe that provides a phaseshift of *180°* leading to anti correlation

Therefore, the first part of the signal $0 \le t \le t_z$ is transmitted through the main lobe without phase shift and the other part $t_z \le t \le T$ is affected by a phase shift of *180°* as it runs through the first side lobe. The relative part p_{main} of the signal running through the main lobe is calculated by

$$p_{main} = \frac{t_z}{T} = \frac{1}{B} \left(\frac{3.83\, c}{2\pi\, a\, \sin(\Theta)} + \frac{B - 2 f_0}{2} \right). \qquad (8.4)$$

Performing a one bit correlation of the received signal with a previously stored reference pattern as shown in Figure 8.2, p_{main} generates a positive contribution to the correlation result while $p_{side} = 1 - p_{main}$ produces a negative one due to the phase shift occurring within the side lobe.

As the part containing anticorrelation delivers the same absolute contribution to the final correlation result but with negative sign, it cancels another part of the same size. The remaining part p_{good} represents the final correlation result

$$p_{good} = \kappa = 1 - 2\, p_{side} = p_{main} - p_{side} = 2\, p_{main} - 1 =$$

$$= \frac{1}{B}\left(\frac{3.83\,c}{\pi\, a \sin(\Theta)} - 2\, f_0 \right) \qquad (8.5)$$

This relative part p_{good} corresponds to the relative correlation result κ obtained by the digital correlation.
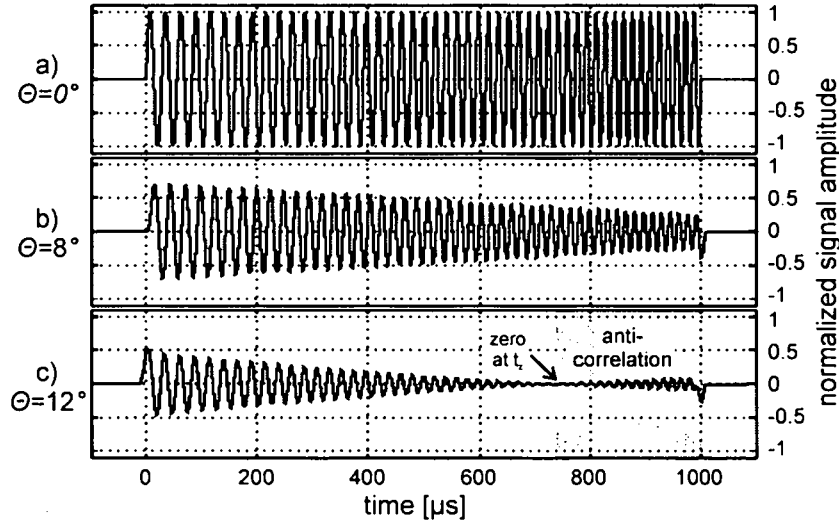
Figure 8.3: Chirps depending on angle of radiation,
case a) $\Theta = 0°$ and b) $\Theta = 8°$ without phase shift and
case c) $\Theta = 12°$ with phase shift providing anti correlation

In the following the results obtained by equation (8.5) for a varying radiation angle Θ are compared with the results obtained by the following simulation: a chirp signal with a length of $T = 1\ ms$, a center frequency of $f_0 = 50\ kHz$ and a bandwidth of $B = 30\ kHz$ (relative bandwidth $B_{rel} = 60\ \%$) runs through a filter that simulates the frequency response of a piston membrane at a specific radiation angle Θ. In Figure 8.3 three examples of radiated chirps at different radiation angles ($\Theta = 0°$, $\Theta = 8°$ and $\Theta = 12°$) are shown. While in case a) and b) only the amplitude of the signal is affected by the piston membrane model, in case c) some signal parts are already transmitted through the first side lobe leading to anticorrelation.

The transmitted signals expected at radiation angles in the range of $0° \le \Theta \le 20°$ are calculated and each one is evaluated by the one bit correlation algorithm. In Figure 8.4/a maxima of the correlation results are plotted over the actual angle of radiation Θ. They are compared with the results obtained by calculation (Figure 8.4/a). In the range of the slope ($10.5° \le \Theta \le 12$) good coincidence is visible. At lower angles the calculation leads to non valid results as (8.4) delivers

values of $p_{main} > 100\%$ which is not possible. At higher angles the correlation maximum located at the right positions is exceeded by other correlation maxima. Therefore, the maximum does not represent a valid position.
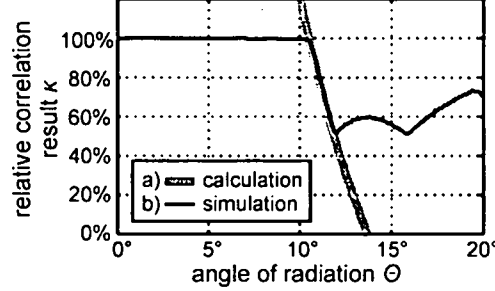
Figure 8.4: Comparison of a) calculation and b) simulation results

The angle sensitivity in the range of the slope ($10.6° \le \Theta \le 11.7°$) is calculated by calculating the first derivative of equation (8.5) with respect to the angle of radiation Θ to

$$\frac{d\kappa}{d\Theta} = -\frac{3.83\, c \cos(\Theta)}{B\,\pi\,a \sin(\Theta)^2}.$$

(8.6)

The sensitivity decreases with increasing of both the signal-bandwidth and the transmitter diameter. In the shown example a sensitivity of

$$\frac{d\kappa}{d\Theta} = -20.53\, rad^{-1} = -35.83\frac{\%}{deg}$$

(8.7)

is found in the middle of the slope at $\Theta = 11.2°$.

To determine if a signal is transmitted inside or outside the well defined area, a threshold value κ_{thres} can be introduced that evaluates the correlation maxima: if it is exceeded, the angle of radiation Θ is assumed to be inside, otherwise not. Based on equation (8.5), the detection angle Θ_{det} is calculated by

$$\sin(\Theta_{det}) = \frac{3.83\, c}{\pi\, a \left(2\, f_0 + \kappa_{thres}\, B\right)}.$$

(8.8)

As expected, the detection angle decreases with increasing transmitter diameter $2a$ and increasing signal frequency.

8.1.2 Implementation of a prototype

In the previous chapter the effect of the piston modeled transmitter to a linear chirp signal transmitted in arbitrary directions is shown and how the one bit correlation method can evaluate this effect. The new measurement system described in this thesis makes use of these "transmission angle coded"-signals and tries to identify the position of reflecting objects by the kind of the actually reflected signal. Therefore, in a first attempt a threshold level κ_{thres} is introduced that distinguishes between objects located inside or outside the detection area.

As in this case the signal coding is done by the piston modeled transmitter, the incoming signal must not be changed by the receiver, which requires a receiver with omni directional radiation pattern at least in the range of interest. This can be accomplished by using a small electret microphone.
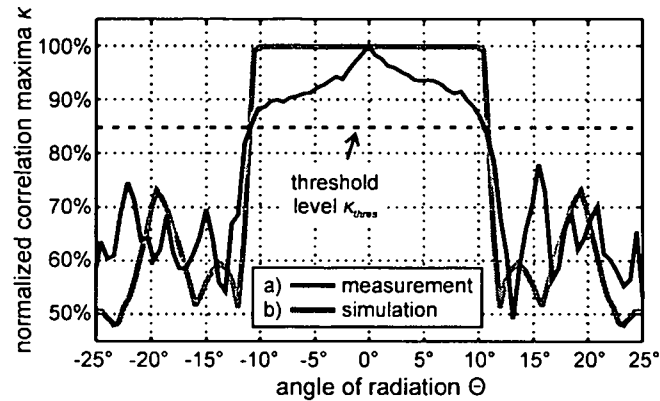
Figure 8.5: Simulation and measurements of correlation maxima depending on angle of radiation Θ

In Figure 8.5 the evaluated results are compared with measurements carried out by the prototype described in chapter 9. While good coincidence is found in the range of the slopes (at $\Theta \approx \pm 11°$), outside this range ($|\Theta| > 11°$) relatively strong deviations are visible. A possible reason of this effect is described in chapter 9.3.3.
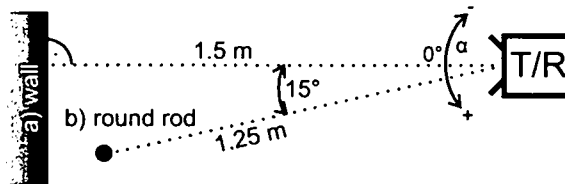
Figure 8.6: Measurement assembly to evaluate the well defined and objects independent detection area

The environment where measurements are taken is shown in Figure 8.6: the measurement device is mounted on a positioning system that carries out rotational scans of the environments, which consist of two objects: a) a smooth well aligned wall at a distance of 1.5 m and b) a round rod with a diameter of 16 mm at 1.25 m. These objects strongly differ according to their reflection characteristics; while the wall provides very strong echoes due to specular reflection, the round rod spreads the incoming signal in all directions leading to very low signal amplitudes.

During the measurement 5 scans in the range of $-30° \le \alpha \le 30°$ with an increment of $\Delta \alpha = 0.5°$ are taken. The reference signal used by the one bit correlation was learned (at position of direct alignment towards the wall) and the threshold level κ_{thres} evaluating the correlation maxima is set to $\kappa_{thres} = 85\ \%$ (see Figure 8.5).

According to Figure 8.7, both objects are detected in the same way independent of their (very different) reflection properties. The detection range is $\pm 10°$ in both cases and no fluctuations are found at the borders. The measurement results are located at the correct positions (compare Figure 8.5) and the distance to each object is evaluated correctly.

Compared with a conventional measurement method (see chapter 9.3.1) great progress is achieved. There it is hardly possible to detect this combination of objects at all, not to mention the clear borders and missing measurement fluctuations in this range.

The presented measurement results are based only on threshold detection of the correlation results by a fixed threshold value κ_{thres} and do not take into account the slope of the correlation maxima found at borders, which will lead to better robustness and even more reliable results. Also the design of an advanced transmitter providing better phase characteristics will enhance further developments.
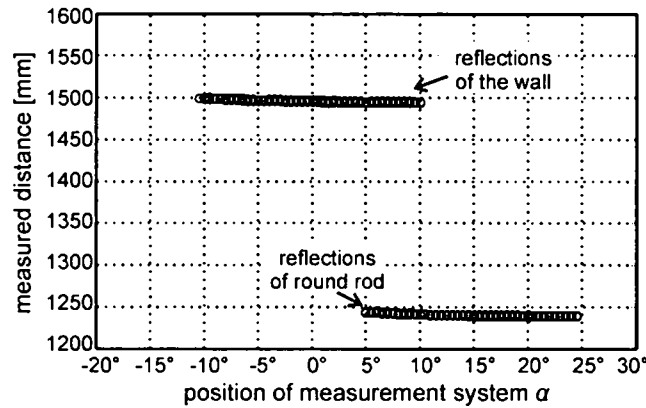
Figure 8.7: Measurements obtained by wall and round rod

8.2 Adjustment of detection area

The possibility of adjusting the detection area leads to significant advantages especially in the case of scanning systems (see chapter 5.3). The presented measurement method allows easy adjustment without additional measurement cycles and is able to provide a so called "soft scan" at the borders of the detection area.

8.2.1 Basic principle of adjustment

The basic approach is the modification of the reference pattern used by the one bit correlation. Consider Figure 8.3/c, where anti correlation is provided during its last (gray shaded) part if the full signal is evaluated by using a reference pattern of the full signal length T. If, for example, the reference pattern lasts only until t_z (assuming the modified reference length $T' = t_z$), the evaluated signal will not contain any anticorrelation parts. In case of a linear chirp with increasing frequency, truncation of the reference pattern means discarding higher frequency parts that would provide narrow main lobes. In the following, an evaluation of this method is given.

As mentioned before, the length of the reference pattern T is shortened to T' which is accomplished by the variation parameter V according to

$$T' = V\,T \text{ with } V \le 1.\tag{8.9}$$

Therefore, the end frequency f_{end} of the signal is changed to

$$f_{end} = f_{start} + \underbrace{V\,B}_{\substack{\text{modified signal}\\\text{bandwidth B'}}} = f_0 - \frac{B}{2}(1-2V).\tag{8.10}$$

This finally leads to a modification of the detection angle shown in equation (8.8) to

$$\sin\left(\Theta_{det}\right) = \frac{3.83\,c}{\pi\,a\left\{2\,f_0 + B\left[V\left(\kappa_{thres}+1\right)-1\right]\right\}}.\tag{8.11}$$

In Figure 8.8 the dependency of the detection angle Θ_{det} of the variation parameter V is shown ($V = 1$ means correlation with full reference). With decreasing value of the variation parameter V the length of the reference pattern and the signal bandwidth decreases which leads to increasing correlation results outside the area of good detection. In case of $V = 0.5$, the correlation results even exceeds the threshold level κ_{thres} e.g. at $\Theta = -22°$, which leads to decreasing robustness of the correlation method (see chapter 6.3.3) due to possible misinterpretations of the correlation maxima (see chapter 6.1). Therefore, the range of V must be restricted.
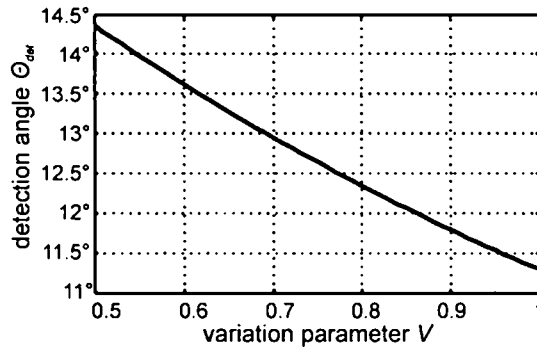
Figure 8.8: Detection angle Θ_{det} depending of variation parameter V

Setting the variation parameter V to a fixed value allows adjusting the detection area. In Figure 8.9 the correlation maxima are plotted over the angle of radiation in case of different variation parameters V: case a) shows uses the full reference pattern and is, therefore, equal to the results shown in Figure 8.5. With decreasing value of $V = 75\%$ and $V = 50\%$ the signal bandwidth decreases, which leads to increasing correlation maxima outside the angle of detection. To avoid erroneous results, further signal processing algorithms that are not in the scope of this work, are necessary.

At negative angles of radiation Θ good agreement with the derived values shown in Figure 8.8 is found; at positive angles some deviations are visible that are expected to occur due to fabrication tolerances of the used ultrasonic transmitter. It is necessary to mention that the

results shown in Figure 8.9 are based on the data obtained by only one scan; the three different results are derived by correlating the received data with three different reference patterns.

Adjustment of the detection area is useful to compensate e.g. the effect of the temperature dependent radiation pattern: according to equation (8.8) the detection angle Θ_{det} depends on the speed of sound c which strongly depends on the ambient temperature. Assuming a constant temperature in the measurement range, the variation parameter V can be used to compensate the temperature effect to get a temperature indifferent angle of detection Θ_{det}.
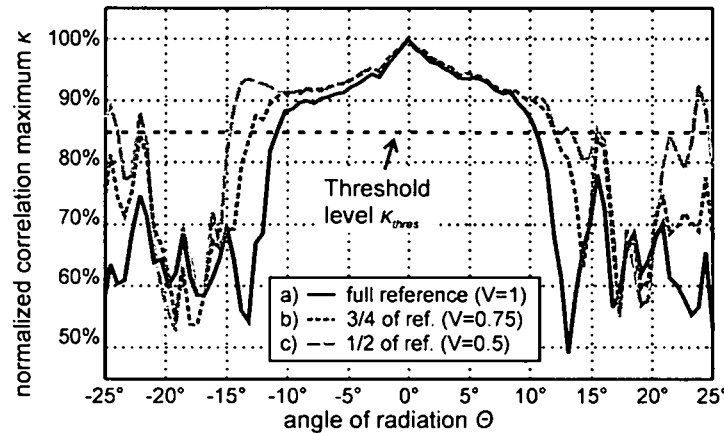
Figure 8.9: Correlation results obtained at different angles of radiation
at variation parameters of a) $V = 1$, b) $V = 0.75$ and c) $V = 0.5$

8.2.2 Implementation of "soft scan" algorithm

The aim of most scan based systems is the evaluation of the lateral position of an object. This can be achieved by seeking the "touch position", where an object enters respectively leaves the detection area during the scan process. Therefore, the sharpness of the detection area is a crucial parameter. The measurement method presented in this work basically fulfills this demand. Furthermore the so-called "soft scan" algorithm allows enhancing the resolution of scan based measurements beyond the size of incremental steps. In the following, a rotational scan with incremental steps of $\Delta\alpha$ is evaluated.

While in conventional systems the resolution is at least restricted to the step size $\Delta\alpha$, the possibility of adjusting the detection area as shown in the previous chapter allows enhancing the resolution. In Figure 8.10 a schematic of a measurement system providing a rotational scan (scan position α) is shown together with some crucial angles provided by the measurement system: depending on the signal parameters (bandwidth B and center frequency f_0) and the transmitter diameter $2a$, the angles of the zero points of the radiation pattern (between main and first side lobe) at the lowest frequency (Figure 8.10/a) and at the highest frequency (d) are found.

As the steep slope of the correlation result κ occurring at the border of detection (see Figure 8.4) is based on anticorrelation, and partial signal transmission through the first side lobe, the minimum and maximum angles of detection $\Theta_{det,min}$ (c) and $\Theta_{det,max}$ (b) are located in between. The actual angle of detection Θ_{det} is finally determined according to equation (8.11) by the

variation parameter V in the range $\Theta_{det,min} \leq \Theta_{det} \leq \Theta_{det,max}$. It is necessary to mention that this variation of the detection area (light gray area in Figure 8.10) depends only on the signal processing method in the receiver based on one sampled signal and, therefore, no additional measurement cycles are required. In the following a procedure is presented that allows finding the pointing angle towards an reflecting object with a resolution beyond the incremental steps of the scanning process.

a) lowest frequency
b) maximal adjust $\Theta_{det,max}$
c) minimal adjust $\Theta_{det,min}$
d) highest frequency
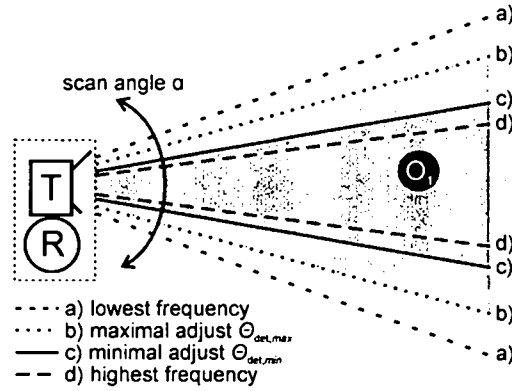
Figure 8.10: Schematic of scanning system with object O_l and crucial angles

At first consider an object located inside the minimum angle of detection $\Theta_{det,min}$ (dark shaded area in Figure 8.10). Due to the one bit correlation it is detected identically as long as it stays within this area. However, during the rotational scan once the object leaves this range and while it was detected at the scan position α_{n-1}, at $\alpha_n = \alpha_{n-1} + \Delta\alpha$ it is not detected any more. As long as the scan increment $\Delta\alpha$ is smaller than the adjustable range $\Delta\alpha < \Theta_{max} - \Theta_{min}$, the object is located inside the light gray area of adjustable range. Now the soft scan algorithm starts seeking a valid value of the variation parameter V in such a way that the relative correlation result $\kappa(V)$ equals the selected threshold value κ_{thres}. Finally the high resolution angle Θ between the sensor axis and the direction towards the object is calculated by equation (8.11).
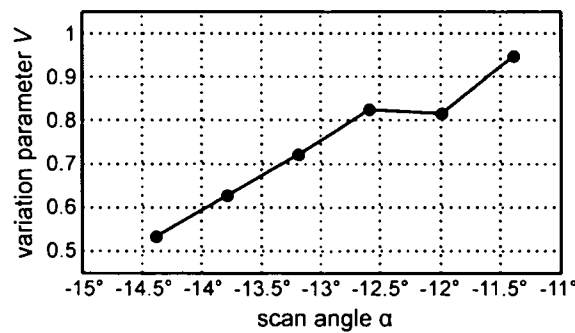
Figure 8.11: Evaluated variation parameter V
in the range of adjustable detection area

In the following, an example of the soft scan algorithm is presented: a scan is performed towards an object located at $\alpha = 0°$. Only the scan positions leading to detection angles inside the adjustable border of the measurement system $-14.5° < \alpha < -11°$ are evaluated. There, for

each measurement cycle the value of the variation parameter V is determined that leads to a relative correlation result of $\kappa = \kappa_{thres}$ (see Figure 8.11).

Based on these results the actual angle between the sensor axis and the direction to the object Θ is calculated. Finally, the position of the object with regard to the scanning system is calculated to

$$\beta = \alpha \pm \Theta. \tag{8.12}$$

The ambiguity of equation (8.12) occurs because the measurement system basically cannot determine on which side of the detection area the touching took place, however the evaluation of the scanning history allows determination of the valid sign. In this example the evaluation leads to the calculated object positions shown in Figure 8.12.

The position of the object with regard to the measurement system is found within accuracy below $\pm 0.5°$. This allows using incremental steps up to a range of $\Delta \alpha \approx 3°$, because the high resolution touching position is evaluated by the soft scan method with high accuracy based on only one measurement cycle located inside the range of adjustable detection area.
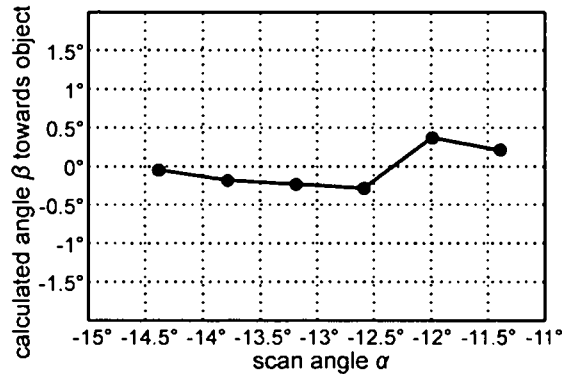
Figure 8.12: Calculated angle β between measurement system
and direction towards object

Of course this method is restricted to the accuracy of the radiation pattern of the used transmitter. The transmitter used in this work (see chapter 9) basically allows verifying the principle but is not suitable for real measurement systems as it provides too unsymmetrical radiation pattern that would lead to erroneous measurement results. This even becomes visible in Figure 8.9, where at negative angles good coincidence between calculation and measurements are found, while at positive angles the soft scan algorithm would not work properly as the correlation results do not respond properly to the variation parameter.

9 Experimental setup

In this chapter a prototype using the new measurement method is presented and the measurement setup is described. Finally some measurement tasks are shown.

9.1 Prototype using Polaroid-transducer

As mentioned in chapter 8, the new measurement method requires a transmitter and receiver with different radiation patterns (see chapter 8.1.2). Therefore, our prototype consists of an electrostatic transducer of the Polaroid series 600 type and a small electret microphone. Due to its large diameter with respect to the wavelength, the transmitter provides a distinctive piston-membrane like radiation pattern, while the small microphone can be considered to be omni-directional (at least in comparison to the used transmitter). As a consequence, phase shifts found at the received signals are mainly generated by the transmitter and can, therefore, be described by the model of the piston membrane (see chapter 7). In Figure 9.1 the prototype, consisting of the transmitter and receiver mounted side by side, is shown.
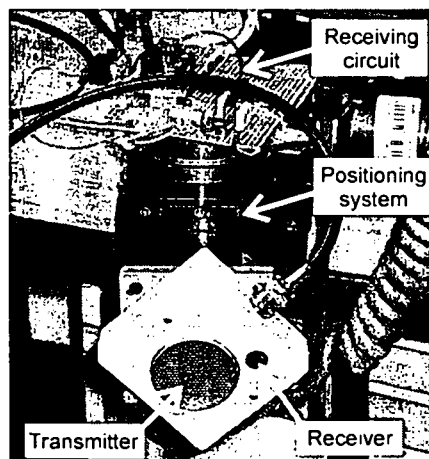
Figure 9.1: Prototype of measurement system containing of transmitter and receiver mounted on positioning system with receiving circuit

All measurement tasks shown in this thesis are carried out with this assembly. However, a real stand alone prototype was not designed yet and, therefore, the signal generation and amplification and the evaluation of the received signal is done by using laboratory equipments as described in the following.

9.2 Measurement assembly

The main part of the measurement assembly is a personal computer that runs MATLAB® and that is equipped with several interfaces. MATLAB® routines provide the following tasks:

- Initialization of measurement assembly

- Generation of transmission signals

- Controlling the positioning system

- Triggering of measurement cycle

- Readout of the received signal

- Evaluation of signal processing algorithms

- Visualization and storage of evaluated data

In Figure 9.2 a schematic of the measurement equipments is shown.
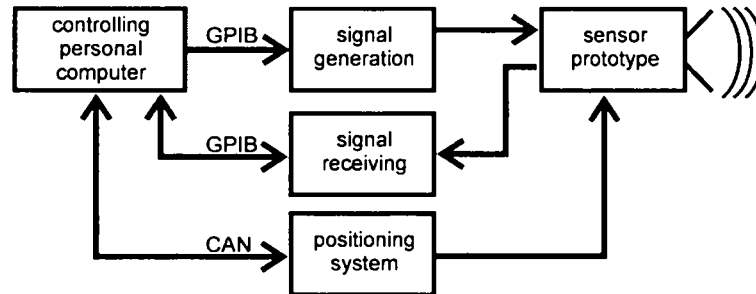
Figure 9.2: Components of measurement assembly

In the following chapters the components of the measurement assembly are described.

9.2.1 Signal generation

Pulse compression requires well defined transmission signals. In this work linear chirps are used. In the presented measurement assembly the transmission signal is designed by a personal computer running MATLAB®; afterwards this signal is transferred to an arbitrary waveform generator of the type "Agilent 33120A" (further information in [www2]), where it is stored as volatile waveform. The output of the signal generator is connected to a high voltage amplifier of the type "A-303" from "A.A.Lab Systems LTD" (see [www3]). Its main parameters are shown in Table 9.1.

This device allows directly connecting an electrostatic transmitter, which is in our case a "Polaroid series 600" type (see [www1]) providing an input capacity of about $C = 500\,pF$. In Figure 9.3 the maximum output voltages of the amplifier A-303 connected to electrostatic transmitters providing different capacities C are shown over the frequency.

The maximum voltage is basically restricted by the maximum output voltage U_{max} and the maximum frequency f_{max} of the amplifier (gray shaded area). Due to the frequency dependent

impedance of the electrostatic transducer, the maximum current I_{max} restricts the maximum achievable voltage (black lines) depending on the transducer capacity. In case of the used transmitter ($C = 500\,pF$), the maximum alternating voltage of $U_{alt} = 200\,V$ can be applied up to $f_{sig,max} = 300\,kHz$. The required bias voltage U_{bias} is generated by an additional DC voltage generator of the type "*SHQ 122M*" from "iseg Spezialelektronik GmbH" (see [www4]).

parameter		value
amplification	U_{out}/U_{in}	20 V/V
max. voltage	U_{max}	±200 V
max. current	I_{max}	±200 mA
max. frequency	f_{max}	1.2 MHz
max. slewrate	$slew_{max}$	400 V/μs

Table 9.1: Main parameters of high voltage amplifier A-303
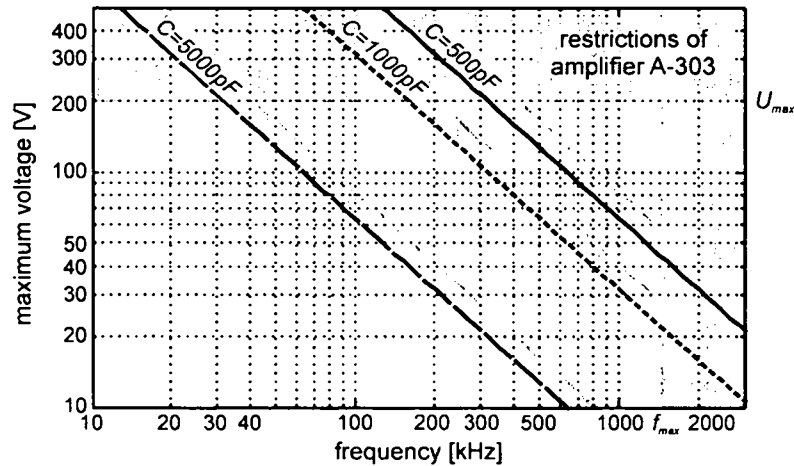

Figure 9.3: Possible output voltage range of amplifier A-303
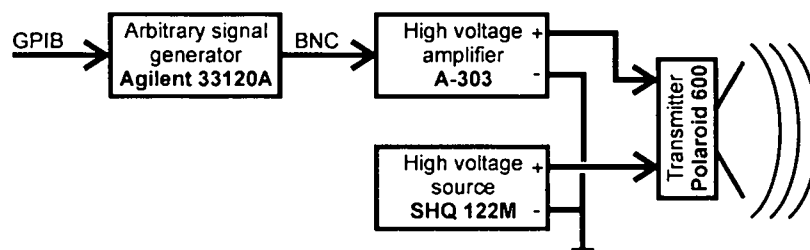in case of different transducer capacities

Figure 9.4: Schematic of signal generation

A schematic containing the mentioned devices is shown in Figure 9.4. In this case the high voltage source *SHQ 122M* delivers a negative voltage of $U_{out} = -U_{bias}$.

9.2.2 Positioning system

The transmitter is mounted on a positioning system of the type *"PowerCube"* from "Amtec GmbH" (see [www5]). It uses a wrist module *PW070* containing a pan and tilt axis. The system is connected to the controller PC by a CAN-bus. An ActiveX dynamic link library, containing the library delivered with the positioning system, allows a user friendly control of the system using easy MATLAB® commands. A schematic of the full measurement system and the used reference frames is shown in Figure 9.5.
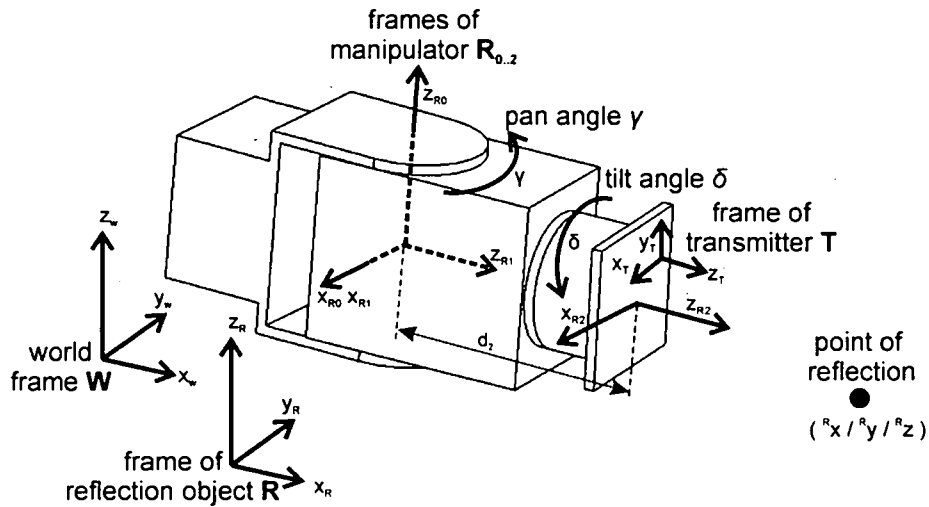
Figure 9.5: Geometric schematic of measurement assembly
containing geometric frames of the world W, the reflection object R,
the manipulator R$_{0.2}$ and the transmitter T

The modeling of the system uses the powerful principle of homogeneous transformations as described in [Pau81]: as shown in Figure 9.5, the model consists of several frames (frame of reflection object **R**, frames of manipulator **R$_{0..2}$** and frame of transmitter **T**) that are all located inside the world frame **W**. The PoR is defined by the vector $^R\mathbf{P_{refl}} = (^Rx \, / \, ^Ry \, / \, ^Rz)$ with regard to the frame of the reflection object **R**. Using homogeneous transformations this vector $^R\mathbf{P_{refl}}$ is easily transformed to $^W\mathbf{P_{refl}}$, which describes the position of the PoR with regard to the world frame **W**:

$$\underbrace{^W P_{refl}}_{\substack{\text{position with regard} \\ \text{to world frame W}}} = \underbrace{^W\mathbf{T_R}}_{\substack{\text{homogeneous} \\ \text{transformation} \\ \text{from R to W}}} \underbrace{^R P_{refl}}_{\substack{\text{position with regard} \\ \text{to frame R}}} \tag{8.13}$$

Homogeneous transformations can be a translation transformation in x, y and z direction, which leads to a transformation matrix of

$$\mathbf{transl}(x,y,z) = \begin{bmatrix} 1 & 0 & 0 & x \\ 0 & 1 & 0 & y \\ 0 & 0 & 1 & z \\ 0 & 0 & 0 & 1 \end{bmatrix}, \tag{8.14}$$

or rotational transformations about the x, y or z axes by an angle θ. In this case the transformation matrices are

$$\mathbf{rot}(x,\theta) = \begin{bmatrix} 1 & 0 & 0 & 0 \\ 0 & \cos(\theta) & -\sin(\theta) & 0 \\ 0 & \sin(\theta) & \cos(\theta) & 0 \\ 0 & 0 & 0 & 1 \end{bmatrix}, \tag{8.15}$$

$$\mathbf{rot}(y,\theta) = \begin{bmatrix} \cos(\theta) & 0 & \sin(\theta) & 0 \\ 0 & 1 & 0 & 0 \\ -\sin(\theta) & 0 & \cos(\theta) & 0 \\ 0 & 0 & 0 & 1 \end{bmatrix} \text{ and} \tag{8.16}$$

$$\mathbf{rot}(z,\theta) = \begin{bmatrix} \cos(\theta) & -\sin(\theta) & 0 & 0 \\ \sin(\theta) & \cos(\theta) & 0 & 0 \\ 0 & 0 & 1 & 0 \\ 0 & 0 & 0 & 1 \end{bmatrix}. \tag{8.17}$$

The final transformation matrix $^{W}\mathbf{T_R}$ consists of a combination of the previously shown transformations. Consider the example in Figure 9.6: it shows the geometric frame of the reflection object $\mathbf{R}$ located inside the world frame $\mathbf{W}$. It is turned by 90° around the z_w-axis and its origin $^{W}\mathbf{O_R}$ is shifted by the vector $(^{W}x_R / {}^{W}y_R / {}^{W}z_R)$. Let's assume an example of $^{W}\mathbf{O_R} = (-3 / 2 / 1)$.
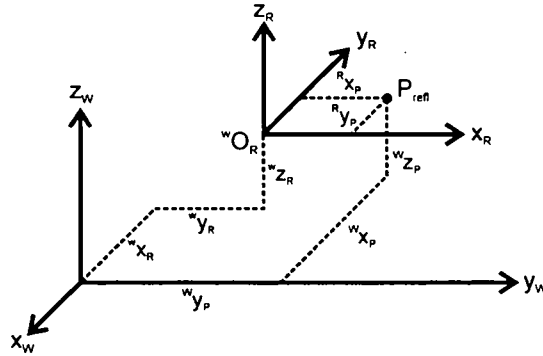

Figure 9.6: Example of homogeneous transformation

Therefore, the transformation matrix $^{W}\mathbf{T_R}$ is calculated using equations (8.14) and (8.17) to

$$^{W}\mathbf{T_R} = \mathbf{transl}(-3,2,1)\,\mathbf{rot}\left(z,\frac{\pi}{2}\right) = \begin{bmatrix} 0 & -1 & 0 & -3 \\ 1 & 0 & 0 & 2 \\ 0 & 0 & 1 & 1 \\ 0 & 0 & 0 & 1 \end{bmatrix}. \tag{8.18}$$

The position of the point $^R\mathbf{P_{refl}}$ is defined by the vector $(^Rx_P/^Ry_P/^Rz_P)$ with regard to the geometric frame $\mathbf{R}$. In the homogeneous coordinate representation an additional scale factor w is added to each vector. Therefore, a point vector

$$\mathbf{v} = a\,\mathbf{i} + b\,\mathbf{j} + c\,\mathbf{k} \qquad (8.19)$$

where $\mathbf{i}$, $\mathbf{j}$ and $\mathbf{k}$ are unit vectors along the x, y and z coordinate axes, is represented in homogeneous coordinates as column matrix

$$\mathbf{v} = \begin{bmatrix} x \\ y \\ z \\ w \end{bmatrix}, \qquad (8.20)$$

where

$$a = \frac{x}{w},\ b = \frac{y}{w} \text{ and } c = \frac{z}{w}. \qquad (8.21)$$

This allows distinguishing between vectors describing the position of points with regard to a geometric frame ($w \neq 0$ and mostly $w = 1$) that are effected by translational transformation. Vectors at infinity ($w = 0$) are used to describe directions and they are only effected by rotational transformations.

Assuming the position of the point $^R\mathbf{P_{refl}}$ of ($2 / 2 / 0$), its homogeneous coordinates are

$$^R\mathbf{P}_{refl} = \begin{bmatrix} 2 \\ 2 \\ 0 \\ 1 \end{bmatrix}. \qquad (8.22)$$

Together with equations (8.13) and (8.18), the position $^W\mathbf{P_{refl}}$ of the point with regard to the world coordinate system $\mathbf{W}$ is easily calculated to

$$^W\mathbf{P}_{refl} = \begin{bmatrix} 0 & -1 & 0 & -3 \\ 1 & 0 & 0 & 2 \\ 0 & 0 & 1 & 1 \\ 0 & 0 & 0 & 1 \end{bmatrix} \begin{bmatrix} 2 \\ 2 \\ 0 \\ 1 \end{bmatrix} = \begin{bmatrix} -5 \\ 4 \\ 1 \\ 1 \end{bmatrix}, \qquad (8.23)$$

which can be verified by Figure 9.6. The homogeneous transformation can also be used to transform coordinates from the world frame $\mathbf{W}$ to another frame by inverting the transformation matrix $\mathbf{T}$ which leads to

$$^W\mathbf{T_R}^{-1}\ ^W\mathbf{P}_{refl} = \underbrace{^W\mathbf{T_R}^{-1}\ ^W\mathbf{T_R}}_{1}\ ^R\mathbf{P}_{refl} = {}^R\mathbf{P}_{refl}. \qquad (8.24)$$

Basically the presented calculus allows describing the measurement assembly shown in Figure 9.5. In [Pau81] a systematic approach to describe manipulators consisting of links connected

together by actuated joints is presented by introducing **A** matrices. The final transformation matrix $\mathbf{T_N}$ found after N links is found to

$$\mathbf{T}_N = \mathbf{A}_1 \, \mathbf{A}_2 \dots \mathbf{A}_N \qquad (8.25)$$

This method requires assigning well defined coordinate frames to all links of the manipulator (frames $\mathbf{R}_1$ and $\mathbf{R}_2$ in Figure 9.5). Afterwards the **A** matrices describe the relationship between two successive frames $\mathbf{R_{n-1}}$ and $\mathbf{R_n}$ by the following consecutive rotations and translations:

1. rotate about z_{n-1} at an angle θ_n

2. translate along z_{n-1} a distance d_n

3. translate along rotated $x_{n-1} = x_n$ a length a_n

4. rotate about x_n at the twist angle α_n

After evaluation of these parameters, the transformation matrix $\mathbf{A}_n$ valid for each link is determined to

$$\mathbf{A}_n = \begin{bmatrix} \cos\theta_n & -\sin\theta_n\cos\alpha_n & \sin\theta_n\sin\alpha_n & a_n\cos\theta_n \\ \sin\theta_n & \cos\theta_n\cos\alpha_n & -\cos\theta_n\sin\alpha_n & a_n\sin\theta_n \\ 0 & \sin\alpha_n & \cos\alpha_n & d_n \\ 0 & 0 & 0 & 1 \end{bmatrix}. \qquad (8.26)$$

The system shown in Figure 9.5 provides the following parameters

link number	twist angle θ_n	d_n	a_n	α_n
1	pan angle γ	0	0	-90°
2	tilt angle δ	d_2	0	0°

Table 9.2: Parameters of positioning system to derive A matrices

Based on equations (8.25) and (8.26), the transmission matrix $^{R0}\mathbf{T}_{R2}$ to transform coordinates of the geometric frame at the end of the manipulator $\mathbf{R}_2$ to the basis geometric frame $\mathbf{R}_0$ is calculated.

Coordinates of the transmitter frame $\mathbf{T}$ are transformed by $^{R2}\mathbf{T}_T$ to the geometric frame $\mathbf{R}_2$ at the end of the manipulator and finally the full transformation chain from the transmitter frame $\mathbf{T}$ to the world frame $\mathbf{W}$ is given to

$$^{W}\mathbf{T}_T = \underbrace{\mathbf{T}_{R_0}}_{\substack{\text{manipulator base} \\ \text{to world frame}}} \underbrace{\mathbf{T}_{R_2}}_{\substack{\text{manipulator} \\ \text{transformation}}} \underbrace{\mathbf{T}_T}_{\substack{\text{transmitter} \\ \text{transformation}}} . \qquad (8.27)$$

In most cases the relative position between the ultrasonic transmitter, mounted in the origin of the transmitter frame $\mathbf{T}$, and the reflecting point $\mathbf{P}_{refl}$ is of interest. As equations (8.13) and

(8.27) are both related to the world frame **W** a direct evaluation of the requested vector $^T P_{refl}$, the position of a reflection point with regard to the transducer frame **T** is possible:

$$^T\mathbf{P}_{refl} = \mathbf{T}_T^{-1}\ \mathbf{T}_{R_2}^{-1}\ \mathbf{T}_{R_0}^{-1}\ \mathbf{T}_R\ {}^R\mathbf{P}_{refl}\ . \tag{8.28}$$

To evaluate for example the well defined detection area, the angle of radiation Θ between the sensor axis z_T and the direction towards the PoR $\mathbf{P}_{refl}$ is considered. After calculation of equation (8.28) the requested angle Θ is directly calculated to

$$\Theta = \arccos\left(\frac{^T\mathbf{P}_{refl}\bullet\mathbf{z}_T}{\left|^T\mathbf{P}_{refl}\right|\underbrace{\left|\mathbf{z}_T\right|}_{1}}\right) = \arccos\left(\frac{^T\mathbf{P}_{refl}}{\left|^T\mathbf{P}_{refl}\right|}\bullet\mathbf{z}_T\right) \tag{8.29}$$

In the following some results based on the previous calculations, are shown: the manipulator basis frame $\mathbf{R}_0$, as well as the frame of the reflection object $\mathbf{R}$ are located in the origin of the world frame **W**. To get the conditions as shown in Figure 9.5, the basis frame $\mathbf{R}_0$ is rotated at about an angle of $-90°$ around the z-axis. The distance between the pan-axis and the origin of the transmitter frame (assuming also $\mathbf{T} = \mathbf{R}_2$) is given to $d_2 = 150\ mm$. The reflection point $\mathbf{P}_{refl}$ is located at several positions and the angle of transmission Θ is evaluated during a scan using the pan-axis y of the manipulator.
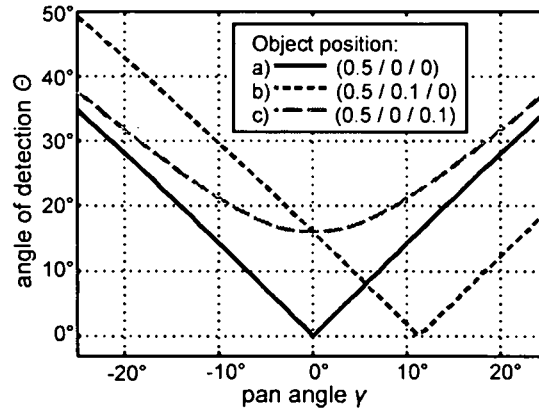
Figure 9.7: Angle of detection Θ over pan angle y
depending on position of the point of reflection

In case a) the PoR is located directly in front of the transmitter, therefore, at $y = 0$ the angle of detection is $\Theta = 0°$, too. However, due to the offset $d_2 = 0.150\ mm$, y is not equal to Θ in general. In case b) of a lateral offset in the plane of panning, a similar result is expected that is only shifted by a constant angle (transducer is well aligned to the PoR at about $y = 11.5°$). However, if the PoR is outside the plane of panning, the angle of detection can never reach $\Theta = 0$ (see Figure 9.7/c). These effects must be accounted for in case of measurement tasks to get correct results.

9.2.3 Signal receiver

In this work two main kinds of signal receiving are used depending on the aspect of the measurement: while basic measurements require a calibrated microphone with well defined properties, the prototype of the final system needs a small and cheap solution. In the following the two used signal receiving components are presented.

9.2.3.1 Calibrated measurement system

To get valid information about the sound pressure generated by the ultrasonic transmitter, a calibrated electrostatic microphone of the type "4138" from "Brüel&Kjaer®" [www6] is used. It provides a calibrated frequency response in the range from 6.5 Hz to 140 kHz and, therefore, is useful for ultrasonic measurements. As any other electrostatic microphone also this type requires a high bias voltage of $U_{bias} = 200\ V$. This is provided by the "Nexus Conditioning Amplifier" also from Brüel&Kjaer®. This device supports up to four microphones of different types and further provides signal conditioning as filtering and amplification. Finally, the conditioned and amplified signal is provided at a BNC-connector which can be directly connected to a digital sampling oscilloscope or other measurement devices.

9.2.3.2 Electret microphone

As the final system costs must be considered, it is not possible to use a calibrated measurement system as described above in the final device. As mentioned in chapter 8, the main demand with respect to the receiver is a sufficiently different radiation pattern with regard to the transmitter. In this thesis a receiver providing a preferable wide radiation pattern is used. Wide radiation patterns are achieved generally by small microphones and in our case a microphone of the type "MCE-2000" from Panasonic is used.

The principle of the electret microphone is similar to an electrostatic microphone, but the necessary bias voltage is replaced by a special electret film that provides the required electrostatic field without additional bias voltages. Furthermore, the device contains a built in FET (Field Effect Transistor) that changes the impedance from the very high value of the membrane to an output impedance of $R_{out} = 3.8\ k\Omega$ which dramatically simplifies the receiver circuit.

According to the datasheet of the device it shows a sensitivity of about $6\ mV/Pa$ in the frequency range of $20\ Hz \leq f \leq 20\ kHz$, which is basically not suitable for ultrasonic measurements. However, at higher frequencies it delivers constant sensitivity decay of $-20\ dB/dec$. This allows using an amplifier compensating this effect by proper frequency dependent amplification.

9.2.4 Signal processing

After receiving, the signal is sampled by a digital sampling oscilloscope of the type "HP54542C" from Agilent (formerly Hewlett Packard). While the necessary bandwidth and sampling rate are achieved by most devices, the critical parameter is the available record length, which is determined by the sampling rate and the expected measurement range. Assuming a measurement distance of $L_{dist} = 3\ m$, a total measurement range of $L_{range} = 2\ L_{dist} = 6\ m$ must be evaluated due to the passive reflection topology. This leads to a maximum record length of

about $T_{range} \approx 20\ ms$ which results, in case of a sampling rate of $f_{sample} = 1\ MHz$, to a required memory depth of $N_{mem,min} = 20\ kSample$. The used DSO provides a maximum depth of $N_{mem,max} = 32\ kSample$ and is, therefore, suitable for this task.

To get almost jitter free results, the oscilloscope is triggered by the sync output of the arbitrary signal generator, which itself is triggered by the controlling personal computer transmitting a trigger-command through the GPIB-bus. After sampling is finished, the data is transferred to the personal computer through the same connection. There it is evaluated by MATLAB® routines. This method allows evaluation of analog signals as well as digital evaluation as required during the one bit correlation.

9.3 Measurement tasks

9.3.1 Evaluation of conventional burst detection method

Most ultrasonic distance measurement systems are based on ToF measurement of burst signals. Mono frequent bursts are easy to generate and require only small bandwidth transducers as piezo-electric types are. Signal detection is accomplished by introducing a threshold value and a signal is considered to be received whenever this threshold is exceeded. A simulation of two received bursts with different amplitudes is plotted in Figure 9.8. Consider Figure 9.8/a providing large amplitude: in this case the time of detection is found near the start of the signal ($t = 0$) providing a small time offset Δt. This offset primarily does not cause problems if it remains constant which allows compensation of this value. However, in case of changing signal amplitudes, also the time of detection varies.
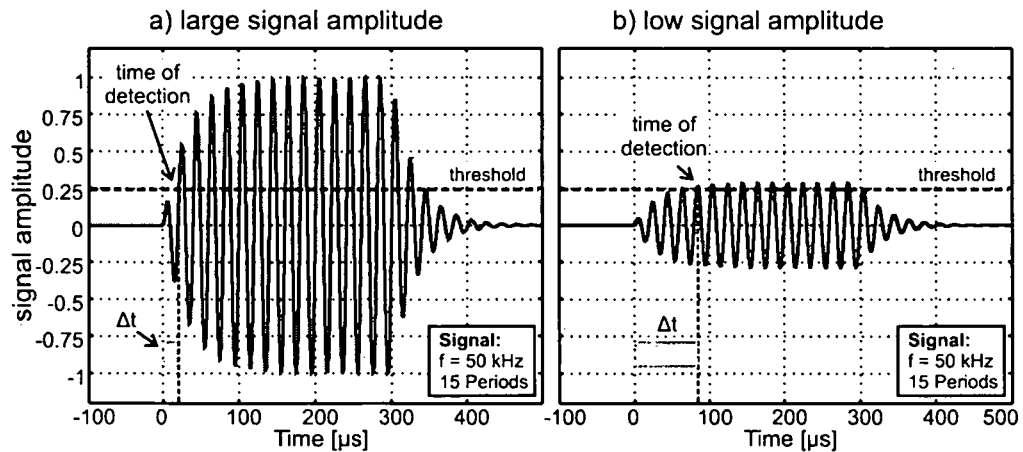
Figure 9.8: Detection of burst with different amplitudes

As long as the time of detection remains at the same signal period, the point of detection varies up to a quarter of a wavelength, in case of a signal frequency of $f = 50\ kHz$ measurement errors up to about $\Delta x = 0.85\ mm$ (assuming a two way measurement system) are expected. While this is not as bad, further amplitude changes cause a change of the detection period thus resulting in a measurement error Δx of about one wavelength which is about $\Delta x = 3.4\ mm$ in the case shown. As shown in Figure 9.8/b the measurement error can also become much worse. This

problem increases with decreasing transducer bandwidth as the signal envelopes incline more gently leading to increasing uncertainties in the time of detection.

In the following the results of some measurements are presented that show the mentioned effects: a rotational scan is provided towards two different objects, a smooth wall with good reflection properties and a round rod with a diameter of *16 mm* thus providing only weak reflections (see Figure 9.9). The used ultrasonic transducer is an electrostatic Polaroid series 600 type and its signals firstly generated by an arbitrary waveform generator and secondly amplified by a high voltage amplified *A-303*. The reflected signal is received by another transducer of the same type and after amplification it is sampled by a digital oscilloscope and evaluated in a personal computer that runs MATLAB®.
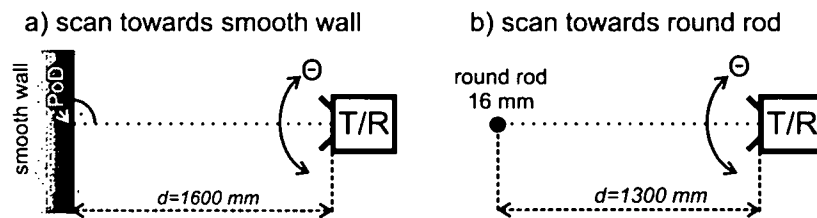

Figure 9.9: Measurement assembly for scans towards a) plane wall and b) round rod

At first a scan towards a smooth wall is carried out: in case of direct alignment a maximum signal voltage of $U_{max,wall} = 2.35 \ V$ is measured at the receiver circuit and, therefore, a threshold value of $U_{thres,wall} = 0.235 \ V$ is chosen. In Figure 9.10 the measured distances occurring during the scan are plotted: while at low angles $-5° \leq \Theta \leq 5°$ the measurements take place on the same period leading to small fluctuations only, at slightly higher angles the next period is detected resulting in a measurement error of about one wavelength $\Delta x \approx 3.4 \ mm$ (compare zoomed area in Figure 9.10).
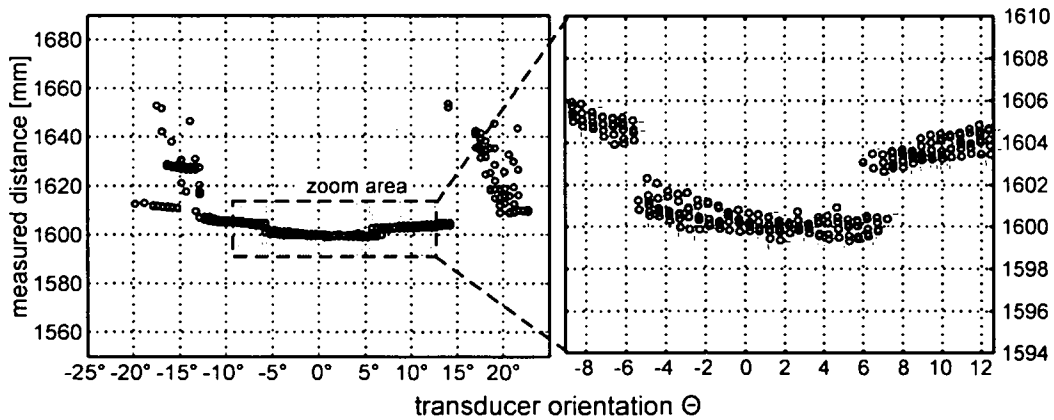
Figure 9.10: Measurement results of scan towards smooth wall over transducer orientation Θ

At higher angles (e.g. in the range of $14° \leq \Theta \leq 16°$) the object is partially not detected because it is located in direction of the zero between the main lobe and the first side lobe of the radiation pattern (compare chapter 7). However, due to the good reflection properties afterwards it is detected again through the first side lobe, but large measurement uncertainties in the range up to about *50 mm* are expected there.

The second scan is carried out towards a round rod with a diameter of *16 mm* thus providing weak reflection properties because the signal is spread in several directions. Therfore, in case of direct alignment a maximum voltage of only $U_{max,rod} = 200\ mV$ is found, which is even below the threshold voltage $U_{thres,wall}$ of the previous measurement. To achieve measurement results the receiver threshold is set to $U_{thres,rod} = 100\ mV$. The retrieved measurement results are shown in Figure 9.11: the rod is detected in a range of $-8° \leq \Theta \leq 8°$ but provides large measurement fluctuations at the borders. As the threshold is at *50 %* of the maximum amplitude $U_{max,rod}$, the amplitudes received through the first side lobe are below the threshold voltage $U_{thres,rod}$. According to Table 7.1 the amplitude of the first side lobe is *17 dB* lower than the main lobe which is about *14 %* of the maximum.
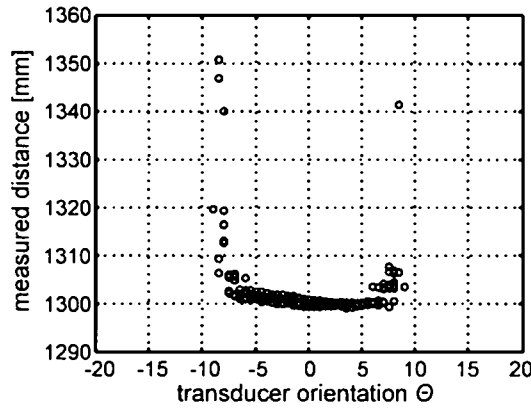

Figure 9.11: Measurement results of scan towards round rod
with diameter of *16 mm* over transducer orientation Θ

The presented measurements are carried out separately using individual threshold voltages $U_{thres,wall}$ and $U_{thres,rodl}$. Also in this case the different relative threshold amplitudes (*10 %* and *50 %*, respectively) lead to significantly different detection areas (wall in the range of about *44°* and rod of about *16°*). However, in case of measurements towards arbitrary objects without a priori knowledge of the reflection properties, threshold adjustment is hardly possible leading to strongly fluctuating measurement ranges: if the plane is scanned using the threshold voltage of the rod $U_{thres,rod}$, which is about *27 dB* below the maximum value obtained in direct alignment $U_{max,wall}$, also the second side lobe will be detected leading to an even increased total detection angle exceeding *60°*.

9.3.2 Evaluation of real transducer characteristics

In the following the behavior of a real transmitter (electrostatic Polaroid transmitter series 600 from Polaroid) is compared with the previously derived results and occurring deviations are discussed. The transmitter is evaluated separately according to its amplitude and phase behavior.

9.3.2.1 Measurement of amplitude behavior

The measurements are taken by the measurement assembly presented in chapter 9.2. Basically the frequency dependency of the amplitude is evaluated at different transducer orientations.

Therefore, a calibrated microphone is located at several positions in front of the transducer measuring the transmitted signal at 450 different angles of transmission in the range of $-50° \leq \Theta \leq 50°$. The frequency response in the frequency range of $20\,kHz \leq f \leq 100\,kHz$ is evaluated in each position. In Figure 9.12 the measured results are shown using a 3D-diagram: on the x-axis the actual signal frequency f is plotted while the y-axis shows the angle of radiation. The intensity of each pixel represents the signal amplitude at the corresponding pair of frequency f and angle of radiation Θ. This figure shows the effect of the frequency dependent main- and side lobes very well: while on the left side a wide main lobe is shown (zeros occur at about $|\Theta| = 25°$, on the right side a rather small main lobe with a width below $|\Theta| = 10°$ is visible.
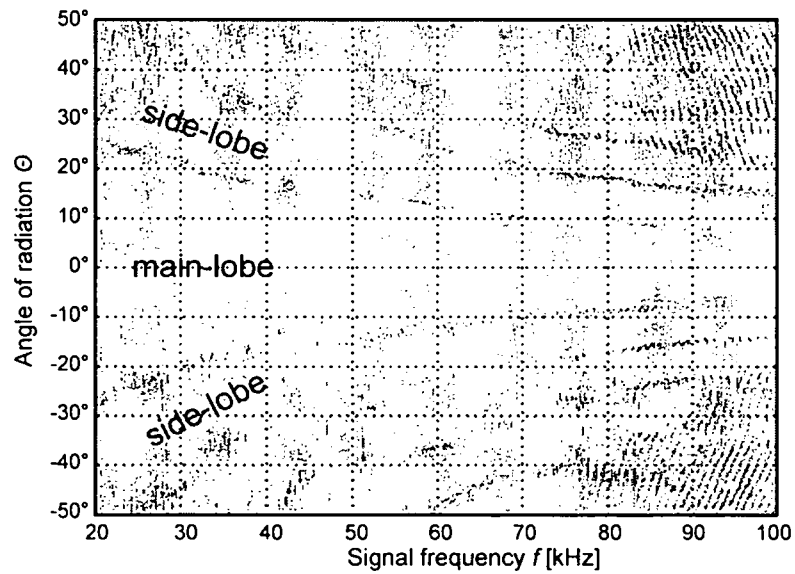

Figure 9.12: Signal amplitude depending on angle of radiation Θ and signal frequency f

For extended evaluation, horizontal and vertical cuts are necessary to show the amplitudes in this section. In Figure 9.13 the frequency dependent amplitude characteristic of a transmitter that is directly aligned towards the receiver is shown. In this case a horizontal cut at an angle of transmission of $\Theta = 0°$ was carried out. It allows evaluating a valid frequency range possible to transmit with this kind of transmitter.

To discuss the model of the piston membrane, vertical cuts are useful that provide the amplitude characteristic at one specific frequency depending on the transmitter orientation Θ. In Figure 9.14 measurement results obtained at different angles of transmission Θ and a fixed signal frequency $f = 35\,kHz$ are plotted together with the simulation results obtained by a piston modeled transducer with a diameter of $d = 38\,mm$. This plot shows very good coincidence between measurement and simulation in the range of the main lobe and also in parts of the side lobes. Although some deviations according to the signal amplitudes are partly visible, the zero directions between the lobes are perfectly coinciding.

At higher frequencies (for example at $f = 75\,kHz$ shown in Figure 9.15) the model does not match as well: in case a) of Figure 9.15 the simulation shows strong deviations (especially according to the positions of the zero points) from the measurement results. Changing the

diameter of the transducer model from the previous value of $d_1 = 38$ mm to $d_2 = 33$ mm leads to much better results (see case b).
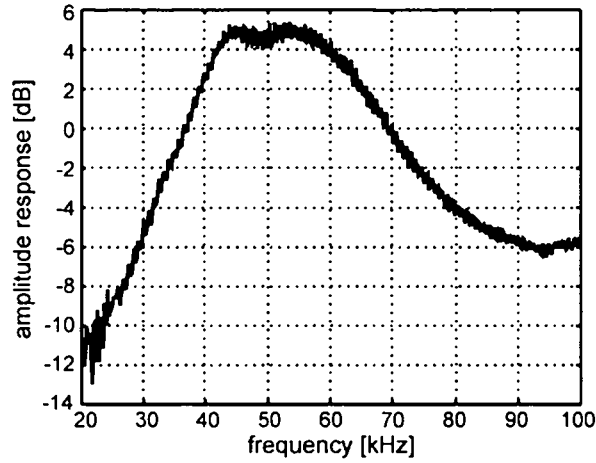
Figure 9.13: Frequency dependent amplitude characteristic
in case of direct alignment of the transmitter towards the receiver ($\Theta = 0°$).
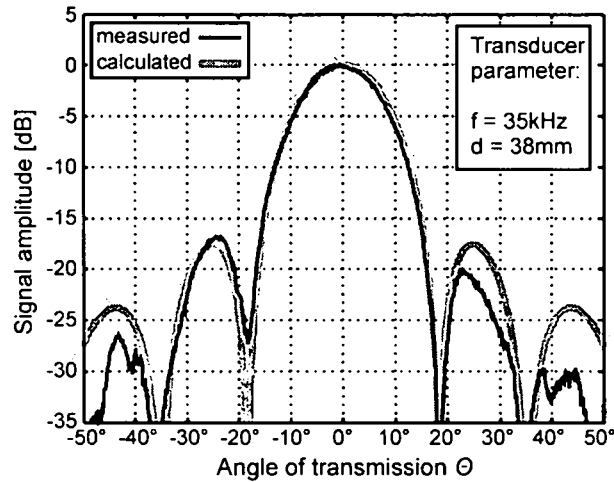
Figure 9.14: Amplitude characteristic over angle of transmission Θ of signal $f = 35$ kHz
and simulation results of transducer with diameter $d = 38$ mm

This leads to the assumption that the real transducer provides a frequency dependent behavior which depends on the actually transmitted signal. Fitting the transducer diameter to each measured frequency leads to Figure 9.16 which provides the appropriate effective transducer diameter d valid for each signal frequency f.

On attempt to explain this behavior is to take into account the stiffness of the membrane. This would be true if the membrane was fixed only at the circumference of the transducer. This would lead to different axial motions of the membrane depending on the stiffness of the membrane and the actual frequency. However, as the air-gap and the membrane thickness must be very small, this method is not practical.
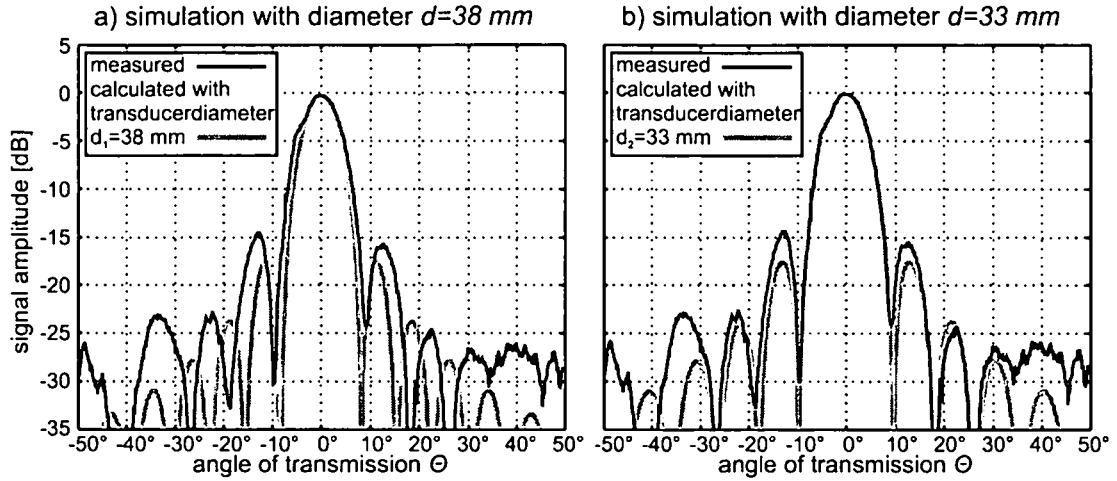
Figure 9.15: Comparison of Amplitude characteristics of measurement results with simulation results of transducer diameters a) $d_1 = 38$ mm and b) $d_2 = 33$ mm of signal $f = 75$ kHz over angle of transmission Θ
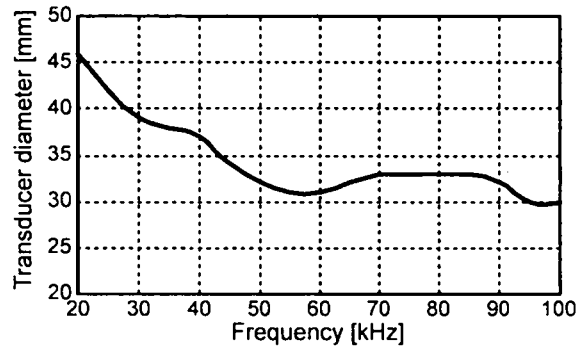
Figure 9.16: Effective transducer diameter d occurring at different signal frequencies f

As shown in [Mat95], the transducer is built of a grooved back plate with an attached isolated thin membrane (see Figure 9.17). The bias voltage U_{bias} leads to a bias tension of the membrane in between the fixed points and additional alternating voltages finally produce small vibrating areas. The influences of the membrane stiffness and the size of the gaps to the achievable signal amplitude, sensitivity and resonance frequency are described in detail in [Mat95] and [Raf91].
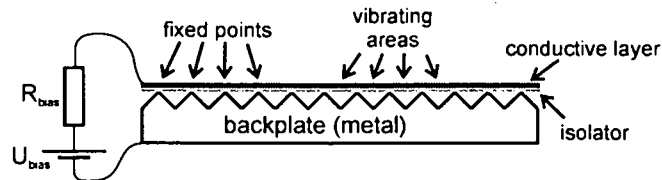
Figure 9.17: Schematic of electrostatic transducer according to [Mat95]

As the vibrating areas are much smaller than the wavelength, this assembly can be well described with the model of a piston membrane. However, it does not explain the frequency dependent change of the effective transducer diameter.

9.3.2.2 Measurement of phase behavior

Because of the fluctuating speed of sound in air direct phase measurement (that means direct comparison between transmitted and received signal) is hardly possible. Reasons are the occurring air turbulences due to moving objects or temperature changes. Phase measurement requires high measurement resolution: to achieve a phase resolution of $\Delta\varphi = 1°$ at a signal frequency of $f = 80\,kHz$, a time resolution of about $\Delta t = 34\,ns$ is necessary. In case of a measurement distance of $x_{dist} = 0.5\,m$ this requires variations of the speed of sound less than $20\,ppm$ during the measurement time which can be hardly accomplished. The solution provided in the following tries to minimize the whole measurement time and, therefore, to suppress occurring deviations: a special signal is generated that consists of a reference and a measurement part, between which the phase is measured. In Figure 9.18 the used signal is plotted: it consists of a reference signal s_{ref} with fixed frequency f_{ref} and length T_{ref} and of a measurement signal s_{meas} whose frequency f_{meas} is varied at each measurement. If a frequency dependent phase shift takes place, the original distance between the two signals

$$\Delta T_{orig} = t_2 - t_1 = T_{delay} + T_{meas} \qquad (8.30)$$

depends on the distance ΔT_{recv} evaluated at the receiver

$$\Delta T_{recv} = t_{2,recv} - t_{1,recv} = \Delta T_{orig} + T_{phase} \qquad (8.31)$$

according to the occurring phaseshift.
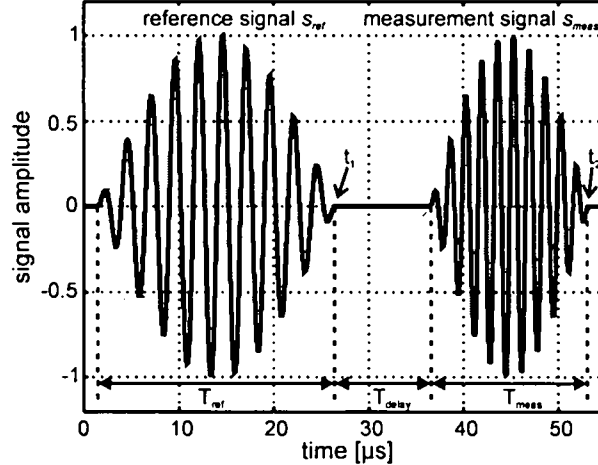
Figure 9.18: Combined signal for phase measurement consisting of reference signal s_{ref} and measurement signal s_{meas}

Therefore, the phase shift φ_{meas} (in degrees) of signal s_{meas} with regard to the reference signal s_{ref} is calculated by

$$\varphi_{meas} = 360° \, f_{meas} \, T_{phase} = 360° \, f_{meas} \left(t_{2,recv} - t_{1,recv} - T_{delay} - T_{meas} \right). \qquad (8.32)$$

As mentioned before, phase measurement requires a high measurement resolution. Therefore, the received signal is correlated with both the reference signal s_{ref} and the measurement signal s_{meas}. In Figure 9.19 the results obtained by each correlation process are shown. Due to the small

bandwidth of the used bursts the amplitudes of the correlation maxima occurring at the end of each signal t_1 and t_2 are very similar to the amplitudes of the relative maxima in their vicinities.

These are located at distinctive locations t_k according to the signal frequency f. In case of the measurement signal s_{meas} the maxima in vicinity $t_{2,k}$ are found at

$$t_{2,k} = t_2 + k \frac{1}{f_{meas}} \qquad (8.33)$$

with integer values of k and $k \neq 0$. This leads to the following general phase shift term $T_{phase,gen}$:

$$T_{phase,gen} = t_2 + \frac{k_{meas}}{f_{meas}} - t_1 - \frac{k_{ref}}{f_{ref}} - T_{delay} - T_{meas} \qquad (8.34)$$

Fortunately the correlation maximum of the reference signal is clearly detectable which allows setting k_{ref} in equation (8.34) to zero. The remaining value k_{meas} is then determined by giving the resulting phase shift φ_{meas} a valid limit of $-180° \leq \varphi_{meas} \leq 180°$.

The measurement resolution is restricted by the resolution of the position of the two signals. The following measurement results are based on a sampling rate of $f_{sample} = 10\ MHz$, which leads to a phase resolution in the range of $1.44° \leq \varphi_{meas} \leq 2.88°$ depending on the actual signal frequency $40\ kHz \leq \varphi_{meas} \leq 80\ kHz$ (according to equation (8.32)).
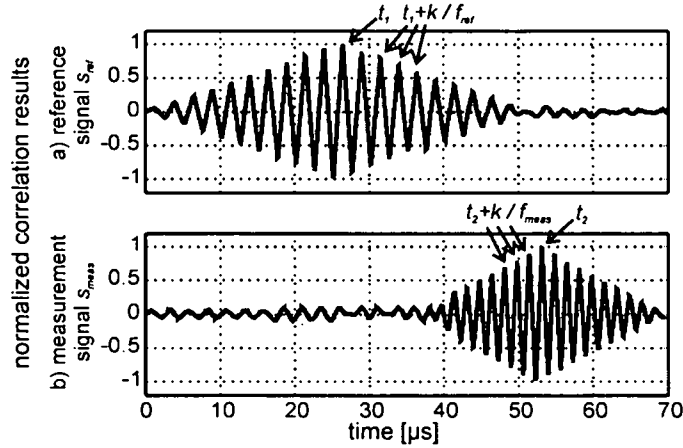
Figure 9.19: Correlation results obtained for reference signal s_{ref} and measurement signal s_{meas}

Measurements are taken at angles of transmission Θ in the range of $-15° \leq \Theta \leq 15°$ and at frequencies in the range of $44\ kHz \leq \varphi_{meas} \leq 80\ kHz$. The frequency of the reference signal s_{ref} is set to $f_{ref} = 40\ kHz$. In Figure 9.20 the results of the measurements are plotted as 3D-surface: on the horizontal axis the signal frequency f_{meas} and the angle of transmission Θ are found and at each point the height of the surface is given by the evaluated phase shift φ_{meas}.

In general, a relative good coincidence with the theoretically derived values ($0°$ for the main lobe and $180°$ at the first side lobe) are found. However, there are some deviations to mention: while the simulation expects no phase shift across the main lobe, the real transducer provides some phase shifts in the range of about $-30° \leq \varphi_{meas} \leq 30°$. This effect leads to reduced

correlation results if the reference pattern of the matched filter is directly matched to the filter that generates the exciting signal for the transmitter, because the transmitter itself provides an additional phase shift slightly altering the effectively transmitted signal. One solution to reduce this problem is using signals from reference measurements as reference pattern that already contain the occurring phase shift.
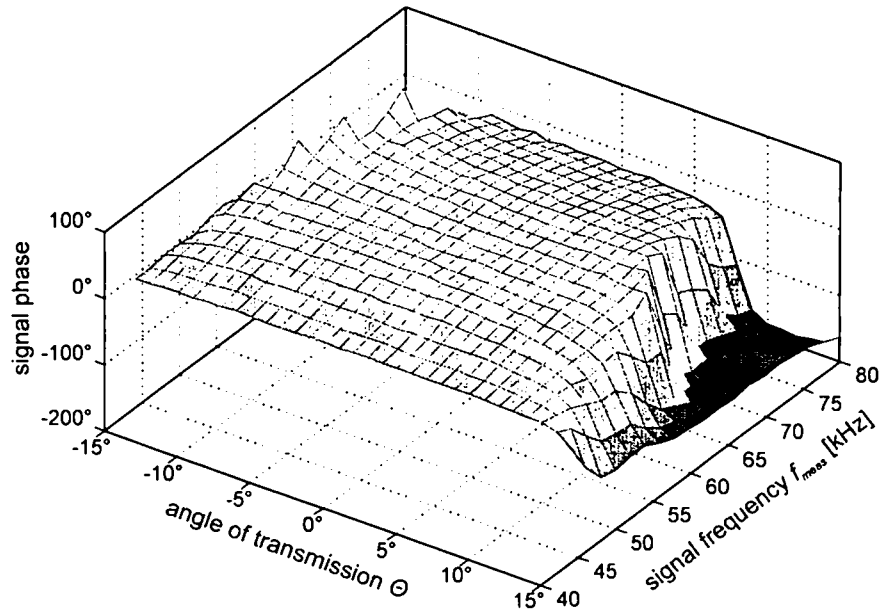
Figure 9.20: Measured signal phase depending on signal frequency f_{meas}
and angle of transmission Θ
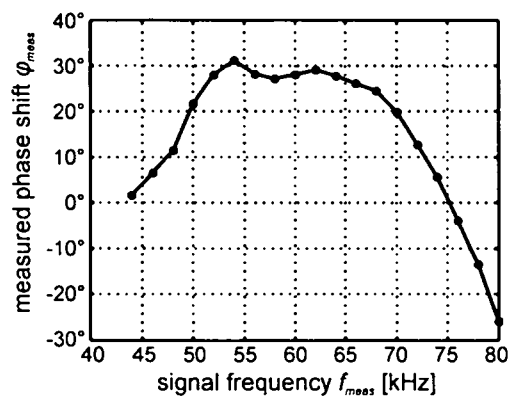
Figure 9.21: Measured signal phase φ_{meas} at fixed transmission angle $\Theta = 0°$
depending on signal frequency of f_{meas}

To verify the influence of the piston modeled transducer on the phase shift of the transmitted signal, the measured phase shift is plotted over the actual angle of transmission Θ at a fixed frequency $f_{meas} = 70\ kHz$ in Figure 9.22. The evaluated results are similar to the results obtained by simulation (gray line): at positive angles of transmission a very good coincidence is found

across the main lobe, the value of $-180°$ is not reached as well at the first side lobe. At negative angles an increasing phase shift is visible at the "edge" of the main lobe.
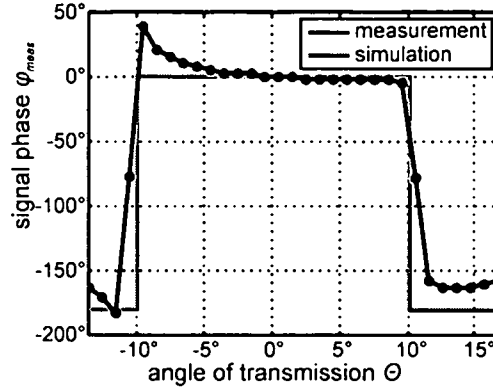
Figure 9.22: Measured signal phase φ_{meas} at fixed signal frequency $f_{meas} = 70\ kHz$ depending on angle of transmission Θ

The observed deviations are due to manufacturing tolerances of the evaluated transducer. This type is primarily not intended for this kind of measurements, but rather for distance measurements in transducer axis using the conventional burst method. Therefore the focus of this construction is rather laid on the device costs, than on the phase behavior outside the primary range of detection.
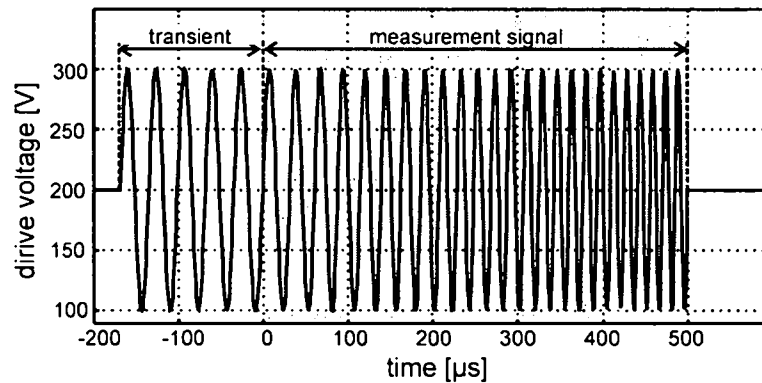
Figure 9.23: Drive voltage of the transmitter

9.3.3 Evaluation of reference signals used by one bit correlation

The pulse compression system is based on matched filtering of the received signal with a special filter (see chapter 6.1). In case of one bit correlation this matched filter is realized as bitwise comparison of two bit streams (received bit stream and stored one), which is evaluated after each sampling time (see chapter 6.2). In the following, the generation of this reference bit stream is discussed.

The basic approach is to take the digitized form of the exceeding voltage of the transmitter containing the measurement signal which is shown shaded gray in Figure 9.23. In this case the full transmission signal consists of a transient of five periods of the start frequency and a linear

chirp as measurement signal. Its parameters are: length $L = 500\ \mu s$, center frequency $f_0 = 50\ kHz$ and bandwidth $B = 40\ kHz$ ($B_{rel} = 80\ \%$).

The expected digital correlation result in case of an undisturbed received signal is shown in Figure 9.24. In this evaluation a sampling frequency of $f_{sample} = 5\ MHz$ is chosen, therefore a maximum absolute correlation result of $K_{max} = 2500$ is found.
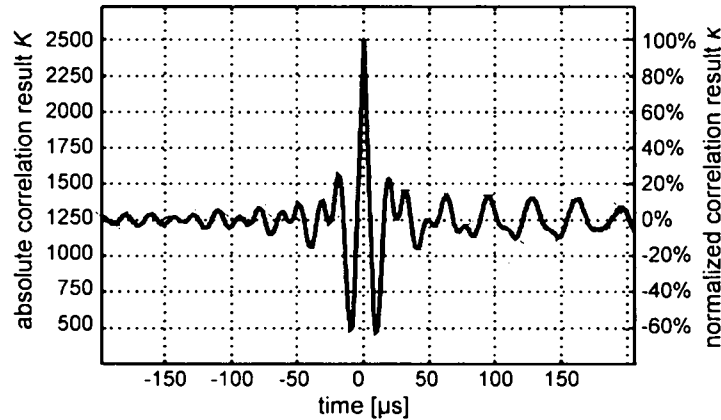
Figure 9.24: Expected one bit correlation result in case of undisturbed signal

However, in case of a real measurement the correlation result shown in Figure 9.25 is obtained. Its correlation maximum κ_{max} is about $\Delta\kappa = 20\ \%$ lower than expected and the whole signal is asymmetrical. This requires a closer look on the received signal itself.
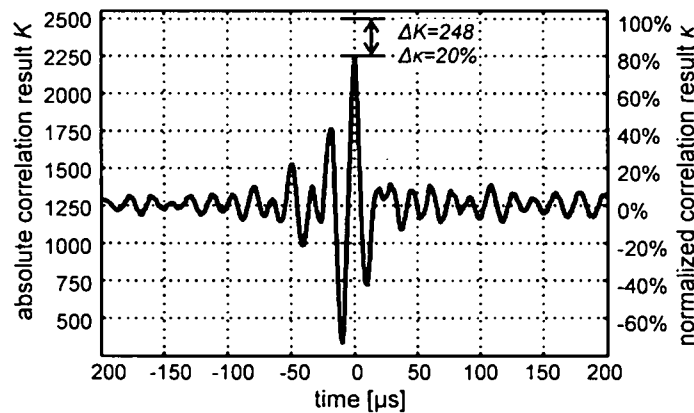
Figure 9.25: Correlation result obtained at measurement
using digitized drive voltage as reference pattern

In Figure 9.26 the received signal voltage is shown: in case a) the full received signal is presented consisting of the transient in the beginning and the measurement signal. In the last part of the signal a significant decrease of the signal amplitude is visible. Basically, this does not influence the results obtained by the one bit correlation method. In case b) this high frequency part is plotted again together with the reference signal. The position of the reference

signal is derived from the position of the correlation maximum visible in Figure 9.25. In parts of the signal considerable phase shifts are found (especially in the range $400 \ \mu s < t < 480 \ \mu s$).
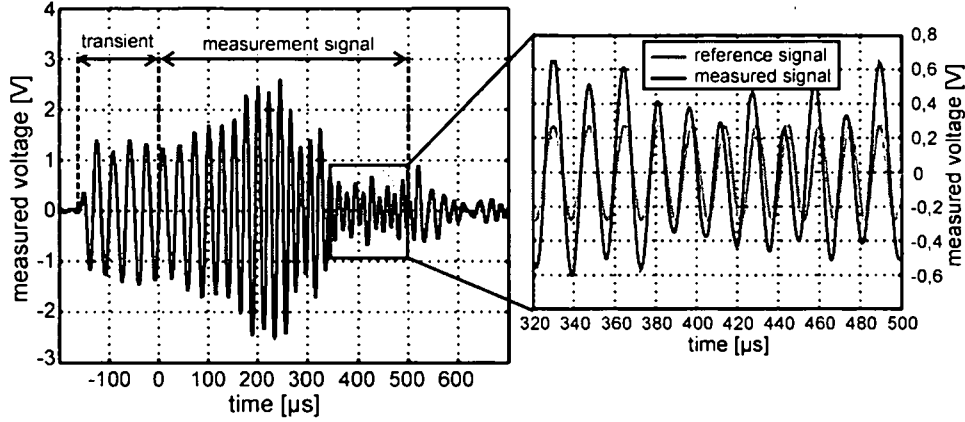
Figure 9.26: Measured signal at receiver: a) full signal and b) zoomed area of high frequency showing comparison with reference signal at position of correlation maximum

However, a phase shift dramatically influences the one bit correlation. Therefore, the deviations of the zero crossings of the measurement signal are compared with those of the reference signal and the results are shown in Figure 9.27. The unit of the deviation is the number of mismatching bits occurring at the correlation maximum. The sum of the absolute values of the deviations gives to the missing correlation part ΔK shown in Figure 9.25.
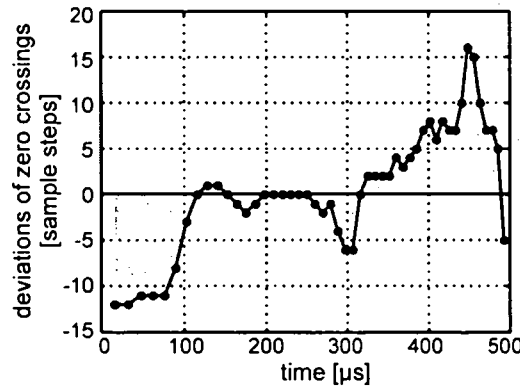
Figure 9.27: Deviations between zero crossings of measured signal and original reference pattern

One possibility to get better results is the implementation of an initial phase shift φ_{start} to the reference signal. This is accomplished by modifying the chirp generation shown in equation (6.7) to

$$f_{chirp,\varphi_{start}} = rect\left(\frac{t}{T}\right) Re\left\{ e^{j\left[2\pi t\left(f_0 + \frac{B \ t}{2 \ T}\right) + \varphi_{start}\frac{f_0}{f_0 - B}\right]} \right\}. \tag{8.35}$$

A good value of $\varphi_{start} = -80°$ is found experimentally and the correlation result found after this correction is shown in Figure 9.28. As shown in this figure, the correlation result shows a

symmetric behavior and the deviation of the correlation maximum from the ideal case becomes $\Delta\kappa = 11\%$.
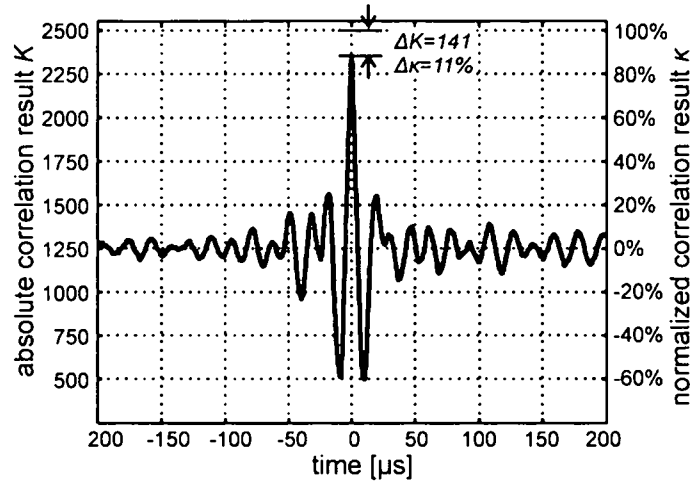
Figure 9.28: Correlation result obtained at measurement
using phase shifted signal as reference pattern

The errors of the zero crossing positions are shown in Figure 9.29. They are significantly lower.
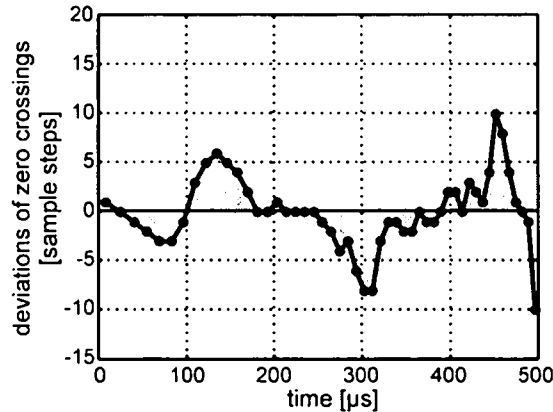
Figure 9.29: Deviations between zero crossings
of measured signal and phase shifted reference pattern

To get even better results the reference signal can be learned: therefore, the received signal shown in Figure 9.26/a is digitized and stored as reference pattern. This procedure leads to the best results and the deviations between zero crossings of measured signal and the learned reference pattern are presented in Figure 9.30.

These deviations occur due to the sampled values located near the zero crossings of the signal, where the low signal amplitude leads to a very low signal to noise ratio causing arbitrary results of the affected bits in the sampled bit stream.

Finally the correlation maxima measured during a rotational scan are evaluated: in Figure 9.31 the results obtained in case of the three presented reference patterns are shown. As expected, in case a) using the initial drive signal as reference pattern leads to the worst results: while all

correlation maxima are below about $\kappa \approx 85\,\%$, it also shows the highest correlation maxima outside the range of detection (e.g. at $\Theta \approx -15°$ a value of $\kappa \approx 65\,\%$ is found). Beside it provides a very asymmetrical behavior.
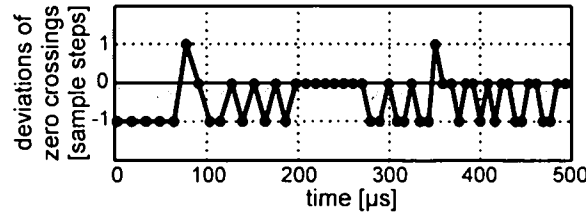
Figure 9.30: Deviations between zero crossings
of measured signal and learned reference pattern

The phase corrected reference signal in Figure 9.31/b and the learned signal in case c) are much better: both provide relatively low maxima outside the range of detection ($\kappa < 56\,\%$) and while case b) also shows a slight asymmetry, the learned reference signal is widely symmetric. The learned signal is taken from a separate measurement cycle and due to the inherent deviations at the zero crossings of the signal, a full correlation result is not reached. In other figures shown in this thesis (e.g. Figure 8.5) the reference signal is taken out of the measured data, therefore, a full correlation is found at these specific measurement cycles.
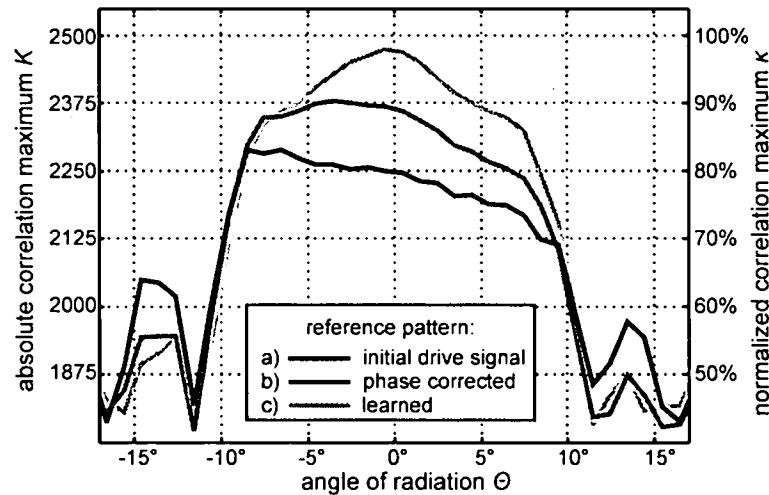
Figure 9.31: Correlation maxima depending on angle of radiation in case of different reference signals: a) initial drive signal, b) drive signal with corrected phase
and c) learned signal from reference measurement

However, it is necessary to mention that the slopes are nearly identical in all three cases, which underlines the need for an evaluation algorithm making use of the slope information.

The main features of correlation based signal processing, the high resolution and accuracy of signal detection was already shown in several works as, for example, in [Zim92], [Jör98] and

[Rei98]. However, all of them are restricted to the region of the mainlobe of the ultrasonic transducer and are only characterized in the range near the sensor axis.

The particularly new of this thesis is the attempt to define the measurement characteristics outside the already well examined range near the sensor axis. This is achieved by a systematical evaluation of the radiation pattern of the ultrasonic transducer. While in most other works the amplitude maxima (especially occurring at the main lobe) are taken into account, the main feature of this thesis is the evaluation of the position of the zeros between the main lobe and the side lobes. This is accomplished with the One Bit Correlation method that moreover provides results that are independent of the object's reflection properties.

10 Summary and Outlook

Summary

In this work basic properties of ultrasonic measurement systems were shown and analyzed. Based on this discussion demands for a new measurement concept were derived and different solutions to solve them were considered. Finally, the well known principle of pulse compression was chosen to overcome the presented problems of conventional ultrasonic measurement systems. As the amplitudes of reflected ultrasonic signals show a large dynamic range due to several reasons, the pulse compression method was implemented using a one bit correlation method that evaluates only the sign but not the amplitude of received signals. However, this correlation based method is based on large bandwidth signals; therefore, ultrasonic sensors providing a large bandwidth are necessary.

A new approach of using a separate transmitter and receiver with sufficiently different but well defined radiation patterns lead, together with the one bit correlation method, to a well defined and object independent range of detection. In contrast to multi receiver configurations which evaluate the angle of the incoming wave, the new system emits a kind of "transmission angle coded" signal due to the use of a piston modeled transmitter. Evaluation of the received signal allows determining the position of the reflecting object based on the kind of signal that is reflected. In a small range it is even possible to determine the angle of the reflecting object towards the transmitter. This so called "soft scan capability" strongly enhances scan based systems because it allows high speed scanning processes combined with high accuracy.

Fields of application are found in mobile robotics and industrial tasks, where well defined and object independent measurement areas are required. This includes collision detection systems as well as scanning tasks for scene recognition. While this measurement method also provides very interesting aspects for automotive tasks, in these cases very robust sensors are required which also must meet the wide bandwidth requirements.

Finally, a prototype was presented that allows verifying the estimated results. It consists of a commercially available electrostatic transmitter and an electret microphone, which both provide a sufficient high bandwidth. Signal generation, receiving and evaluation were done using laboratory equipment.

During the work results were presented at several international conferences ([Elm02], [Elm02a], [Elm03], [Elm03a], [Elm03b], [Sch03] and [Sch04]) and the final measurement method is subject of a pending patent [Sch04a] submitted by the Vienna University of Technology.

Outlook

While this work verifies the properties of the new measurement method, there is a lot of work to do to get a ready to use system:

- First of all a stand alone prototype allowing real time measurements in real environments will be built. Basic steps to reach this aim are already done during several student projects (compact high voltage amplifier, implementation of a fast ADC (analog to digital converter) to a high end digital signal processor, receiver circuits with proper frequency dependent amplification). However, it needs some time to fit these components together to get a running system with the expected properties.

- Further work is also necessary in the range of signal coding. While this work only uses linear chirps, other works report even better results using non linear frequency modulated signals (e.g. chirps with quadratic frequency characteristics). Therefore, these signal types will be evaluated, and their usability in the context of the measurement principle presented in this work will be checked.

- The main property of the one bit correlation method is the rejection of the signal amplitude, which leads to object independent measurement results. However, the amplitude contains a lot of information about the reflecting object. Therefore, a combined system, containing the one bit correlation and algorithms evaluating analog information, is planned.

- In this thesis signal detection is achieved by implementation of a threshold evaluating the one bit correlation results. While this method basically works, it is not suitable in case of signals providing a signal to noise ratio below about *20 dB*. Therefore, advanced algorithms with dynamically adjustable threshold levels will be developed.

- The used electrostatic transmitter basically meets the expected requirements, but it also shows some deviations in critical details. It is expected that this behavior is based on a kind of misuse of the transmitter: the used type is designed for amplitude detection based burst systems that only measure well defined objects located in its direction of radiation. However, in this work its side lobes are evaluated with high accuracy. Therefore, mechanical tolerances that do not matter in conventional systems become visible in this kind of use. As a consequence, in the future some work will be spent on sensor design to build better transmitters providing higher accuracy especially at the borders of the measurement range.

- In this work the receiver is located beside the transmitter. While this does primarily not affect the final area of detection, the evaluated distance depends on the orientation of the combination of the transmitter and receiver. To compensate this effect, the microphone must be located concentric to the transmitter, which also leads to more compact measurement systems. This will also be evaluated in the design of a new sensor.

Literature

[Ada94]   J.C.Adamowski, E.C.N.Silva, C.Simon, F.Buiochi, R.T.Higuti: *Finite Element Modeling of an Ultrasonic Capacitive Transducer*, Proc. IEEE Ultrasonic Symposium 1994, vol.2, pp.1261-1264

[Alv04]   T.E.G.Álvarez-Arenas: *Acoustic Impedance Matching of Piezoelectric Transducers to the Air*, IEEE Trans. on Ultrasonics, Ferroelectrics, and Frequency Control, 2004, vol.51, no.5, pp. 624-633

[Bab91]   M.Babic: *A 200-kHz Ultrasonic Transducer Coupled to the Air with a Radiating Membrane*, IEEE Trans. on Ultrasonics, Ferroelectrics and Frequency Control, 1991, vol.38, no.3, pp.252-255

[Bar90]   B.Barshan, R.Kuc: *Differentiating sonar reflections from corners and planes by employing an intelligent sensor*, IEEE Trans.on Pattern Analysis and Machine Intelligence, 1990, vol.12, no.6

[Bor95]   J.Borenstein, Y.Koren: *Error Eliminating Rapid Ultrasonic Firing for Mobile Robot Obstacle Avoidance*, IEEE Trans.on Robotics and Automation, 1995, vol.11, no.1, pp.132-138

[Boz92]   Ö.Bozma, R.Kuc: *Characterizing the Environment Using Echo Energy, Duration, and Range: the ENDURA Method*, Proc. of the 1992 IEEE/RSJ Intern. Conf. on Intelligent Robots and Systems, pp.813-820

[Cap94]   L.Capineri, A.S.Fiorillo, L.Masotti, S.Rocchi: *Array of PVDF Sensors for Ultrasonic Imaging in Air*, Proc. IEEE Ultrasonic Symposium 1994, vol.1, pp.487-490

[Cap97]   L.Capineri, A.S.Fiorillo, L.Masotti, S.Rocchi: *Piezo-Polymer Transducer for Ultrasonic Imaging in Air*, IEEE Trans. on Ultrasonics, Ferroelectrics and Frequency Control, 1997, vol.44, no.1, pp.36-43

[Cic97]   G.D.Cicco, B.Morten, M.Prudenziati: *A New Ultrasonic Composite Transducer Implemented with Thick Film Technology*, IEEE Trans. on Ultrasonics, Ferroelectrics and Frequency Control, 1997, vol.44, no.5, pp.992-996

[Cra46]   H.Cramér: *Mathematical Methods of Statistics*, Princeton University Press, 1946 (Reprint 1991)

[Cra93]   O.Cramer: *The variation of the specific heat ratio and the speed of sound in air with temperature, pressure, humidity, and CO_2 concentration*, The Journal of the Acoustical Society of America (JASA), 1993, vol.93, issue 5, pp.2510-2516

[Elm00]   H.Elmer: *Entfernungsmessung mittels Ultraschall nach dem Prinzip der Aktiven Reflexion*, Diploma Thesis, Vienna University of Technology, 2000

[Elm02]   H.Elmer, H.Schweinzer: *High Resolution Ultrasonic Distance Measurement in Air Using Coded Signals*, Proc. of the 19th Instrumentation and Measurement Technology Conference IMTC/2002, vol.2, pp.1565-1570

[Elm02a] H.Elmer, G.Magerl: *Hochauflösende Ultraschall-Entfernungsmessung für große Distanzen*, XVI. Messtechnisches Symposium des Arbeitskreises der Hochschullehrer für Messtechnik 2002, pp.137-148,

[Elm03]   H.Elmer, H.Schweinzer, G.Magerl: *High Resolution Ultrasonic Distance Measurement for Long Distances*, tm-Technisches Messen, Oldenbourg Verlag, 2003, Vol.70, Issue 4, pp.173-179

[Elm03a] H.Elmer, H.Schweinzer: *Effect of Frequency Dependent Radiation of Ultrasonic Transducer to Correlation Based Distance Measurement Systems*, Proc.of the 5th IFAC Symposium on Intelligent Components and Instruments for Control Applications SICICA 2003, pp.295-300

[Elm03b] H.Elmer, H.Schweinzer: *Dependency of Correlative Ultrasonic Measurement upon Transducer's Orientation*, Proc. of IEEE Sensors 2003, pp.210-215

[Far97]   R.Farlow, G.Hayward: *The Absolute Sensitivity of a Piezocomposite Transducer*, Proc. IEEE Ultrasonic Symposium 1997, vol.2, pp.911-914

[Fio92]   A.S.Fiorillo: *Design and Characterization of a PVDF Ultrasonic Range Sensor*, IEEE Trans. on Ultrasonics, Ferroelectrics and Frequency Control, 1992, vol.39, no.6, pp.688-692

[Fio98]   A.S.Fiorillo: *Piezo-polymer Ultrasound Transducer with Controlled Resonance for Medicine and Robotics*, Proc. IEEE Ultrasonic Symposium 1998, vol.1, pp.729-733

[Fio99]   A.S.Fiorillo: *Design of an Ultrasonic Sensor to Emulate Bat Bio-Sonars*, Proc. IEEE Ultrasonic Symposium 1999, vol.1, pp.409-412

[Ge99]   L-F.Ge: Electrostatic Airborne Ultrasonic Transducers: Modeling and Characterization, IEEE Trans. on Ultrasonics, Ferroelectrics and Frequency Control 1999, vol.46, no.5, pp.1120-1127

[Gia82]   P.Giacomo: *Equation for the determination of the density of moist air (1981)*, Metrologia 18, pp.33-40

[Gil99]   P.Gilkerson, P.Probert: A diffuse Reflection Model for Time of Flight Sonar, Proc.of the 1999 IEEE Intern. Conf. on Robotics and Automation, vol.1, pp.624-629

[Hal91]   M.I.Haller, B.T.Khuri-Yakub: *Micromachined Ultrasonic Materials*, Proc. IEEE Ultrasonic Symposium, 1991, vol.1, pp.403-405

[Hal96]   M.I.Haller, B.T.Khuri-Yakub: *A Surface Micromachined Electrostatic Ultrasonic Air Transducer*, IEEE Trans. on Ultrasonics, Ferroelectrics and Frequency Control, 1996, vol.43, no.1, pp.1-6

[Har01]   P.D.Harris, M.K.Andrews, G.C.Turner: *Ultrasonic Transmission and Reception from Bulk-Micromachined Transducers*, IEEE Trans. on Ultrasonics, Ferroelectrics and Frequency Control, 2001, vol.48, no.1, pp.224-231

[Hea00]   A.Heale, L.Kleeman: , Proc. of the 2000 IEEE/RSJ Intern.Conf.on Intelligent Robots and Systems (IROS 2000), vol.2, pp.1261-1266

[Hut95]   D.A.Hutchins, A.G.Bashford, W.M.D.Wright, D.W.Schindel: *Advances in Wide Bandwidth Air-coupled Capacitance Transducers*, Proc. IEEE Ultrasonic Symposium 1995, vol.2, pp.981-984

[Jin98]   X.Jin, I.Ladabaum, B.T.Khuri-Yakub: *The Microfabrication of Capacitive Ultrasonic Transducers*, IEEE Journal of Microelectromechanical Systems, 1998, vol.7, no.3, pp.295-302

[Jör97]   K.W.Jörg, M.Berg, M.Müller: *Towards Sophisticated Mobile Robot Sonar Sensing using Pseudo-Random Sequences*, Proc. EUROBOT '97, 2nd Euromicro Workshop on Advanced Mobile Robots, Brescia, Italy

[Jör98]   K.W.Jörg, M.Berg, M.Müller: *Using Pseudo-Random Codes for Mobile Robot Sonar Sensing*, IAV'98, 3rd IFAC Symposium on Intelligent Autonomous Vehicles, Madrid, Spain

[Kao00]   G.Kao, P.Probert: *Feature Extraction from a Broadband Sonar Sensor for Mapping Structured Environments Efficiently*, Intern. Journal of Robotic Research, 2000, vol.19, no.10, pp.895-913

[Kle95]   L.Kleeman, R.Kuc: *Mobile Robot Sonar for Target Localization and Classification*, Intern. Journal of Robotic Research, 1995, vol.14, no.4, pp.295-318

[Kle99]   L.Kleemann: *Fast and Accurate Sonar Trackers using Double Pulse Coding*, Proc. of the 1999 IEEE/RSJ Intern. Conf. on Intell.Robots and Systems, 1999, vol.2, pp.1185-1190

[Kle02]   L.Kleeman: *On-the-fly classifying sonar with accurate range and bearing estimation*, Proceedings of the 2002 IEEE/RSJ Intl. Conference on Intelligent Robots and Systems EPFL., vol.1, pp.178-183

[Khu88]   B.T.Khuri-Yakub, J.H.Kim, C-H.Chou, P.Parent, G.S.Kino: *A new Design for Air Transducers*, Proc. IEEE Ultrasonic Symposium 1988, vol.1, pp.503-506

[Khu98]   B.T.Khuri-Yakub, F.L.Degertekin, X-C.Jin, S.Calmes, I.Ladabaum, S.Hansen, X.J.Zhang: Silicon *Micromachined Ultrasonic Transducers*, Proc. IEEE Ultrasonic Symposium, 1998, vol.2, pp.985-991

[Kra03]   P.Krammer, H.Schweinzer: *Localization of 3D Objects Based on Ultrasonic Data, Considering the Influence of Measurement Uncertainty*, Proc. of IEEE Sensors 2003, vol.1, pp.12-17

[Kre99]   E.Kreyszig: *Advanced Engeneering Mathematics*, 8th edition, John Wiley & Sons, 1999

[Kro96]   K.Kroschel: *Statistische Nachrichtentheorie*, Springer Verlag Berlin, Heidelberg, New York, 1996

[Kuc03] R.Kuc: *Forward Model for Sonar Maps Produced with the Polaroid Ranging Module*, IEEE Trans. on Robotics and Automation, 2003, vol.19, no.2, pp.358-362

[Kut88] H.Kuttruff: *Physik und Technik des Ultraschalls*, S.Hirzel Verlag Stuttgart, 1988

[Lad95] I.Ladabaum, B.T.Khuri-Yakub, D.Spoliansky, M.I.Haller: *Micromachined Ultrasonic Transducers (MUTs)*, Proc. IEEE Ultrasonic Symposium 1995, vol.1, pp.501-504

[Lan94] J.Lan, M.J.Simoneau, R.K.Jeffers, S.G.Boucher: *A Complete Finite Element Model*, Proc. IEEE Ultrasonic Symposium 1994, vol.2, pp.999-1003

[Leo92] J.J.Leonard, H.F.Durrant-Whyte, J.J.Cox: *Dynamic map building for an autonomous mobile robot*, IJRR, 1992, vol.11, no.4, pp.286-298

[Mag94] V.Mágori: *Ultrasonic Sensors in Air*, Proc. IEEE Ultrasonic Symposium 1994, vol.1, pp.471-481

[Man92] W.Manthey, N.Kroemer, V.Magori: *Ultrasonic transducers and transducer arrays for applications in air*, Meas. Sci. Tecnology, 1992, vol.3, pp.249-261

[Mat95] P.Mattila, F.Tsuzuki, H.Väätäjä, K.Sasaki: *Electroacoustic Model for Electrostatik Ultrasonic Transducers with V-Grooved Backplates*, IEEE Trans. on Ultrasonics, Ferroelectrics, and Frequency Control, 1995, vol.42, no.1, pp.1-7

[McK96] P.J.McKerrow, S.M.Zhu: *Modelling multiple reflection paths in ultrasonic sensing*, Proc.of IEEE/RSJ Internat. Conf. on Intell. Robots and Systems 1996, vol.1, pp.284-291

[Mor68] P.M.Morse, K.U.Ingard: *Theoretical Acoustics*, New York: McGraw-Hill, 1968

[Pap99] E. P. Papadakis: *Ultrasonic Instruments and Devices*, 1st ed., Academic Press, London, 1999

[Pau81] R.P.Paul: *Robot Manipulators Mathematics, Programming, and Control*, The MIT Press Cambridge, Massachusetts and London, England, 9th Printing 1992

[Pep04] Pepperl&Fuchs: *Sensors 3, Ultrasonic Sensors*, Automation Datasheet Catalog 2004

[Pol98] Z.Politis, P.Probert: *Perception of an Indoor Robot Workspace by Using CTFM Sonar Imaging*, Proc. of the 1998 IEEE Intern. Conf. on Robotics and Automation, vol.4, pp.2801-2806

[Pol99] Z.Politis, P.J.Probert: *Modeling and Classification of Rough Surfaces Using CTFM Sonar Imaging*, Proc. of the 1999 IEEE Intern. Conf. on Robotics and Automation, vol.4, pp.2988-2993

[Raf91] M.Rafiq, C.Wykes: *The performance of capacitive ultrasonic transducers using v-grooved backplates*, Meas. Sci. Technology, 1991, vol.2, pp.168-174

[Ran02] C.Randell, I.MacColl, H.Muller, Y.Rogers: *Exploring the Potential of Ultrasonic Position Measurement as a Research Tool*, IEE Communication Networks and Service Professional Network, editors, First European Workshop on Location Based Services, Savoy Place, London, 2002, pp.171-174,

[Rei98]   C.Reimann, H.Janocha: *Hochgenaue Positionsbestimmung im Raum mit Composite-Wandlern*, Proceedings ITG-Fachtagung Sensoren und Meßtechnik, March 9.-11., Bad Nauheim, 1998

[Sal03]   J.Salazar, A.Turó, J.A.Chávez, J.A.Ortega, M.J.García: *High-Power High-Resolution Pulser for Air-Coupled Ultrasonic NDE Applications*, IEEE Trans. on Intrumentation and Measurement, 2003, vol.52, no.6, pp.1792-1798

[Sch92]   D.W.Schindel, D.A.Hutchins, L.Zou, M.Sayer: *Capacitance Devices for the Generation of Airborne Ultrasonic Fields*, Proc. IEEE Ultrasonic Symposium 1992, vol.2, pp.843-846

[Sch03]   H.Schweinzer, H.Elmer: *High Resolution Distance Measurement Systems Using Pulse Compression and Their Applications*, Proc.of the 6th Intern.Symposium on Measurement Technology and Intelligent Instruments ISMTII 2003, pp.65-70

[Sch04]   H.Schweinzer, P.Krammer, H.Elmer: *3D-Lagebestimmung von Objektkanten mittels Ultraschall-Sensoren*, e&i Elektrotechnik und Informationstechnik, Springer Verlag, 2004, Vol. 2, pp.58-67

[Sch04a]   H.Schweinzer, H.Elmer: *Ultraschall-Sensor zur Entfernungsmessung in Luft*, filed Austrian Patent Nr. A315/2004, Feb. 2004

[Sou99]   M.Soumekh: *Systhetic Aperture Radar Signal Processing*, John Wiley & Sons Inc., 1999

[Sku54]   E.Skudrzyk: *Grundlagen der Akustik*, Springer Verlag Wien, 1954

[Sta97]   B.Stanley, P.McKerrow: *Measuring Range and Bearing with a Binaural Ultrasonic Sensor*, Proc.of the 1997 IEEE/RSJ Intern. Conf. on Intelligent Roots and Systems, vol.2, pp.565-571

[Ste04]   G.Steiner, D.Watzenig, B.Schweighofer: *Time optimal control of ultrasonic transducers for improved multiple object recognition*, Proc.of the International Workshop on Robot Sensing ROSE 2004, pp.69-73

[Suz89]   K.Suzuki, K.Higuchi, H.Tanigawa: *A Silicon Electrostatic Ultrasonic Transducer*, IEEE Trans.on Ultrasonics, Ferroelectrics and Frequency Control, 1989, vol.36, no.6, pp.620-627

[Tes89]   M.Teshigawara, F.Shibata, H.Teramoto: *High resolution (0.2 mm) and fast response (2 ms) range finder for industrial use in air*, Proc. of IEEE Ultras. Symp. 1989, vol.1, pp.639-642

[War97]   A.Ward, A.Jones, A.Hopper: *A New Location Technique for the Active Office*, IEEE Personal Communications, 1997, vol.4, issue 5, pp.42-47

[www1]   Link to SENSECOMP, INC, producing various ultrasonic components: www.senscomp.com

[www2]   Link to AGILENT, producing various measurement components: www.agilent.com

[www3]   Link to A.A.LabSystems LTD, producing various specialized measurement equipments: http://www.lab-systems.com

[www4]   Link to iseg Sepezialelektronik GmbH, producing high voltage devices:
          http://www.iseg-hv.de

[www5]   Link to Amtec GmbH, producing highly integrated servo actuators:
          http://www.amtec-robotics.com

[www6]   Link to Brüel&Kjaer, producing acoustic measurement devices: http://www.bk.dk

[Yat99]   T.Yata, A.Ohya, S.Yuta: *A Fast and Accurate Sonar-ring Sensor for a Mobile
          Robot*, Proc.of the 1999 IEEE Intern. Conf. on Robotics and Automation, vol.1,
          pp.630-636

[Zim92]   G.Zimmermann: *High Resolution Ultrasonic Distance Measurement with Real-
          Time Digital Signal Processing for Industrial Field of Application*, PhD Theses (in
          German), Vienna University of Technology, 1992

[Zol98]   M.Zollner, E.Zwicker: *Elektroakustik*, 3rd edition, Springer-Verlag Berlin
          Heidelberg NewYork 1998

Lebenslauf

Mein Name ist Hannes Elmer und ich wurde am 21.3.1976 als ältester Sohn meiner Eltern Arthur und Johanna Elmer in St.Pölten geboren. Nach Abschluss der Volksschule (1982 bis 1986 am Institut der Englischen Fräulein, Linzerstrasse 11, 3100 St.Pölten) absolvierte ich in den Jahren 1986 bis 1994 am Bundesgymnasium (Bundesgymnasium und Bundesrealgymnasium, Josefstraße 84, 3100 St.Pölten) den neusprachlichen Zweig mit zusätzlicher Fremdsprache Russisch. Darauf folgte der Grundwehrdienst in der Zeit vom Oktober 1994 bis Mai 1995 in St.Pölten/Spratzern.

Im Oktober 1995 begann ich das Studium Elektrotechnik an der Technischen Universität Wien. Den gewählten Studienzweig „Automatisierungs- und Regelungstechnik" beendete ich im November 2000 mit Auszeichnung.

Von Februar 2001 bis Jänner 2005 war ich als Universitätsassistent am Institut für Elektrische Mess- und Schaltungstechnik (EMST) der Technischen Universität Wien tätig und erstellte in dieser Zeit meine Dissertation „Improved Ultrasonic Distance Measurement in Air".

Seit Februar 2005 arbeite ich im Familienbetrieb Elmer GmbH in Obergrafendorf.

Hannes Elmer